TOPOLOGY-INDUCED PHENOMENA AND CALORIC EFFECTS IN CONDENSED MATTER

Dejvid Črešnar

Doctoral Dissertation
Jožef Stefan International Postgraduate School
Ljubljana, Slovenia, July 2023

Supervisor: Prof. Dr. Zdravko Kutnjak, Jožef Stefan Institute, Jamova 39, Ljubljana, Slovenia
Co-Supervisor: Asst. Prof. Brigita Rožič, Jožef Stefan Institute, Jamova 39, Ljubljana, Slovenia

Evaluation Board:
Prof. Dr. Boštjan Zalar, Chair, Jožef Stefan Institute, Jamova 39, Ljubljana, Slovenia
Prof. Dr. Samo Kralj, Member, Faculty of Natural Science and Mathematics, University of Maribor, Koroška cesta 160, Maribor, Slovenia
Prof. Dr. Ioannis Lelidis, Member, Department of Physics, National and Kapodistrian University of Athens, 157 84 Zografou, Athens, Greece

MEDNARODNA PODIPLOMSKA ŠOLA JOŽEFA STEFANA
JOŽEF STEFAN INTERNATIONAL POSTGRADUATE SCHOOL

Dejvid Črešnar

TOPOLOGY-INDUCED PHENOMENA AND CALORIC EFFECTS IN CONDENSED MATTER

Doctoral Dissertation

TOPOLOŠKO INDUCIRANI FENOMENI IN KALORIČNI EFEKTI V KONDENZIRANI MATERIJI

Doktorska disertacija

Supervisor: Prof. Dr. Zdravko Kutnjak

Co-Supervisor: Asst. Prof. Brigita Rožič

Ljubljana, Slovenia, July 2023

Acknowledgments

My personal thanks go to my supervisor and co-supervisor Dr. Zdravko Kutnjak and Dr. Brigita Rožič for their guidance, encouragement, and constructive criticism during my time as a young researcher. My thanks also go out to Dr. Samo Kralj, whose encouragement ultimately led me to continue my PhD studies.

I would also personally like to thank Dr. Boštjan Zalar, Dr. Nikola Novak, Dr. Marta Lavrič, Dr. George Cordoyiannis, Dr. Vid Bobnar, Dr. Aleksander Matavž, Dr. Slavko Kralj, Dr. Uroš Jagodič, Dr. Andrej Rešetič, Nikita Derets, and Davorin Kotnik for their advice and cooperation during my research.

A very heartfelt thank you goes out to my junior colleagues Vida Jurečič, Matic Morgan, Rok Peklar, Lea Gašparič, and Rebeka Viltužnik for the fun and pleasant times spent together.

Finally, I would like to thank my parents, Karolina and Jure for putting up with me during these 5 years. Special thanks also go out to my sister Tina and my childhood friend Patrik, who encouraged me to return to science after a brief period of self-doubt. Thank you.

I would like to acknowledge the financial support of the Slovenian Ministry of Higher Education, Science and Innovation through their Young Researcher educational program.

Abstract

The first part of the thesis deals with the impact of surface-functionalized nanoparticles (NP) can have on the stability of liquid crystal (LC) phases. Experimental data of NP concentration-driven phase transition between the isotropic and nematic phase in 5OO8 LCs were used to create a minimal mathematical model that would qualitatively describe the observed behavior. The Lebwohl-Lasher-type lattice model was used as a basis, with the NPs acting as a random field within the lattice, and using a constant and Gaussian angular distribution for the random fields. The results of the model are in good qualitative agreement with experimental observations. This work is followed by an experimental study of oleylamine surface-coated Au NPs-induced temperature stabilization of the twist grain boundary A (TGB_A) phase in nFBTFO$_1$M$_7$ ($n = 9$, 10, 11) LCs. Calorimetric and polarized optical microscopy measurements were performed. A significant increase in the temperature range of the TGB_A phase was observed only when the lower temperature phase was the smectic A (SmA) phase. In contrast, when the lower temperature phase was the chiral smectic C (SmC^*) phase, the increase was negligible. Increasing the NP concentration in 10FBTFO$_1$M$_7$ where all three phases are present caused the SmA phase temperature range to decrease significantly, while for the TGB_A and SmC^* phases, it increased, shifting a system towards a TGB_A-SmA-SmC^* triple point. The important mechanisms for stabilizing the TGB_A phase were found to be the adaptive defect core targeting (ADCT) mechanism and the mechanism related to the saddle-splay elasticity.

The second part of the thesis deals with caloric effects. Specifically, in solid materials, the impact of doping on the electrocaloric effect (ECE) in barium titanate (BT)-based ceramics was studied. In soft materials, the impact of crosslinker concentration, crosslinking temperature, applied stress during crosslinking, and swelling with LC mesogens on the elastocaloric effect (eCE) in liquid crystalline elastomers (LCE) was investigated.
Doping $Ba_{0.8}Ca_{0.2}TiO_3$ with Zr caused an increase in the ECE, but at still relatively high temperatures ($T = 385$ K). In contrast, doping $Ba_{0.9}Sr_{0.1}TiO_3$ with Sn caused a decrease in the ECE, but lowered the temperature at which the largest ECE is observed. In the case of the eCE in LCEs, an initial numerical study was performed and compared to the experimental results. It is demonstrated that lower crosslinker concentrations, larger crosslinking temperature, lower applied stresses during crosslinking, and some swelling of LCEs cause an increase in the eCE. A peculiar behavior in eCE response was observed in the case of LCE sample with a 6% mass concentration of crosslinkers which appears to be a consequence of the proximity of the line of critical points, i.e., the crossover effect between the first-order phase transition to supercritical evolution found in relaxor ferroelectrics.

Povzetek

V prvem delu te teze se ukvarjam z vplivom površinsko funkcionaliziranih nanodelcev (ND) na stabilizacijo tekoče-kristalnih (TK) faz. Uporabil sem eksperimentalne podatke vpliva koncentracije ND na fazni prehod med izotropno in nematsko fazo v 5OO8 TK za izdelavo minimalnega matematičnega modela, ki bi kvalitativno opisal opažen pojav. Za temelj sem uporabil Lebwohl-Lasherjev mrežni model, v katerem se ND obnašajo kot naključno polje znotraj mreže. Pri naključnem polju sem uporabil konstantno in Gaussovo kotno porazdelitev. Rezultati dobro kvalitativno opišejo eksperimentalna opažanja. Sledi eksperimentalna študija vpliva Au ND, ki so površinsko funkcionalizirani z olejlaminom, na temperaturno stabilnost TK faze z zvitimi dislokacijami A (TGB_A) (ang. *twist-grain boundary A*) v nFBTFO$_1$M$_7$ (n = 9, 10, 11) TK. Kalorimetrične meritve in meritve s polarizacijskim optičnim mikroskopom pokažejo povečanje temperaturnega območja TGB_A faze, kadar je naslednja faza pri nižjih temperaturah smektična A (SmA) faza. Kadar je naslednja faza pri nižjih temperaturah kiralna smektična C (SmC*) faza, je povečanje zanemarljivo. Pri povečanju koncentracije ND v 10FBTFO$_1$M$_7$, kjer so prisotne vse tri faze, pride do precejšnjega zmanjšanja temperaturnega območja SmA faze in do povečanja TGB_A ter SmC* faze. Trend nakazuje gibanje proti TGB_A-SmA-SmC* trojni točki. Najpomembnejši mehanizmi za stabilizacijo TGB_A faze sta mehanizem za adaptivno ciljanje defektnih jeder (ang. *adaptive defect core targeting*) in mehanizem, povezan s sedlasto elastično deformacijo (ang. *saddle-splay elasticity*).
V drugem delu te teze se ukvarjam s kaloričnimi pojavi v trdnih in mehkih snoveh. Natančneje, v trdnih snoveh študiram vpliv dopiranja na elektrokalorični efekt (EKE) v keramiki barijevega titanata. Dopiranje $B_{0.8}Ca_{0.2}TiO_3$ s Zr povzroči povečanje EKE, toda največji odziv se še vedno pojavi pri relativno visokih temperaturah (T = 385 K). Dopiranje $Ba_{0.9}Sr_{0.1}TiO_3$ s Sn pa povzroči padec EKE, toda temperature, pri katerih se pojavi vrh EKE, se zmanjšajo proti sobni temperaturi. V mehkih snoveh pa proučujem vpliv koncentracije zamreževalcev, temperature zamreževanja, natezne sile med zamreževanjem in dodajanje TK molekul na elastokalorični pojav (eKE). Pri eKE v TKE sprva opravim numerično modeliranje in te rezultate primerjam z rezultati eksperimentalnih meritev. Pokažem, da manjša masna koncentracija zamreževalcev, višje temperature zamreževanja, manjše natezne sile pri zamreževanju in dodajanje majhnih količin TK v TKE povzročijo povečanje eKE. Zanimivo odstopanje je bilo opaženo v TKE vzorcu s 6% masno koncentracijo zamreževalcev, ki je posledica bližine linije kritičnih točk, opažene v feroelektričnih relaksorjih, kjer fazni prehod preko kritične točke preide iz prvega reda v superkritično evolucijo.

Contents

List of Figures

List of Tables

Abbreviations

AC . . . alternating current
ADCT . . . adaptive defect core targeting
BCE . . . barocaloric effect
BCT . . . barium calcium titanate ($Ba_{(1-x)}Ca_xTiO_3$)
BCZT . . . barium calcium zirconium titanate ($B_{(1-x)}Ca_xZr_yTi_{(1-y)}O_3$)
BP . . . blue phase
BPI . . . blue phase I
BPII . . . blue phase II
BPIII . . . blue phase III
BSTS . . . barium strontium titanate ($Ba_{(1-x)}Sr_xTi_{(1-y)}Sn_yO_3$)
BT . . . barium titanate ($BaTiO_3$)
C . . . crystal phase
DCR . . . defect core replacement
DSC . . . differential scanning calorimetry
eC . . . elastocaloric
EC . . . electrocaloric
eCE . . . elastocaloric effect
ECE . . . electrocaloric effect
I . . . isotropic phase
LC . . . liquid crystal
LCE . . . liquid crystal elastomer
LCP . . . liquid crystal polymer
MC-LCE . . . main-chain liquid crystal elastomer
MCE . . . magnetocaloric effect
N . . . nematic phase
N^* . . . chiral nematic phase
$N_L{}^*$ . . . short pitch twist-grain boundary phase
NP . . . nanoparticle
OA . . . oleylamine
PMN-PT . . . lead magnesium niobite-lead titanate $Pb(Mg_{1/3}Nb_{2/3})O_3$-$PbTiO_3$
PN . . . paranematic phase
POM . . . polarizing optical microscopy
RAN . . . random-anisotropy-nematic
SC-LCE . . . side-chain liquid crystal elastomers
SmA . . . smectic A phase
SmC . . . smectic C phase
SmC^* . . . chiral smectic C phase
TD . . . topological defect
TGB_A . . . twist-grain boundary A phase

Symbols

$\underline{B}$	...	molecular field tensor
C_p	...	heat capacity at a constant pressure
c_p	...	specific heat capacity at a constant pressure
d_0	...	disorder strength
d	...	normalized disorder strength
$\vec{E}$	...	electric field
F	...	Helmholtz free energy
f	...	Helmholtz free energy density
G	...	Gibbs free energy
g	...	Gibbs free energy density
H	...	enthalpy
$\vec{H}$	...	magnetic field
h	...	normalized uniaxial stress
h_e	...	normalized external uniaxial stress
h_i	...	normalized internal uniaxial stress
$\vec{h}$	...	helical axis
J_{ij}	...	interaction strength between neighboring nematic spins
K_i	...	Frank elastic constant
k	...	winding number
k_B	...	Boltzmann constant
L	...	latent heat
l	...	length
M	...	external field conjugate to the order parameter α
$\vec{M}$	...	magnetization
m	...	mass
m_{LC}	...	mass of mesogens in liquid crystal
m_{LCE}	...	mass of mesogens in liquid crystal elastomer
$\vec{n}$	...	nematic director
P	...	power
$P(\vec{e}_i)$	...	probability distribution
$\vec{P}$	...	polarization
$\vec{P}_S$	...	spontaneous polarization
p	...	hydrostatic pressure
Q	...	heat
$\underline{\underline{Q}}$	...	global nematic order parameter

Q_{ij}	...	tensor order parameter
q	...	topological charge
$\vec{q}$	...	wave vector
$\underline{\underline{q}}$	...	nematic tensor order parameter
R	...	thermal resistance
r	...	normalized temperature
S	...	scalar orientational order parameter
T	...	temperature
T^*	...	supercooling temperature
T^{**}	...	superheating temperature
T_B	...	thermal bath temperature
T_C	...	Curie temperature
$T_{N_L^*-N^*}$	...	phase transition temperature between N^* and $N_L{}^*$
T_S	...	sample temperature
ΔT_{ECE}	...	electrocaloric temperature change
ΔT_{eCE}	...	elastocaloric temperature change
t	...	time
V	...	volume
w_i	...	interaction strength between nematic spins and impurities
α	...	order parameter describing a system
γ	...	coupling constant between the order parameter and the disorder strength
ε	...	strain
ε'	...	dielectric constant
η	...	translational order parameter
λ	...	relative length
ξ	...	electrocaloric responsivity
ρ	...	density
σ	...	uniaxial stress
τ_{ext}	...	external diffusion time
τ_{int}	...	internal diffusion time
ϕ	...	volume concentration
φ	...	phase shift
χ	...	mass concentration
Ω	...	entropy
Ω_{dip}	...	dipolar subsystem entropy
Ω_{LC}	...	liquid crystal subsystem entropy
Ω_T	...	thermal subsystem entropy
ω	...	angular frequency

Chapter 1

Introduction

Topological defects (TD) appear in a variety of physical systems, such as soft matter [1–7], quantum systems [8–11], superfluids [12,13], thin-film magnets [14–16], and cosmology [17–20]. Defect structures, which are a consequence of symmetry breaking at phase transitions, can form chaotic or even regular structures. It is most convenient to study such defect structures in systems that exhibit universal features of defect structures and are quantitatively simple to study [18–23]. Liquid crystals (LC) are attractive for exactly such a purpose. These systems exhibit structural variety, have reasonable relaxation times, and require a negligible amount of energy to induce a state change. Boundary effects [24,25], the addition of colloidal particles [1,4,26–30], external fields [31–35] and flow [36–40] can increase the complexity of such systems. They allow us to study the dynamics and interactions between defects as well as their influence on the surrounding matrix using conventional optical polarizing microscopes.

LC are typically rod-shaped or disc-shaped organic molecules that exhibit one or more intermediate states between an isotropic (I) liquid and a crystalline solid [41–43]. Each LC phase, or mesomorphic phase, exhibits a certain long-range order in their molecular arrangement, such as long-range orientational order in the nematic phase (N), where on average LC molecules are oriented along the same direction. Hence why LCs are sometimes referred to as anisotropic liquids. Depending on the LC, the transitions between various phases can be achieved in two ways: by changing the temperature or the concentration. The former type of LCs are known as thermotropic, while the later are known as lyotropic. In this work, only thermotropic LC will be explored.

The last decade has seen an increase in the study of interactions between different nanoparticles (NP) and TD within an LC matrix. Homogeneous mixtures of LC with NP can often lead to new and enhanced electrooptical properties [44–47], changes in phase behavior [28,48–53], stabilization of different topological structures [3,54–56], and other behavior useful for applications. The presence of colloidal particles or NP leads to a distortion in the nematic elastic field, which causes the appearance of long-range interactions between particles [1,2,5,29,56–58]. Once orientational order increases, so does the tendency toward phase separation. On the other hand, an appropriate surface treatment of NP can reduce this tendency. They can also stabilize an LC structure containing a lattice of TD. This stabilization is enabled by the defect core replacement (DCR) mechanism [59]. Appropriately surface-treated NPs reduce the free energy penalty of forming TD by replacing part of the energetically costly core with the volume of the trapped NP. The same mechanism is believed to be responsible for pinning vortices to impurities in type-II superconductors.

On the applicational side of things, LC can also be used in another interesting way. One can incorporate them into a polymer chain, either by being part of the polymer

backbone or hanging from its side. Crosslinking these liquid crystal polymers (LCP) into an elastomer forms a liquid crystalline elastomer (LCE). These materials combine the elastic properties of an elastomer with the orientational and positional ordering of LC [60]. The coupling between strain and orientational order is useful, since one can alter one by altering the other. If, for example, we change the orientational order of the LC by changing the temperature of the material, we can alter the material length (thermomechanical effect). Similar effects can be reached by using electric fields and ultraviolet light. Thus, they have great applicational potential as sensors and actuators [61–69]. On the other hand, it has been demonstrated that if you extend LCE in an adiabatic fashion near an appropriate temperature, which turns out to be the I-N phase transition temperature of the LC, the LCE will heat up. Releasing the external stress allows the LCE to contract back to its original length, which causes it cool down. Extending and then contracting LCEs causes them to heat up or cool down. This is an example of the elastocaloric effect (eCE), which belongs to the larger family of caloric effects.

Another member of the caloric effects is the electrocaloric effect (ECE). In this case, the external field driving the temperature change of the material is the electric filed, and the order parameter coupled to the external electric field is polarization. The ECE is observed in ferroelectric materials. In such materials, a large enough external electric field can produce a spontaneous polarization to appear. These materials are, along with their wide array of functional properties [70], interesting for their applicational potential as environmentally friendly heat-management devices. This work will focus on the ECE in doped lead-free barium titanate $BaTiO_3$ (BT) ferroelectric ceramics.

This thesis is composed of two parts, each dealing with the impact of structural disorder on phase ordering and specific properties such as caloric effects. In the first part, we will focus on LCs and the description of their phases relevant to this work. A description of topological defects will follow this. The following two chapters will present computational and experimental results of LC-NP mixtures. In the first case, we will present a mathematical model describing the impact of NP on the orientational order of a LC in the N. After this, we present the model results and compare them with experimental results. In the second case, we will present the alternating current (AC) calorimetry results of LC-NP mixtures focusing on the potential temperature stabilization of the twist-grain boundary A phase (TGB_A) as an example of the adaptive defect core targeting (ADCT) mechanism. In the second part of this thesis, we will focus on the caloric effect. The caloric effect is introduced, followed by a description of the ECE in doped lead-free $BaTiO_3$ ceramics and the eCE in LCEs. In both cases, we briefly introduce these materials, including their relevant properties for our investigation. After which, we present the dielectric and ECE measurement results in doped lead-free $BaTiO_3$ ceramics. Following the same pattern, the thermomechanical and eCE measurement results in LCEs are presented. In a separate chapter, we also introduce the experimental and sample preparation techniques. In the conclusion, a summation of all the main results and propositions for further research are given.

Chapter 2

Topological Phenomena in Liquid Crystal

We shall begin by giving a brief but relevant overview of LCs and their various phases as it pertains to our research. This will then be followed by the phenomenological description of various LC phases and a description of topological defects (TD), since they form the basis of our inquiry into the effect of NP on the LC order. It will be shown that NP can have both a destructive and constructive effect with an appropriate surface treatment. What is meant by this is they can either destroy the global orientational order by forming a TD-NP pair, also known as a topological dipole, creating an order-destroying random field, or stabilizing certain TD structures in LCs by interacting with them, thereby reducing their free energy penalty.

2.1 Nematic Phase

The simplest LC phase is the N phase. There is no positional order, however, the molecules maintain, on average, a preferred orientation as they diffuse through space (Figure 1). This direction is expressed by a unit vector $\vec{n}$, called the nematic director or simply the director, and is a vectorial order parameter. It is obtained by averaging over molecular orientations $\vec{e}$. The averaging is performed over a large volume compared to the molecular dimension but small compared to typical deformation lengths in an N phase. The special property of the director is that it does not distinguish between the direction $\vec{n}$ and $-\vec{n}$, or in other words, there is a head-to-tail symmetry. This assumes an absence of polarity, which tends to be true for all nematic LC. Without any external influences, the global orientation of the N phase is completely arbitrary. However, $\vec{n}$ does not contain any information about the degree of orientational ordering.

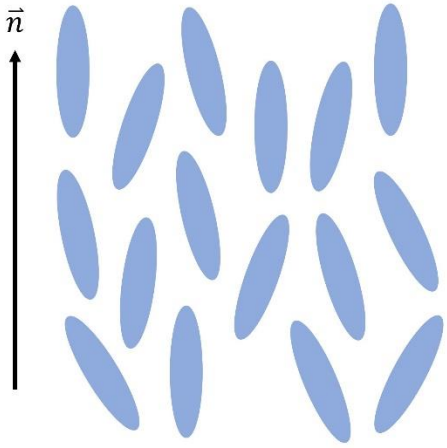

Figure 1: A schematic depiction of an N phase. LC molecules are, on average, oriented along the same direction represented by nematic director $\vec{n}$.

The anisotropic nature of N phase can be seen in a number of measurable macroscopic quantities, such as the diamagnetic susceptibility, the refractive index, and the dielectric permittivity. For example, typical nematic LCs are optically uniaxial: the polarization along the long axis of the molecule is different from that perpendicular to it. The anisotropy of these tensorial quantities can serve the role of an order parameter. What we end up with is a second-rank tensor known as the tensor order parameter:

$$Q_{ij} = \left\langle e_i e_j - \frac{1}{3}\delta_{ij} \right\rangle = s \left\langle n_i n_j - \frac{1}{3}\delta_{ij} \right\rangle. \tag{1}$$

The $\langle ... \rangle$ denotes the thermal average, indices i and j run over (x, y, z), and s is known as the scalar orientational order parameter and defined as:

$$s = \frac{1}{2}\langle 3\cos^2\theta - 1 \rangle, \tag{2}$$

where θ is the angle between the molecular orientational axis $\vec{e}$ and nematic director $\vec{n}$. In the I phase $s = 0$, and in the N phase $0 < s \leq 1$.

2.2 Smectic Phase

In addition to having orientational order, smectic phases have some positional order in the form of a layered structure resembling a bookshelf. The molecules are allowed to move freely within the layers. This is why smectic LC are sometimes referred to as two-dimensional liquids. The simplest smectic phase is the smectic A phase (SmA), where the molecules are stacked in a layer of thickness d, and the director $\vec{n}$ is parallel to the layer normal. If the director $\vec{n}$ is slightly tilted away from the layer normal, then we have the smectic C phase (SmC). A schematic depiction of both phases is shown below (Figure 2).

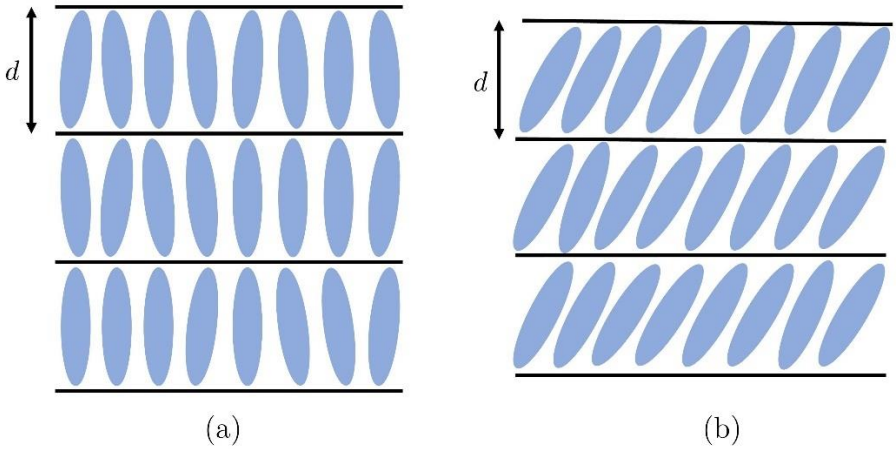

Figure 2: A schematic depiction of two smectic phases. a) A SmA phase where the LC molecules are, on average, oriented parallel to the smectic layer normal. b) A SmC phase where the molecules form an angle with the smectic layer normal.

Similar to when we defined the orientational order parameter for the N phase, we can define the positional order parameter for the smectic phases. In simple fluids, the density ρ is commonly considered the relevant variable. In a smectic LC, ρ will have a constant value within the smectic layers but will spatially vary in the direction of the layer normal in a periodic fashion. In a good approximation, the density deviation from its equilibrium value ρ_0 can be expressed as:

$$\rho(\vec{r}) - \rho_0 = \eta(\vec{r}) \cos(\vec{q} \cdot \vec{r} - \varphi) + \cdots = \eta(\vec{r}) e^{i(\vec{q} \cdot \vec{r} - \varphi)} + \cdots \tag{3}$$

The density modulation is not very strong, and to a first approximation, the complex smectic order parameter can be expressed by a single harmonic:

$$\psi(\vec{r}) = \eta(\vec{r}) e^{i(\vec{q} \cdot \vec{r} - \varphi)}, \tag{4}$$

where $\vec{q}$ is the wave vector of the period structure, φ is phase shift, and $\eta(\vec{r})$ is the translational order parameter that quantifies the degree of layer ordering. In an N phase $\psi(\vec{r}) = 0$, while in a smectic phase $\psi(\vec{r})$ is a complex number. Such a definition of the smectic order parameter is quite useful since one can draw parallels between N-SmA and conductor-superconductor phase transitions [71].

2.3 Twist Grain Boundary A Phase

An object that cannot be transformed into its mirror image by applying rotations and translations is called chiral. LC phases formed by chiral molecules are very special and unusual. They can contain an intrinsic helical structure in the director field. In chiral N phases, also known as cholesteric phases, the nematic director $\vec{n}$ continuously rotates along a helical axis $\vec{h}$. The typical length for which it takes $\vec{n}$ to fully rotate along $\vec{h}$ is called pitch p. Similar helical structures can be found in chiral SmC phases (SmC*), where the molecular tilt within each layer is rotating for a small angle from one smectic layer to another (Figure 3a).

However, it is impossible to simultaneously generate a continuous structure exhibiting both a smectic layer structure and a helical structure within the smectic layers. The

frustrated structure created by the competition between these two conflicting structures contains a regular grain boundary lattice consisting of a lattice of screw dislocations. These structures tend to form in the temperature range between the chiral N phase with a short pitch and a smectic phase, typically SmA phase or SmC* phase [72–75].

The twist grain boundary A (TGB_A) phase (Figure 3b), which we will be interested in, consists of smectic slabs separated by defect walls. The neighbouring slabs are tilted by a small angle with respect to each other around a helical axis, leading to a helical structure. The ordering within each slab is equivalent to that of a regular smectic A phase: the molecules are arranged in layers and are uniaxially aligned along the local director $\vec{n}$, which is parallel to the smectic layer normal. The grain boundaries between slabs are defect walls consisting of parallel defect lines, specifically, twist dislocations.

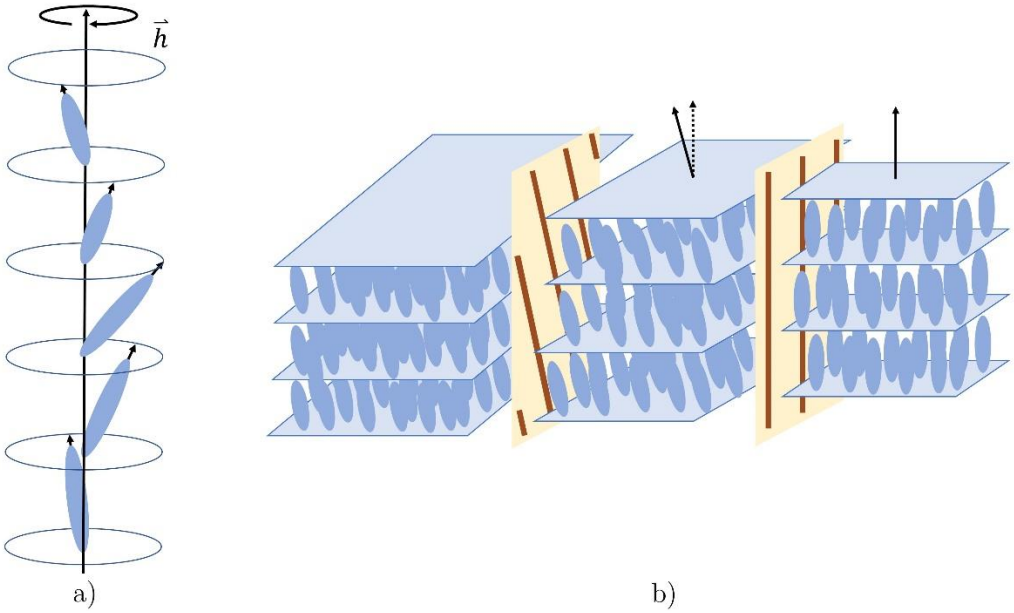

Figure 3: a) In an SmC* phase, as we move through the smectic layers upward, the angled LC molecules rotate along the helical axis $\vec{h}$. b) A schematic depiction of a TGB_A phase, where the neighboring smectic slabs are rotated with respect to each other, separated by a layer of grain boundaries.

2.4 Phenomenological Description of Phase Transitions in Liquid Crystals

Different phases of matter differ by the type of order, mass density, polarization, magnetization, and so on. Transitions between phases is described by thermodynamic potentials, such as the Gibbs free energy G and the Helmholtz free energy F, and their derivatives. We differentiate between two types of phase transitions: first-order and second-order. In a first-order phase transition the first derivative of the thermodynamic potential, which is usually the order parameter or entropy, exhibits a discontinuous jump at the transition point. These transitions usually involve nonzero latent heat. In a second-order phase transition the first derivative is continuous, but the second derivative, usually the heat capacity, diverges at the transition point. No latent heat is present in these phase transitions.

In order to describe such phase transition, the phenomenological Landau theory is used. The basic idea is to find a proper order parameter of the observed system, expanding the

free energy in the vicinity of the phase transition as a power series of the order parameter, and finding the minima of the free energy as a function of the order parameter [41–43]. In such an expansion not all terms are permissible when one takes symmetry considerations in to account.

2.4.1 Landau-de Gennes model of the nematic-isotropic phase transition

The appropriate order parameter required to describe the N-I phase transition is the second-rank tensor order parameter Q_{ij} (Equation (1)). The Landau expansion of the Gibbs free energy density in terms of Q_{ij} is:

$$g(T) = g_0 + \frac{1}{2}A(T)Q_{ij}Q_{ji} + \frac{1}{3}B(T)Q_{ij}Q_{jk}Q_{ki} + \frac{1}{4}C(T)Q_{ij}Q_{jk}Q_{kl}Q_{li} + \cdots, \tag{5}$$

where g_0 is the Gibbs free energy density of the I phase. An interesting feature of such an expansion is the presence of the cubic term, which is not invariant under the transformation $Q_{ij} \rightarrow -Q_{ij}$. These states are not degenerate, and therefore, not allowed. According to Landau's theorem, such a phase transition is first-order. A necessary condition for the transition to be second-order is the vanishing of $B(T)$.

The expansion coefficients $A(T)$, $B(T)$, and $C(T)$ are assumed to be temperature dependent. In practice one usually takes only $A(T)$ to be temperature dependent, while B and C are taken to be temperature independent. The simples form of $A(T)$ is $A(T) = A_0(T - T^*)$ with T^* being the supercooling temperature. It represents the limit of metastability of the I phase. Combining Equations (1) and (5) yields:

$$\begin{aligned} g(T) &= g_0 + \frac{1}{3}A_0(T - T^*)S^2 + \frac{1}{4}BS^3 + \frac{9}{16}CS^4 + \cdots = \\ &= g_0 + \frac{1}{2}a_0(T - T^*)S^2 + \frac{1}{3}bS^3 + \frac{1}{4}cS^4 + \cdots. \end{aligned} \tag{6}$$

Minimizing Equation (6) with respect to S and taking in to account only term up to the S^4 term yields:

$$\frac{\partial g}{\partial S} = a_0(T - T^*)S + bS^2 + cS^3 = 0, \tag{7}$$

with the physically accepted solutions being:

$$\begin{aligned} S_I &= 0, \\ S_N &= \frac{b}{2c}\left(1 + \sqrt{1 - \frac{4a(T - T^*)c}{b^2}}\right). \end{aligned} \tag{8}$$

At the transition point we have the condition $g(S_N) = 0$ and $\partial g/\partial S = 0$. Combining these two expressions into:

$$\left(\frac{1}{4}S\frac{\partial g}{\partial S} - g\right)\Big|_{S=S_{IN}} = 0, \tag{9}$$

one can determine the equilibrium order at the transition point $S_{IN} = 2b/3c$, the phase transition temperature $T_{IN} = T_C = T^* + 2b^2/9a_0c$, and the enthalpy density change due to the jump in system entropy $\Delta h = T_{IN}\Delta\Omega = -2T_{IN}a_0b^2/9c^2 = -T_{IN}a_0S_{IN}^2/2$. The superheating temperature T^{**}, the limit of metastability of the N phase, is determined to be $T^{**} = T^* + b^2/4a_0c$. Figure 4 shows the $\Delta g = g(T) - g_0$ as a function of S for various temperatures. At $T > T^{**}$ the I phase is absolutely stable. At $T_C < T < T^{**}$, a relative minimum $S_N > 0$ appears, with the system remaining in the I phase if it was initially in the I phase. On the other hand, if the system is initially in the N phase, it can be superheated above T_c. At $T^* < T < T_C$ the I phase is metastable and the N phase is stable. One can observe the nucleation and growth of nematic droplets when the system is cooled from the I phase.

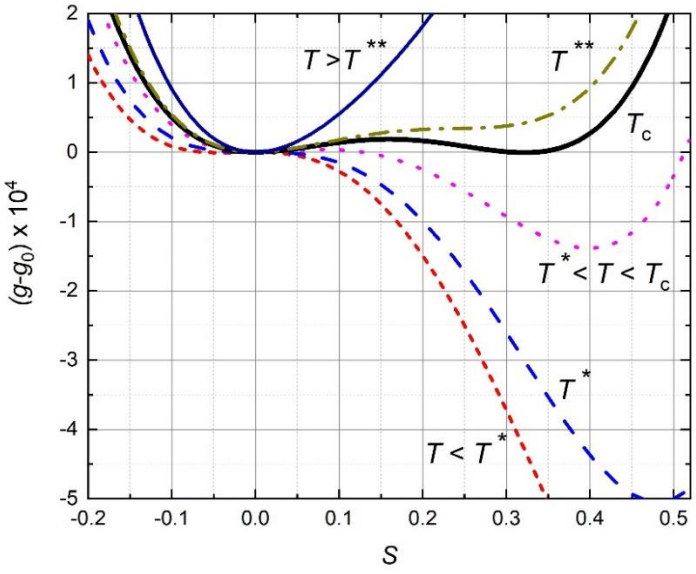

Figure 4: The Gibbs free energy density $\Delta g = g(T) - g_0$ as a function of S for various temperatures. T^* is the supercooling temperature, T^{**} is the superheating temperature, and T_C is the phase transition temperature.

2.4.2 Ginzburg-Landau model of the smectic A-nematic phase transition

As can be seen from Equation (4), the order parameter of the SmA phase contains two components: the translational order parameter that quantifies the degree of layer ordering $\eta(\vec{r})$, and the phase shift φ describing the position of the smectic layers. The Ginzburg-Landau expansion of the free energy density in terms of the complex smectic order parameter $\psi(\vec{r})$ is:

$$f(T) = \alpha(T - T_C)|\psi|^2 + \frac{1}{2}\beta|\psi|^4 + C_\parallel\left|\frac{\partial\psi}{\partial z}\right|^2 + C_\perp|\nabla_\perp\psi|^2 + \cdots, \tag{10}$$

with α, β, $C_\parallel$, and $C_\perp$ being positive temperature independent material constants, and $\nabla_\perp = (\partial/\partial x, \partial/\partial y, 0)$. Since there are no odd terms, the transition is second-order. The gradient terms reflect the possibility of spatial variation of ψ. This expression presumes that $\vec{n}$ is fixed. In reality $\vec{n}$ does fluctuate, thus we must modify the gradient terms to

take this in to account. Let the smectic layer normal be parallel to the z-axis. A small deviation of $\vec{n}$ from the z-axis will have a negligible effect. On the other hand, the change in the plane perpendicular to the z-axis is $\delta\vec{n}_\perp = \vec{n} - \vec{z}$. A rotation δn_x of the layer implies a displacement $-\delta n_x x$ with the new smectic order parameter being $\psi = \psi_i e^{iq_s \delta n_x x}$. Here ψ_i is the smectic order parameter defined in its local reference frame, also known as the intrinsic smectic order parameter. In order to obtain the expression $C_\perp|\nabla_\perp\psi|^2$ we modify it into $C_\perp|(\nabla_\perp - iq_s\delta\vec{n}_\perp)\psi|^2$, which gives $C_\perp|\nabla_\perp\psi_i|^2$ for the ψ_i, as we desired. Thus, the final expression for the free energy density as a function of $\psi(\vec{r})$ is:

$$f(T) = \alpha(T - T_C)|\psi|^2 + \frac{1}{2}\beta|\psi|^4 + C_\parallel\left|\frac{\partial\psi}{\partial z}\right|^2 + C_\perp|(\nabla_\perp - iq_s\delta\vec{n}_\perp)\psi|^2 + \cdots. \tag{11}$$

2.4.3 The Frank elastic free energy

In the case of the I-N phase transition, it was assumed that the director field $\vec{n}(\vec{r})$ is constant thought space. In reality there are always spatial fluctuations of $\vec{n}(\vec{r})$ due to constraints that are imposed on the boundaries of a system. Such fluctuations impose a free energy penalty on the system. Assuming that $\vec{n}(\vec{r})$ varies slowly and continuously, the most basic deformations found in LCs are splay, twist, and bend deformations shown in Figure 5. The free energy penalty expression for a LC system which contains splay, twist, and bend deformations is given by the Frank elastic free energy expression [76]:

$$\begin{aligned} f_{el} &= \frac{1}{2}K_i(\partial_i n_j)(\partial_i n_j) = \\ &= \frac{1}{2}K_1(\nabla\vec{n})^2 + \frac{1}{2}K_2[\vec{n}(\nabla\times\vec{n})]^2 + \frac{1}{2}K_3[\vec{n}\times(\nabla\times\vec{n})]^2, \end{aligned} \tag{12}$$

with the first term describing the splay deformations, the second term describing the twist deformations, and the third term describing the bend deformations. The strengths of these deformations are determined by the Frank elastic constants K_1, K_2, and K_3.

In the case of chiral LCs, where $\vec{n}$ is induced to twist spatially and adopt a helical structure, the full Frank elastic free energy expression becomes:

$$\begin{aligned} f_{el} = \frac{1}{2}K_1(\nabla\vec{n})^2 + \frac{1}{2}K_2[\vec{n}(\nabla\times\vec{n}) + q_0]^2 + \frac{1}{2}K_3[\vec{n}\times(\nabla\times\vec{n})]^2 - \\ -K_{24}\nabla\cdot(\vec{n}\nabla\cdot\vec{n} + \vec{n}\times\nabla\times\vec{n}). \end{aligned} \tag{13}$$

The twist term is modified by an addition of $q_0 = 2\pi/p$, with p being the pitch, and the additional K_{24} term is known as the saddle-splay term. Due to its divergence nature it is usually expressed as a surface term once integrated over a volume.

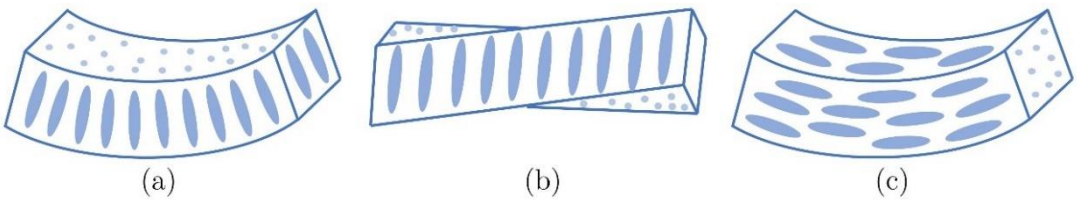

Figure 5: Depiction of three types of deformations found in LC: a) splay deformation, b) twist deformation, and c) bend deformation.

2.4.4 Boundary effects

So far, only bulk terms were considered, which need to be supplemented by terms associated with surface effects on the boundaries. Interactions between LC molecules and the surrounding boundary modifies the LC structure in the vicinity of the boundary (structural rearrangements) and limits the possible orientations of $\vec{n}$ within the bulk (anchoring phenomena) [43]. The surface orientation of $\vec{n}$ is determined by the polar and azimuthal angles θ and φ. A particular direction which minimizes the interfacial tension σ, and thus the reduces the free energy penalty due to the distortion of $\vec{n}(\vec{r})$, is called the easy axis, represented by the angles θ_0 and φ_0. The interfacial tension $\sigma(\theta, \varphi)$ can be expressed as the sum of $\sigma(\theta_0, \varphi_0)$ and an anchoring energy function $w(\theta, \varphi)$, which depends on the intermolecular interactions at the boundary. It is often assumed that the surface anchoring energy can be expressed as:

$$w = -\frac{1}{2} w_\theta (\vec{n} \cdot \vec{e})^2, \tag{14}$$

where w_θ is the polar anchoring coefficient and $\vec{e}$ the direction of the easy axis. This expression is known as the Rapini-Papoular anchoring potential [77]. It can equivalently be expressed as:

$$w = -\frac{1}{2} w_0 \vec{e} \cdot \underline{Q} \vec{e}. \tag{15}$$

Depending on the size of w_0 we differentiate between strong and weak anchoring. We shall only be interested in weak anchoring conditions, were the resulting interaction on the boundary has a negligible impact on the qualitatively bulk behavior of the LC, as opposed to strong anchoring conditions that have a significant impact on the bulk LC structure. Depending on the type of surface anchoring, whether strong or weak, plane parallel (planar) or plane perpendicular (homeotropic), boundary effects can have a constructive or destructive impact on the surrounding LC structure.

2.5 Topological Defects

The order parameter is a continuous field that describes the state of the system at each point. Generally, it is a function of coordinates. Distortions in this continuous field can be of two types: those containing singularities and those without singularities. A singularity is a space region where the local order parameter is not defined. The singular regions, or defects as we shall be referring to them from here on out, which we encounter, are either zero-dimensional (points), one-dimensional (lines), or two-dimensional (walls). A TD is a nonhomogeneous state which cannot be eliminated by a continuous variation of the order parameter, in other words, one cannot arrive at a homogeneous state [43].

TD can be categorized based on its influence on the surrounding director field. For example, let us look at point defects in a two-dimensional N system. We can assign to each TD a number known as a topological charge. In order to determine the topological charge, we encircle the point defect with an imaginary loop. As we move around this loop counter-clockwise, we observe how much the director's orientation changes. Mathematically, this process is written as follows:

$$k = \frac{1}{2\pi} \oint \frac{d\theta}{dl} dl, \tag{16}$$

where the integration takes place over a closed loop path, θ is the orientation of the director field, and dl is a small line segment of the closed loop. Here, k is referred to as the winding number and is equal to the topological charge q in a two-dimensional system. Some examples are shown in Figure 6. Due to the head-to-tail symmetry of the nematic director, half-integer values can be obtained.

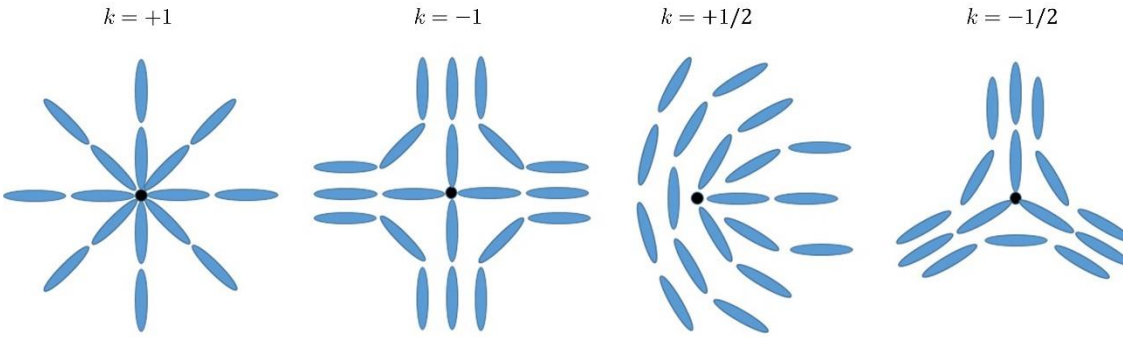

Figure 6: TD with various values of topological charges: from positive and negative to integer and half values.

We can analogously determine the topological charge of a point defect in three-dimensions, except in this case the closed loop is replaced by a closed surface and mathematically the expression changes to:

$$q = \frac{1}{4\pi} \oiint \vec{n} \cdot \left(\frac{\partial \vec{n}}{\partial u_1} \times \frac{\partial \vec{n}}{\partial u_2} \right) du_1 du_2, \tag{17}$$

where u_1 and u_2 are a parametrization of the closed surface encompassing the point defect, and the integral runs over the entire surface [43]. As we can see, the topological charge depends on the third power of $\vec{n}$. This implies that the sign of the topological charge depends on the direction we assign the director. This may look like an issue since by assigning a direction to the director, we are breaking its head-to-tail symmetry. However, the direction we choose is purely for convenience and is completely arbitrary. Thus, the sign of the charge is completely arbitrary as well. We have to ensure that we are consistent when determining topological charge values based on our direction choice.

An important result of topology is the conservation of topological charge. This conservation law implies that if we create a point defect with a topological charge $q = 1$, the system will create a point anti-defect with a topological charge $q = -1$. The total change of the topological charge is $\Delta q = 1 + (-1) = 0$. Let us look at two systems of a N LC: one without any TD and the other with two-point defects of opposite charge ($q_1 = 1$ and $q_2 = -1$). Both systems have a total topological charge of $q = 0$. Can one system, without any external influence, be transformed into the other? Defects create distortions in the nematic director field, which imposes a free energy penalty on the system described by Equation (13). The N LC system will attempt to destroy these two defects by bringing them together and annihilating them in the same way a positron-electron pair is annihilated. With this, the free energy penalty no longer exists.

The next question is what happens in a N LC system when one introduces a defect in the form of a colloidal particle, which interacts with the surrounding LC matrix? Regardless of the type of anchoring on the surface of the particle, whether homeotropic or planar, the total topological charge of this combined system has changed. A particle with homeotropic anchoring is equivalent to a topological point defect with charge $q = 1$ (Figure 7). In order for the total topological charge to remain zero, the N itself must nucleate an additional point anti-defect with charge $q = -1$. However, unlike in the previous example where the

point defect and point anti-defect annihilate, thus reducing the free energy penalty, here the colloidal particle cannot be destroyed by the point anti-defect. Instead, they form a particle-defect assembly, or in other words, a topological dipole [2]. These types of particle-defect assemblies dispersed randomly in the LC matrix can form a kind of random field that can locally induce a different directional ordering compared to the global directional ordering of the LC [78].

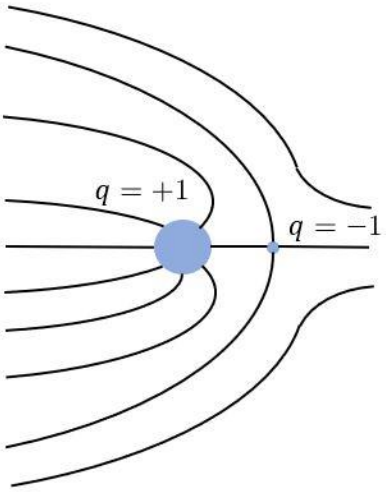

Figure 7: Depiction of a topological dipole formed by a particle-defect assembly. Since the NP is a physical object and not a TD, it cannot be destroyed by the topological anti-defect through annihilation.

2.6 Experimental Techniques used in the Study of Liquid Crystals

Throughout this work, we use various sample preparation and measurement techniques. The measurement techniques can be divided into two categories: heat capacity C_p measurements and temperature T measurements. In other words, calorimetric and caloric effect measurements.

2.6.1 Calorimetric measurements and analysis

An important role is played by enthalpy H and the heat capacity C_p in the characterization of the type of critical behavior, as well as the type of phase transition, whether first- or second-order, in the material [79–81]. In a simple first-order transition, there is a discontinuous jump in H due to the presence of latent heat L, but little or no pretransitional behavior in C_p. In a second-order transition, $L = 0$, while C_p usually exhibits a power law singularity. Often, there is also a substantial excess enthalpy $\delta H = \int \Delta C_p dT$, where $\Delta C_p = C_p - C_p^{(background)}$, and $C_p^{(background)}$ represents the normal C_p behavior expected in the absence of the transition. Various types of transitions are presented in Figures 8 and 9.

Standard calorimetric techniques, such as traditional adiabatic calorimetry and differential scanning calorimetry (DSC), have some issues. While conventional adiabatic calorimetry has high precision and can be used to determine L at strongly first-order transitions, it can be challenging to achieve a sufficient resolution to characterize $C_p(T)$

close to the second-order phase transition temperature T_C, as well as it requires a large sample mass [82]. However, DSC is widely used due to its ease of operation and small sample size. The issue becomes its necessary scanning rate, typically 1-5 K/min. The drawback of this is a poor temperature resolution and moderate accuracy in determining changes in H. While DSC is very useful for initial survey studies, it is incapable of detailed quantitative measurements near critical phase transitions. Its fast scanning rate does not allow the sample to be close to equilibrium, hence the precise shape of C_p anomalies cannot be obtained [79,83]. Due to these drawbacks, we focus on using high-resolution scanning calorimetry.

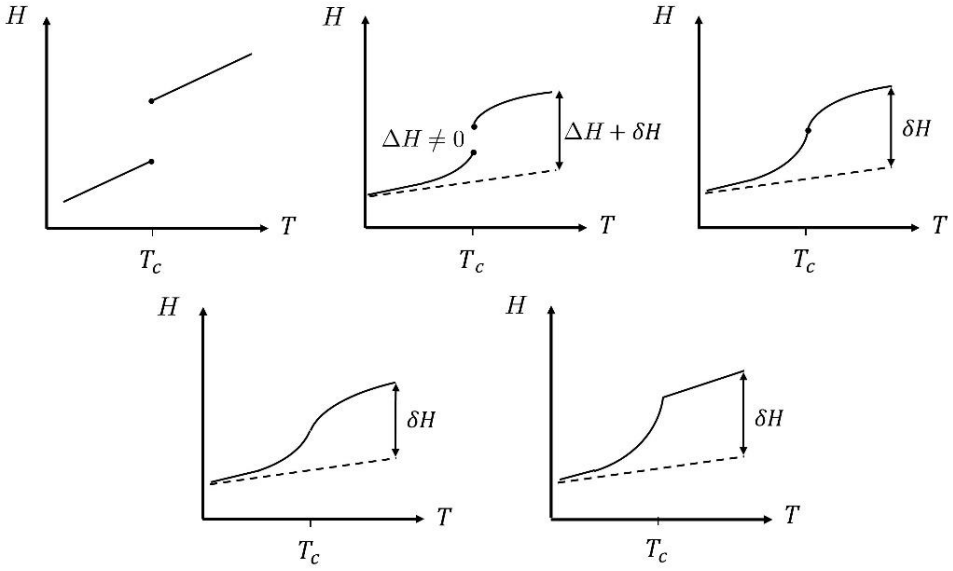

Figure 8: Different types of transitions in terms of enthalpy H. Top row: strong first-order, weakly first-order, and critical. Bottom row: continuous and mean field.

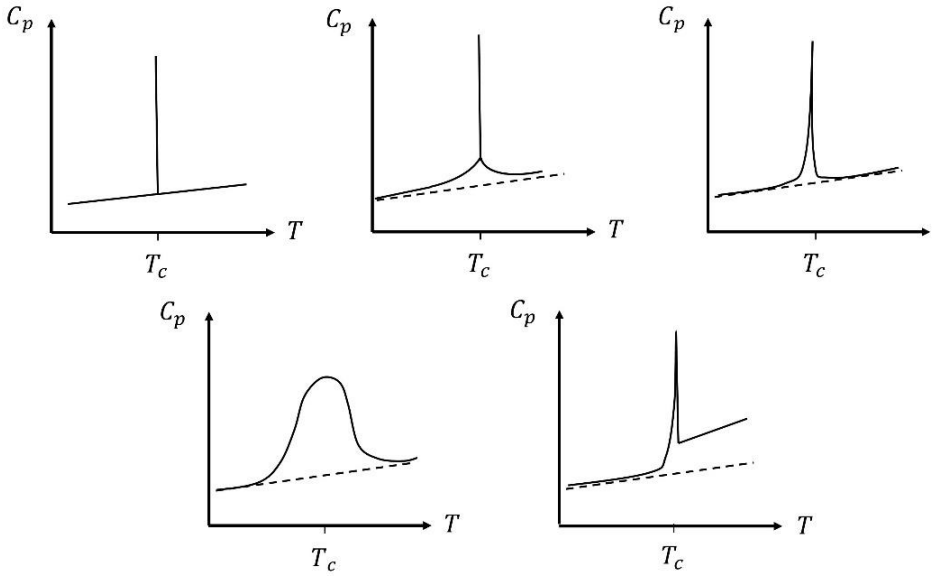

Figure 9: Different types of transitions in terms of heat capacity C_p. Top row: strong first-order, weakly first-order, and critical. Bottom row: continuous and mean field.

Measurements of the temperature dependence of the heat capacity were performed employing a home-made fully automatized dual mode calorimeter. The two high-resolution calorimetry methods are high-resolution AC calorimetry and nonadiabatic relaxation calorimetry [84–87]. The AC mode provides us with precise information on the continuous enthalpy change as a function of temperature. In contrast, the relaxation mode is sensitive to both continuous and discontinuous enthalpy changes at the expense of a somewhat lower resolution.

The calorimetric setup consists of a thermal bath made of two hermetically sealed copper blocks. A Keithley 2002 digital multimeter is used for data acquisition of the supplied power and the resistance of the 500 kΩ thermistor. The heater is connected to the Krohn-Hite model 5920 function generator and a six-decade resistor, which allow adjustments of the signal shape and amount of power supplied to the sample. The bath temperature is set and stabilized by the Lakeshore model 340 temperature controller (Figure 10). The whole setup is remotely controlled by a computer. First, the sample cell is prepared using high-purity silver sheets. An indium paste is applied to both the silver cup and lid, which ensures that the cup and lid are, in a sense, glued together to prevent any possible leakage. Next, the cell is filled with the desired material and sealed by pressing the cup and lid together. Afterward, a 120 Ω resistive heater and 40 μm thick supportive copper wires are attached to the cup-side of the cell using GE varnish. On the lid-side of the cell, a 500 kΩ small glass bead thermistor is glued using a two-component adhesive Torr Seal. The cell is then mounted on the sample holder as shown in Figure 11. The cell is coupled to its surrounding mainly by air and the connecting wires. The whole chamber is insulated from the outside by three thermal shields. The temperature of the internal chamber is stabilized to within ± 0.1 mK by the Lakeshore temperature controller.

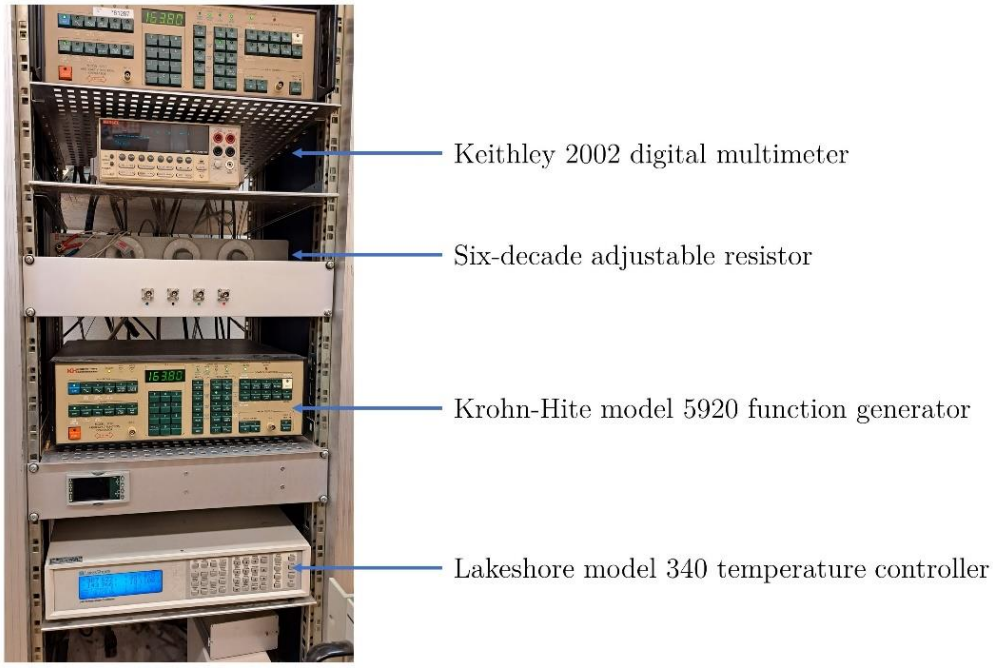

Figure 10: Devices used in the performance of calorimetric measurements.

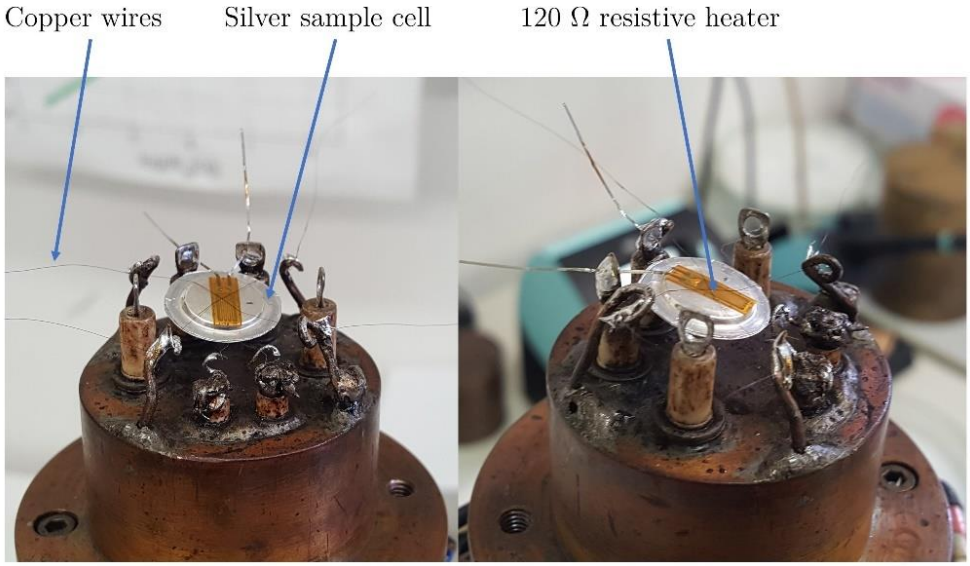

Figure 11: Silver sample cell with attached copper wires and a 120 Ω resistive heater. A 500 kΩ small glass bead thermistor is attached to the underside of the sample cell.

The setup for the high-resolution calorimeter can be depicted by a simple diagram of a thermal system consisting of a sample and a heater (Figure 12). The thin resistive heater is attached to the sample and provides the input power. Both are connected to a temperature-controlled bath stabilized to a specific temperature T_B. The thermal link between the sample and the bath is represented by the thermal resistance R. Such a simple zero-dimensional model can be used when the thermal diffusion time τ_{int} of the sample is sufficiently small so one can neglect any temperature gradients within the sample. The sample temperature $T_S(t)$ is detected by a small bead thermistor attached to the heater on the opposite side of the sample.

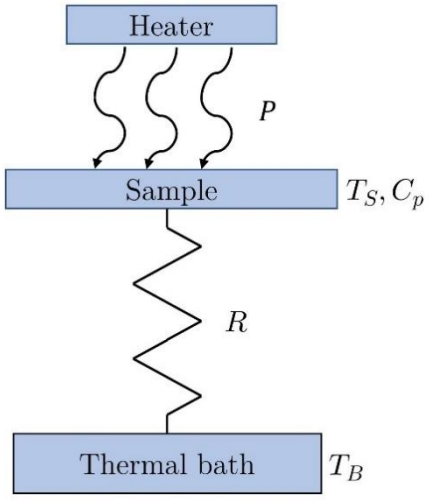

Figure 12: Schematic depiction of a zero-dimensional model consisting of a heater, sample, thermal link, and thermal bath.

Due to the conservation of energy, our thermodynamic process occurring at constant atmospheric pressure can be expressed as:

$$P = C_p^{sys}\frac{dT}{dt} + \frac{dL}{dt} + \frac{T - T_B}{R}. \tag{18}$$

Here P is the power supplied to the sample by a resistive heater, $C_p^{sys} = C_p^{sample} + C_p^{else}$ is the total heat capacity of the sample and everything else connected to the sample, such as wires and a holding cell (if one is required), T is the temperature measured by the small bead thermistor connected to the sample, T_B is the surrounding bath temperature, and L the latent heat. Without any phase coexistence region present, $L = 0$, thus:

$$C_p^{sys} = \frac{dH/dt}{dT/dt} = \frac{P - (T - T_B)/R}{dT/dt}. \tag{19}$$

On the other hand, in the presence of latent heat, one can define an effective heat capacity:

$$C_{p,eff}^{sys} = \frac{P - (T - T_B)/R}{dT/dt}, \tag{20}$$

with the released or absorbed latent heat L involved in the first-order phase transition being given by:

$$\begin{aligned} L &= \int_{T_a}^{T_b} \left[C_{p,eff}^{sys} - (C_p^{coex} + C_p^{else})\right] dT = \\ &= \int_{t_1}^{t_2} \left(P - \frac{T - T_B}{R}\right) dt - \int_{T_a}^{T_b} (C_p^{coex} + C_p^{else}) dT, \end{aligned} \tag{21}$$

where C_p^{coex} is the heat capacity of two coexisting phases over the temperature range from T_a to T_b, and t_1 to t_2 are the times of the appearance and disappearance of the coexistence phase at temperatures T_a and T_b [81].

The AC mode uses a sinusoidal oscillating input power:

$$P = P_0 + P_0 \cos(\omega t). \tag{22}$$

Due to the nonnegligible thermal losses to the surrounding bath, $\frac{T - T_B}{R}$, makes this scanning method nonadiabatic. In equilibrium, the sample temperature can be expressed as a sum of two components:

$$T(t) = T_{dc} + T_{ac}(t). \tag{23}$$

Inserting this expression into Equation (18), one obtains:

$$T_{dc} = T_B + P_0 R, \tag{24}$$

$$T_{ac}(t) = \frac{P_0 R}{1 + (\omega\tau_{ext})^2}\left[\cos(\omega t) + \omega\tau_{ext}\sin(\omega t)\right] = \Delta T_{ac}\sin(\omega t + \varphi), \tag{25}$$

where $\tau_{ext} = RC_p^{sys}$ and φ denotes the phase shift between the input power oscillation and the sample temperature oscillation. In the case of a second-order phase transition (with $L = 0$), the temperature oscillation ΔT_{ac} and the phase shift φ can be expressed as:

$$\Delta T_{ac}(t) = \frac{P_0}{\omega C_p^{sys}} \left(1 + \left(\frac{1}{\omega R C_p^{sys}}\right)^2\right)^{-\frac{1}{2}}, \tag{26}$$

$$\tan \varphi = \frac{1}{\omega R C_p^{sys}}. \tag{27}$$

The heat capacity can thus be written as:

$$C_p^{sys} = \frac{P_0}{\omega \Delta T_{ac}} \cos \varphi. \tag{28}$$

Due to the small, yet nonnegligible phase shift, one can approximate the expression by:

$$(C_p^{sys})^2 \approx \left(\frac{P_0}{\omega \Delta T_{ac}}\right)^2 - \frac{1}{\omega^2 R^2}. \tag{29}$$

The thermal resistance R can be determined either from T_{dc} or from the relaxation mode. The input power oscillation frequency ω has to set in the range:

$$\frac{1}{\tau_{ext}} \ll \omega \ll \frac{1}{\tau_{int}}. \tag{30}$$

In the case of a first-order phase transition, latent heat L is released or absorbed in the coexistence range of a two-phase transformation. The presence of L is seen by an anomalous temperature variation of the sample. A slow release of L in a broad temperature range will not change T_{ac}, but will have a negligible effect on T_{dc}. A fast release of L will rapidly change T_{dc} that will also affect T_{ac} by distorting the harmonic oscillations of the sample temperature. This causes an anomalous variation of φ, which could hint at the nature of the phase transition. For example, the case of a second-order phase transition, φ exhibits a dip, whereas, in the case of a first-order phase transition along the coexistence range, it exhibits a peak. While some qualitative information can be gained from the AC mode, quantitative information about L cannot be obtained. It can, however, be reliably determined in combination with the relaxation mode.

In the relaxation mode, the input power is linearly applied to the sample. In the case of heating:

$$P(t) = \begin{cases} 0, t < 0 \\ \dot{P}t, 0 \leq t \leq t_1 \\ P_0 = \dot{P}t_1, t > t_1 \end{cases}, \tag{31}$$

where $\dot{P} = \frac{dP}{dt}$ is constant. If the power is being reduced in the case of cooling:

$$P(t) = \begin{cases} P_0, t < 0 \\ P_0 + \dot{P}t, 0 \leq t \leq t_1, \\ 0, t > t_1 \end{cases} \tag{32}$$

where $\dot{P}$ is now a negative constant. The variation of the cell's temperature for increasing and decreasing power regimes is given by:

$$T(t) = T_B + R\dot{P}(t - \tau_{ext}) + \tau_{ext} R\dot{P} e^{-\mathrm{t}/\tau_{ext}}, \tag{33}$$

$$T(t) = T_\infty + R\dot{P}(t - \tau_{ext}) + \tau_{ext} R\dot{P} e^{-\mathrm{t}/\tau_{ext}}. \tag{34}$$

The thermal resistance is given by:

$$R = \frac{T_\infty - T_B}{P_0}, \tag{35}$$

where T_∞ is the saturated temperature. The heat capacity $C_{p,eff}^{sys}$ is then calculated using Equation (20) using data obtained from both heating and cooling scans, where P is the power at a given moment of time corresponding to a specific sample temperature T lying in the interval between T_B and T_∞. The derivative dT/dt is obtained by fitting the $T(t)$ data over a short time interval centered at time t. Specifically, the Savitzky-Golay filtering algorithm is used. If the system undergoes a strongly first-order phase transition, the latent heat L is straightforward to determine from Equation (21), since $C_p^{coex} + C_p^{else}$ is roughly constant and is easily approximated by interpolation using slowly varying C_p^{sys} data outside the coexistence region. If the phase transition is weakly first-order with small to moderate amounts of latent heat L, care must be taken when choosing the temperatures T_a and T_b that define the extent of the coexistence region. But these two values can usually be approximately determined from the AC mode. In the two-phase coexistence region, there is a distortion in the wave form of T_{ac}. This results in a characteristic anomaly in the phase shift φ between the input heater power and the sample temperature oscillation.

2.6.2 Liquid crystal-nanoparticle mixture preparation

For the preparation of LC-Au NP mixtures, a well-known mixing protocol is used [88–92]. 200 µl of pure toluene was added to a small amount of LC of mass between m_{LC} = 100-200 mg and mixed well using a glass stirrer. The required amount of a toluene-Au NP solution was added and stirred. The mixture was then slowly heated, using a heating plate, to 80°C and maintained at this temperature for 1 hour. After this, the mixture was again slowly heated to 100°C and maintained at this temperature, until the toluene completely evaporated. If the toluene evaporated too quickly, an additional amount of 100 µl of pure toluene was added to the mixture. Once the toluene was evaporated entirely, the mixture was taken off the heating plate, still at 100°C, and dipped into a bath of cold water. This prevents the NP from being ejected from the LC as it passes through various phases, thus maintaining a good homogeneous mixture.

The Au NPs were prepared and characterized at JSI Department for Material Synthesis by Assist. Prof. Slavko Kralj. In order to functionalize the NP, they were coated with OA. The average diameter of the Au NP is d = 48.9 nm, and was determined using the dynamic light scattering method.

2.6.3 Polarized optical microscopy

Polarized optical microscopy is used to determine and distinguish different LC phases. Observations were performed using a Nikon ECLIPSE LV100ND microscope. Images were taken in real-time using a Nikon DS-Fi3 microscope camera. Heating and cooling scans were performed using a Linkam HFS350EV-PB4 heating stage controlled by a Linkam T96-S temperature controller. Glass holders are made using two glass plates separated with

spacers (Figure 13). In order to minimize any kind of surface effects on the behavior of the LC phases, 100 μm thick spacers were used. Glass plates were treated with polyimide to achieve a planar alignment on the surface.

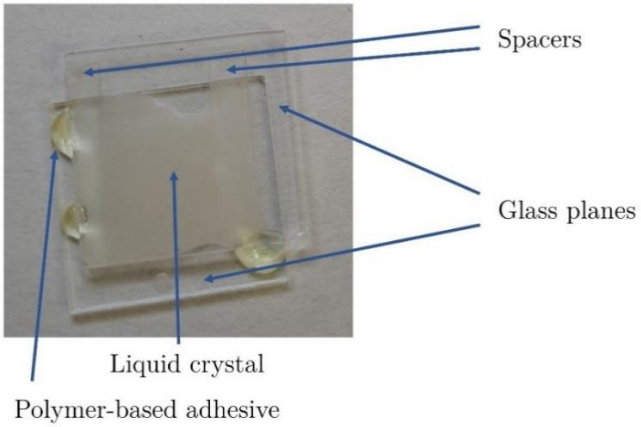

Figure 13: A glass sample holder made from two treated glass plates glued together using a polymer-based adhesive with two spacers in between the plates.

2.7 Simulation of Liquid Crystal Mixtures with Nanoparticles

Studies of thermotropic 5OO8 LC doped with NP of volume concentration ϕ in the diluted regime ($\phi \ll 1$) have been performed using polarized micro-Raman spectroscopy and optical birefringence measurement [48,49,93]. What was shown is that the scalar nematic order parameter S displayed two different regimes on increasing ϕ (Figure 14). In the first regime ($0 < \phi \leq \phi_c$), where $\phi_c = 0.001$, $S(\phi)$ monotonously decreased. However, in the second regime ($\phi_c < \phi < 0.01$), it gradually saturated to a roughly constant value.

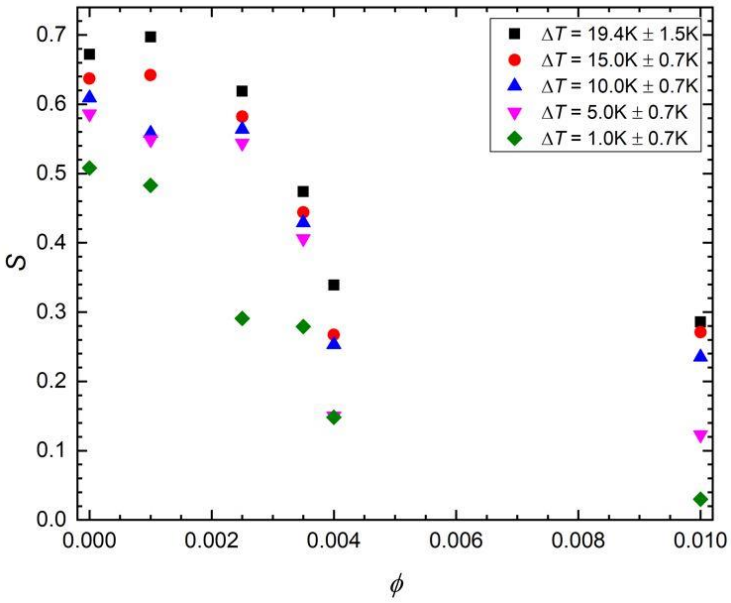

Figure 14: Nematic orientational order parameter S as a function of NP concentration ϕ at different temperatures ΔT below the I to N phase transition temperature T_{IN}.

To reproduce the basic mechanism behind these results, a simple mean-field-type expression at temperature $T = 0$ K for the nematic response in a randomly perturbed N phase is derived. In the above-referenced study, homogeneously dispersed NPs enforce a relatively weak disorder. The simplest possible modeling is used by assuming that NPs enforce, in general, a different local orientation which is roughly mimicked by a kind of random field of constant amplitude. A modified Lebwohl-Lasher-type lattice modelling is used which, despite its simplicity, describes general properties of nematic ordering well [94–96].

A d-dimensional lattice (cases for $d = 2$ and $d = 3$ are studied) of N nematic spins n_i pointing along a local direction of rod-like LC molecules at the site r_i interacting by a Lebwohl-Lasher interaction is considered. The traceless nematic tensor order parameter in d-dimensions is expressed by:

$$\underline{q_i} = \vec{n}_i \bigotimes \vec{n}_i - \frac{1}{d}\underline{I}^{(d)} \tag{36}$$

where $\underline{I}^{(d)}$ is the d-dimensional unit tensor [43]. The global nematic order parameter of the system is defined as:

$$\underline{Q} = S^{(d)}\left(\vec{n}_g \bigotimes \vec{n}_g - \frac{1}{d}\underline{I}^{(d)}\right) = \langle \underline{q_i} \rangle, \tag{37}$$

where $\langle ... \rangle$ stands for the spatial average. The global nematic director $\vec{n}_g$ points along the average nematic director in the system and $S^{(d)}$ stands for the global uniaxial nematic order parameter. NP located at the ith site are set to enforce a local random orientation determined by the tensor:

$$\underline{q_i}^{(NP)} = \vec{e}_i \bigotimes \vec{e}_i - \frac{1}{d}\underline{I}^{(d)}, \tag{38}$$

and the orientations of the unit vectors $\vec{e}_i$ are distributed according to some probability distribution $P(\vec{e}_i)$. In order to determine $S^{(d)}$ Equation (37) is multiplied on both sides by $\vec{n}_g$ to get:

$$\vec{n}_g \cdot \underline{Q}\vec{n}_g = Q_{\alpha\beta}(\vec{n}_g)_\alpha(\vec{n}_g)_\beta = \vec{n}_g \cdot \langle \underline{q_i} \rangle \vec{n}_g = \langle \underline{q_i} \rangle_{\alpha\beta}(\vec{n}_g)_\alpha(\vec{n}_g)_\beta, \tag{39}$$

where the Einstein summation notation is used and indices α and β run from 1 to d. Carrying out the multiplications on both sides and rearranging terms, the obtained expression is:

$$S^{(d)} = \frac{1}{d-1}\langle d(\vec{n}_g \cdot \vec{n}_i)^2 - 1 \rangle. \tag{40}$$

For $d = 2$ and $d = 3$ it follows:

$$S^{(2)} = \langle 2(\vec{n}_g \cdot \vec{n}_i)^2 - 1 \rangle = \langle 2\cos^2(\theta_i) - 1 \rangle = \langle \cos(2\theta_i) \rangle, \tag{41}$$

$$S^{(3)} = \frac{1}{2}\langle 3(\vec{n}_g \cdot \vec{n}_i)^2 - 1 \rangle = \frac{1}{2}\langle 3\cos^2(\theta_i) - 1 \rangle. \tag{42}$$

Note that $S^{(2)} \in \{-1, 1\}$ and $S^{(3)} \in \{-1/2, 1\}$. A perfect nematic order implies $S^{(d)} = 1$ and an isotropic distribution of $\vec{n}_i$ implies $S^{(d)} = 0$. For later convenience, we also introduce:

$$S_{NP}^{(d)} = \frac{1}{d-1}\left(d(\vec{n}_g \cdot \vec{e}_i)^2 - 1\right). \tag{43}$$

In the Lebwohl-Lasher-type lattice model of nematic structures perturbed by impurities, which act as an external field, the energy of the system is expressed as:

$$W = -\frac{1}{2}\sum_{i=1}^{N}\sum_{j=1}^{N} J_{ij}\mathrm{Tr}(\underline{q}_i\underline{q}_j) - \sum_{i=1}^{N} w_i \mathrm{Tr}\left(\underline{q}_i\underline{q}_i^{(NP)}\right). \tag{44}$$

Here, Tr stands for the trace operator and the sum runs over all the lattice sites. The first term describes the interaction between nematic spins. We set $J_{ij} = J_0 > 0$ among the nearest neighbours and $J_{ij} = 0$ for all other pairs, as well as $J_{ii} = 0$. This choice models short-range interactions, enforcing parallel alignment of nematic spins. The second term, initially introduced to study random-anisotropic-nematic (RAN) interactions, describes the interaction between nematic spins and impurities [97]. The effective NP-generated local interaction strength is expressed by w_i and set to $w_i = w_0 > 0$ at the sites where NP are present and $w_i = 0$ everywhere else. In the limit $w_0 \to \infty$, the RAN interaction locally enforces $\vec{n}_i = \vec{e}_i$. Equation (44) can be rewritten as:

$$W = -\sum_{i=1}^{N} Tr(\underline{B}_i\underline{q}_i), \tag{45}$$

where the molecular field tensor is introduced as:

$$\underline{B}_i = \sum_{j=1}^{N} J_{ij}\,\underline{q}_j + w_i\underline{q}_i^{(NP)}. \tag{46}$$

In the classical mean-field approach, the molecular field $\underline{B}_i$ is replaced by an effective molecular field acting on each spin:

$$\underline{B} = J\underline{Q} + w\underline{q}_i^{(NP)}. \tag{47}$$

Here, $J = N_{nn}J_0$, N_{nn} stands for the number of nearest neighboring nematic spins, and $w = \phi w_0$. It is assumed that the local nematic orientation is determined by the effective molecular field. Hence, it is requested that the frames of $\underline{B}$ and $\underline{q}_i$ coincide. In other words, it is requested that $\underline{q}_i = A\underline{B}$. To determine the constant A, the expression $\mathrm{Tr}(\underline{q}_i\underline{q}_i) = C^{(d)} = d - 2 + \frac{1}{d}$ is used. For $d = 2$ and $d = 3$, $C^{(2)} = 1/2$ and $C^{(3)} = 4/3$, respectively. On the other hand:

$$\begin{aligned}\mathrm{Tr}(\underline{q}_i\underline{q}_i) = A^2\mathrm{Tr}(\underline{B}\underline{B}) = A^2\mathrm{Tr}\left(\left(J\underline{Q} + w\underline{q}_i^{(NP)}\right)^2\right) = \\ = C^{(d)}A^2\left((JS^{(d)})^2 + w^2 + 2JwS^{(d)}S_{NP}^{(d)}\right).\end{aligned} \tag{48}$$

Therefore:

$$A = \frac{1}{\sqrt{(JS^{(d)})^2 + w^2 + 2JwS^{(d)}S_{NP}^{(d)}}}. \tag{49}$$

and:

$$\underline{q}_i = \frac{J\underline{Q} + w\underline{q}_i^{(NP)}}{\sqrt{(JS^{(d)})^2 + w^2 + 2JwS^{(d)}S_{NP}^{(d)}}}. \tag{50}$$

Multiplying Equation (50) on both sides by $\vec{n}_g$ we obtain:

$$\vec{n}_g \cdot \underline{q}_i \vec{n}_g = \frac{JS^{(d)} + wS_{NP}^{(d)}}{\sqrt{(JS^{(d)})^2 + w^2 + 2JwS^{(d)}S_{NP}^{(d)}}}. \tag{51}$$

Finally, the spatial average of Equation (51) is taken, which yields the self-consistent integral equation for $S^{(d)}$ given probability distribution $P(\vec{e}_i)$:

$$S^{(d)} = \frac{1}{\Omega^{(d)}} \int P(\vec{e}_i) \frac{JS^{(d)} + wS_{NP}^{(d)}}{\sqrt{(JS^{(d)})^2 + w^2 + 2JwS^{(d)}S_{NP}^{(d)}}} d\Omega^{(d)}. \tag{52}$$

The integration is carried out over all possible orientations of $\vec{e}_i$, $\Omega^{(d)} = \int d\Omega^{(d)}$ is the solid angle in d-dimensional space, and $\frac{1}{\Omega^{(d)}} \int P(\vec{e}_i) d\Omega^{(d)} = 1$. We also assume a cylindrically symmetric distribution of $\vec{e}_i$ values about $\vec{n}_g$. Consequently:

$$S^{(2)} = \frac{1}{\pi} \int_0^{\pi} P\big(\cos(\alpha_i)\big) \frac{JS^{(2)} + wS_{NP}^{(2)}}{\sqrt{(JS^{(2)})^2 + w^2 + 2JwS^{(2)}S_{NP}^{(2)}}} d\alpha_i, \tag{53}$$

$$S^{(3)} = \frac{1}{2} \int_{-1}^{1} P\big(\cos(\alpha_i)\big) \frac{JS^{(3)} + wS_{NP}^{(3)}}{\sqrt{(JS^{(3)})^2 + w^2 + 2JwS^{(3)}S_{NP}^{(3)}}} d\big(\cos(\alpha_i)\big), \tag{54}$$

where α_i is the angle between $\vec{e}_i$ and $\vec{n}_g$. Note that Equation (52) yields $S^{(d)} = 1$ for $w = 0$, and in the limit $w \to \infty$ for an isotropic distribution $P(\vec{e}_i)$ it follows $S^{(d)} = 0$. We calculate $S = S^{(3)}$ as a function of $w = \phi w_0$ for different distributions P. A step-like distribution $P(\alpha \leq \alpha^{(max)}) = P_0$ and $P(\alpha > \alpha^{(max)}) = 0$, where P_0 is imposed as constant. As can be seen in Figure 15, the $S(\phi)$ dependence monotonously decreases with increasing ϕ, displaying a relatively steep crossover between the two regimes, characterized by significantly different characteristic values of S. The saturated value of S in the second (plateau) regime monotonously decreases with increasing $\alpha^{(max)}$ and is finite for $\alpha^{(max)} < \frac{\pi}{2}$. We also note that the behavior shown in Figure 15 is relatively robust with respect to the shape of $P(\alpha)$. For example, in Figure 15c, we compare $S(\phi)$ behavior for a step-like and Gaussian distribution. As can be seen, both distributions reproduce the essential behavior $S(\phi)$.

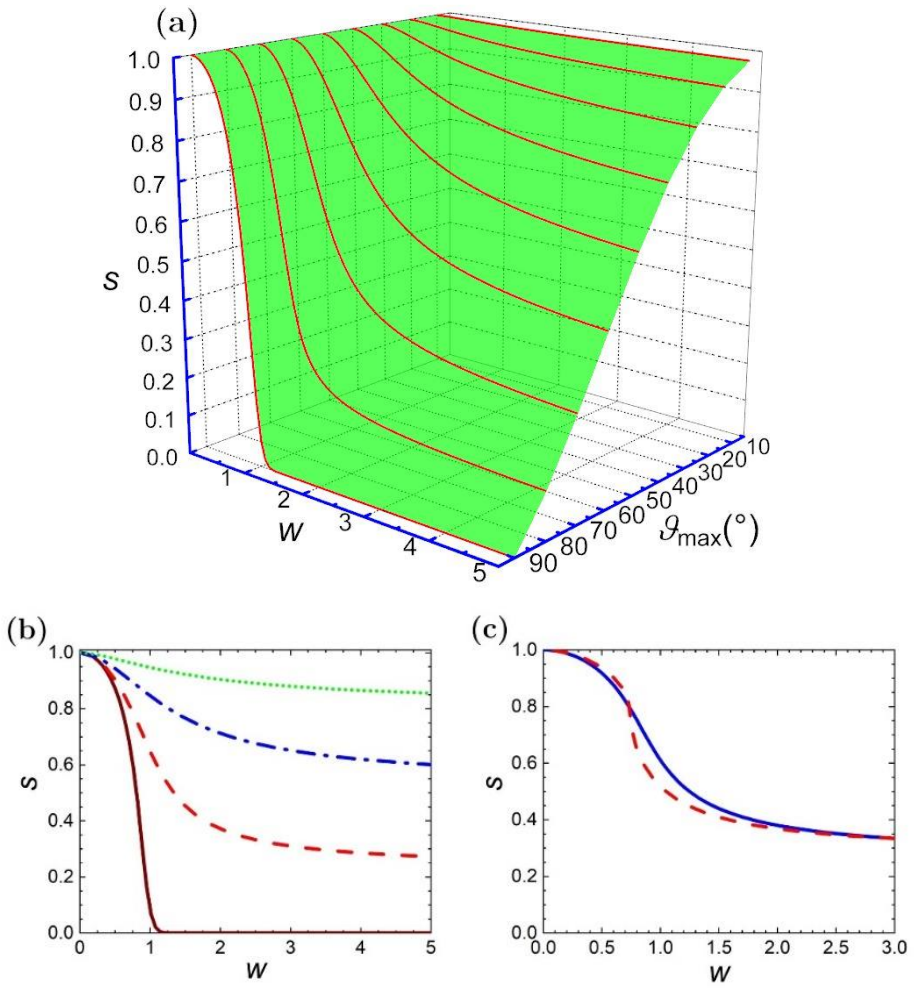

Figure 15: a, b) Order parameter variation as a function of w and ϑ_{max}. b) Full line: $\vartheta_{max} = \pi/2$, dashed line: $\vartheta_{max} = 7\pi/18$, dash-dotted line: $\vartheta_{max} = \pi/3$, dotted line: $\vartheta_{max} = 2\pi/9$. c) Comparison of $S(w)$ dependences for a step-like (full line) and the Gaussian probability distribution (dashed line). The step-like distribution is described by $P_{NP}(\vartheta \leq \vartheta^{(max)}) = P_0$ and $P_{NP}(\vartheta > \vartheta^{(max)}) = 0$, where P_0 is a constant, and the Gaussian distribution is described by $P_{NP} = P_G(\vartheta) = Ce^{-\vartheta^2/2\sigma^2}/\sqrt{2\pi\sigma^2}$, where C is the normalization constant and σ is the standard deviation. Both probability distributions must be normalized on the interval from $\vartheta = 0$ to $\vartheta = \pi$. This condition gives us the value of $P_0 = 1/\vartheta^{(max)}$. To determine σ we solve the equation $\vartheta^{(max)} = \int_0^\pi e^{-\vartheta^2/2\sigma^2}\, d\vartheta$ and to determine C we solve the equation $\int_0^\pi Ce^{-\vartheta^2/2\sigma^2}/\sqrt{2\pi\sigma^2}\, d\vartheta = 1$. We chose ϑ_{max} for both distributions in such a way as to roughly match the observed drop in experimentally measured $S(p)$ dependence. For the step-like distribution $\vartheta_{max} = 0.387\ \pi$, while for the Gaussian distribution $\sigma = 0.798$ and $C = 0.499$. These parameters were used to match typical experimentally measured quantitative features roughly.

2.8 Nanoparticle-Induced Stabilization of Twist Grain Boundary A Phase

Introducing NPs into an LC system that contains defects could enhance the stability of such a system. The two mechanisms enabling such a stabilization are referred to as the DCR mechanism and the ADCT mechanism [52,59,88,98–100]. The DCR mechanism refers to a partial filling of the energetically expensive TD core volume with the volume of the trapped NPs. Within these TD cores, the nematic order in disclinations or the smectic order in dislocations are essentially melted [101–103]. Generally, this introduces a relatively high-energy penalty in the condensation term of free energy. However, if NPs are trapped within the TD cores, the free energy penalty is reduced, making this configuration energetically favorable. We must note that not all types of NPs are appropriate for exploiting the DCR mechanism. The appropriate ones are the ones that do not significantly distort the surrounding nematic director field $\vec{n}(\vec{r})$ or smectic phase field $\phi(\vec{r})$. The more universal ADCT mechanism refers to the case when NP are able to stabilize both LC systems with disclinations and dislocations [59,104]. NP should only slightly distort the surrounding LC structure in order to be attracted toward the TD cores. In the opposite case, introducing NP would cause a too severe energy penalty and would be immediately ejected from the LC. Also, they should only slightly distort the surrounding LC order once trapped in the TD core. To achieve the universality of being able to target both disclinations and dislocations, an appropriate surface treatment of the NP must be performed [52,59,88,89,100].

2.8.1 Twist grain boundary A phase in pure chiral *n*FBTFO$_1$M$_7$ (n = 9, 10, 11)

The *n*FBTFO$_1$M$_7$ LC belong to the optically active series 3-fluoro-4-(S)-1-methylheptyloxy4'-(4''-alkyloxy-3''-fluorobenzoyloxy)tolanes [105]. The TGB$_A$ phase is shown to exist in all the derivatives from heptyloxy ($n = 7$) to octadecyloxy ($n = 18$). We shall only focus on the $n = 9$, 10, and 11 derivatives, the chemical formulas of which are presented in Figure 16.

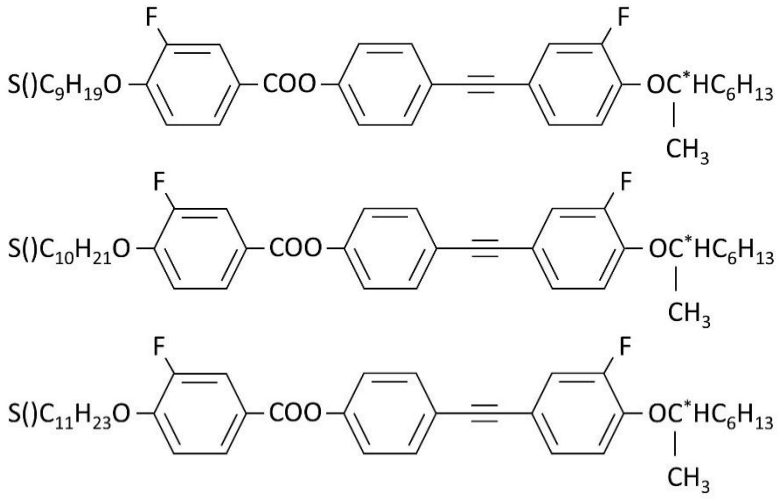

Figure 16: Chemical formulas from top to bottom: 9FBTFO$_1$M$_7$, 10FBTFO$_1$M$_7$, and 11FBTFO$_1$M$_7$.

2.8.1.1 Heat capacity measurement results of chiral *n*FBTFO$_1$M$_7$ (n = 9, 10, 11)

High-resolution heat capacity measurements of a pure 9FBTFO$_1$M$_7$ under a cooling run show two peaks in the $c_p(T)$ profile at 375.2 K and 380.0 K. The relatively sharp high temperature peak is associated with the combined blue phases (BP) BPI, BPII, and BPIII, with the N* phase lying on the low-temperature wing and the I phase at the high-temperature wing. The broad low-temperature peak is associated with the chiral line liquid phase (N$_L^*$), a TGB$_A$ phase structure of shorter-range order. On the high-temperature wing lies the N* phase, and on the low-temperature wing lies the TGB$_A$ phase, followed by the SmA phase at a lower temperature. A pure 9FBTFO$_1$M$_7$ displays the I - BP - N* - N$_L^*$ - TGB$_A$ - SmA - C LC phase sequence (Figure 17).

High-resolution heat capacity measurements of a pure 10FBTFO$_1$M$_7$ under a cooling run similarly show two peaks in the $c_p(T)$ profile at 377.5 K and 381.7 K. The very large and narrow high temperature c_p peak is associated with the BP phases (BPI, BPII, and BPIII), with the N* and I phases lying on the lower and higher temperature wing, respectively. The broad lower temperature c_p peak is, as in the case of 9FBTFO$_1$M$_7$, associated with the transition between the low-temperature N$_L^*$ phase and high-temperature N* phase. Further down the low-temperature wing lies the TGB$_A$ phase, followed by the SmA and SmC* phases. A pure 10FBTFO$_1$M$_7$ displays the I - BP - N* - N$_L^*$ - TGB$_A$ - SmA - SmC* - C LC phase sequence (Figure 18).

High-resolution heat capacity measurements of a pure 11FBTFO$_1$M$_7$ under a cooling run show a sharp peak in the $c_p(T)$ profile at 378.4 K associated with the BP phases (BPI, BPII, and BPIII). Unlike in the previous two samples, the broad lower temperature c_p peak associated with the N$_L^*$ phase displays a very smeared-out transition. The value of the c_p appears to plateau for a range of 1 K until a small but noticeable drop associated with the N$_L^*$-N* transition is observed. At 370.2 K, a nearly mean field-type transition between the SmC* and the TGB$_A$ phases is observed. A pure 11FBTFO$_1$M$_7$ displays the I - BP - N* - N$_L^*$ - TGB$_A$ - SmC* - C LC phase sequence (Figure 19).

One can construct a phase diagram from these high-resolution heat capacity measurements, presented in Figure 20. The discrepancy in phase transition temperatures with respect to the heat capacity measurements performed by Bouchta et al. [105] is due to them using differential scanning calorimetry with a relatively fast cooling rate of 0.5 K/min, which leads to a poor temperature resolution. We do not show the phase diagram obtained from POM, as supportive POM measurements were only taken to identify the phases and did not have sufficient resolution and they were not performed under same conditions, i.e., instead of thicker bulk samples used in C_p measurements, much more thinner cells were used in POM, which might slightly change the transition temperature [106].

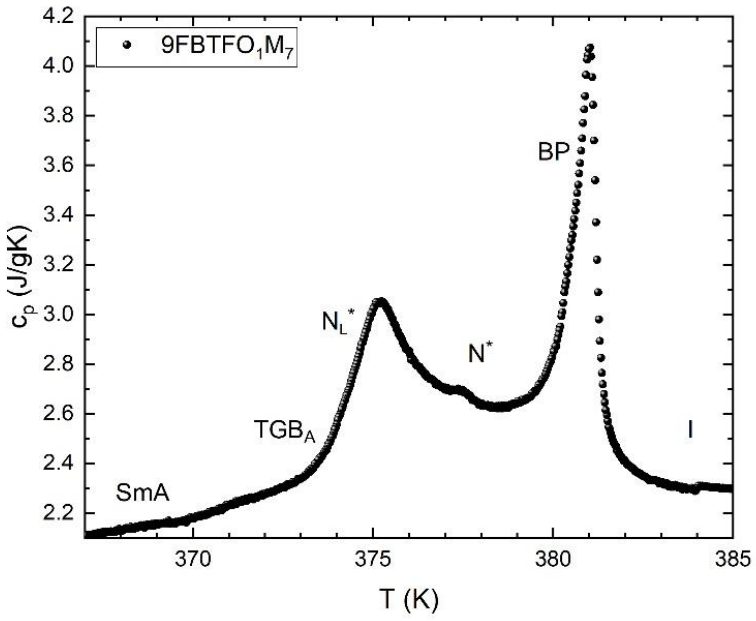

Figure 17: AC calorimetry results of the specific heat capacity c_p for a pure sample of $9FBTFO_1M_7$.

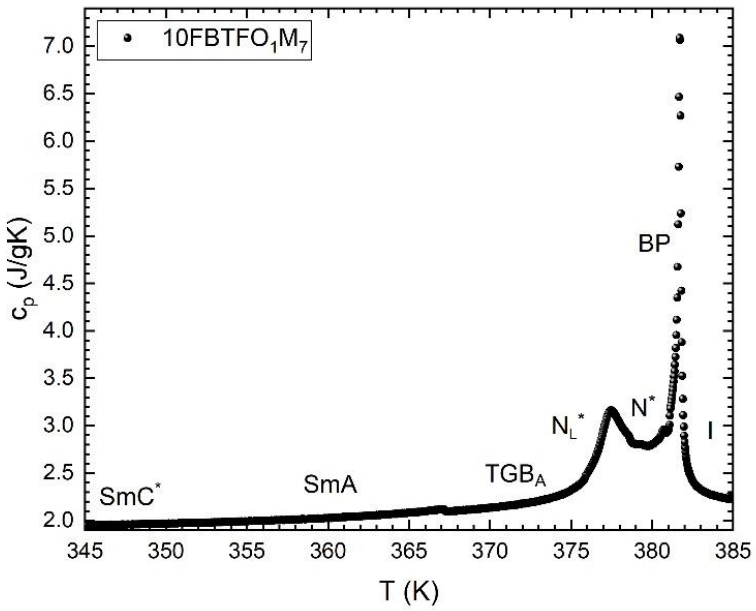

Figure 18: AC calorimetry results of the specific heat capacity c_p for a pure sample of $10FBTFO_1M_7$.

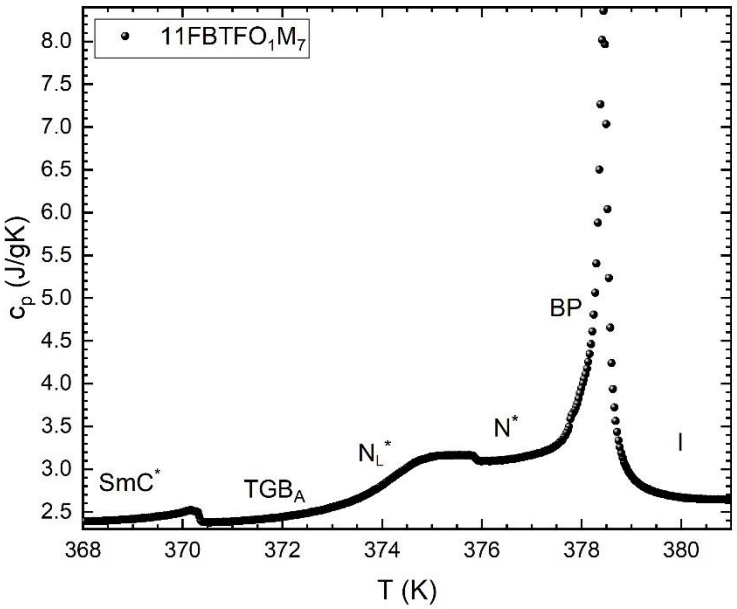

Figure 19: AC calorimetry results of the specific heat capacity c_p for a pure sample of 11FBTFO$_1$M$_7$.

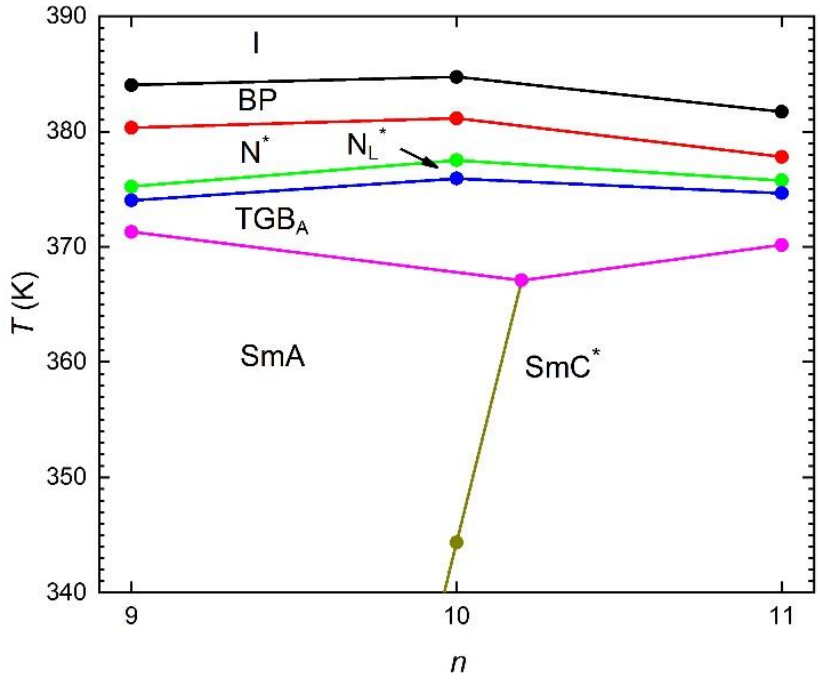

Figure 20: Phase diagram $n - T$ of the nFBTFO$_1$M$_7$ ($n = 9$, 10, 11) based on the results obtained from the AC calorimetry measurements.

2.8.2 Mixtures of 9FBTFO$_1$M$_7$ with spherical Au nanoparticles

This section presents the high-resolution heat capacity measurement results of 9FBTFO$_1$M$_7$-Au NP mixtures, followed by the polarized optical microscopy (POM) measurement results. Mixtures with a mass concentration of $\chi = 0.005$ and $\chi = 0.010$ were synthesized according to the mixing protocol described in Section 1.6.2. The mass concentration is defined as $\chi = m_{NP}/(m_{NP} + m_{LC})$. The measurement data were obtained by performing an AC calorimetry cooling run at a 200 mK/h cooling rate. POM was used in order to determine the type of LC phases present in the sample. The glass cell preparation procedure for planar alignment on the surface is described in Section 1.6.3.

2.8.2.1 High-resolution heat capacity measurement results of mixtures of 9FBTFO$_1$M$_7$ with spherical Au nanoparticles

The 9FBTFO$_1$M$_7$ $c_p(T)$ profile displays two peaks, with the higher temperature one being weakly first-order and the lower temperature one being second-order, displaying the SmA - TGB$_A$ - N$_L^*$ - N* phase sequence (Figure 21), typical of LC with a stable TGB$_A$ phase [59,89,107]. The existence of these phases was confirmed using polarized microscopy. The presence of Au NPs does not alter this phase sequence. It does, however, change the temperature range where these phases occur, as can be seen from the $c_p(T)$ profile. The phase transitions are shifted towards lower temperatures with increasing χ. The high-temperature peak decreases and broadens out, tending towards a second-order transition. Centering the $c_p(T)$ profiles along $T - T_{N_L^*-N^*}$ we can compare the temperature range of the combined TGB$_A$ + N$_L^*$ phases. From Figures 22 and 23, it is evident that the SmA-TGB$_A$ phase transition is barely noticeable in the $c_p(T)$ profiles. It appears that the SmA-TGB$_A$ phase transition is strongly a first-order transition. Additional data from the phase shift φ (Equation (27)) was required to determine the location of the phase transition point (Figure 24). We observe that the phase transition point shifts downwards and away from the N$_L^*$-N* phase transition point, thereby increasing the combined temperature range of the TGB$_A$ + N$_L^*$ phases by approximately 1.55 K and 1.95 K for $\chi = 0.005$ and $\chi = 0.010$, respectively. Based on the calorimetric measurements, the $\chi - T$ phase diagram for 9FBTFO$_1$M$_7$ + Au NP mixtures is presented in Figure 25. It is clearly seen that the presence of NP increases the temperature range of the combined TGB$_A$ + N$_L^*$ phases. The trend also indicates a slowing down of the temperature range increase. A further increase in χ would not drastically improve the temperature stability.

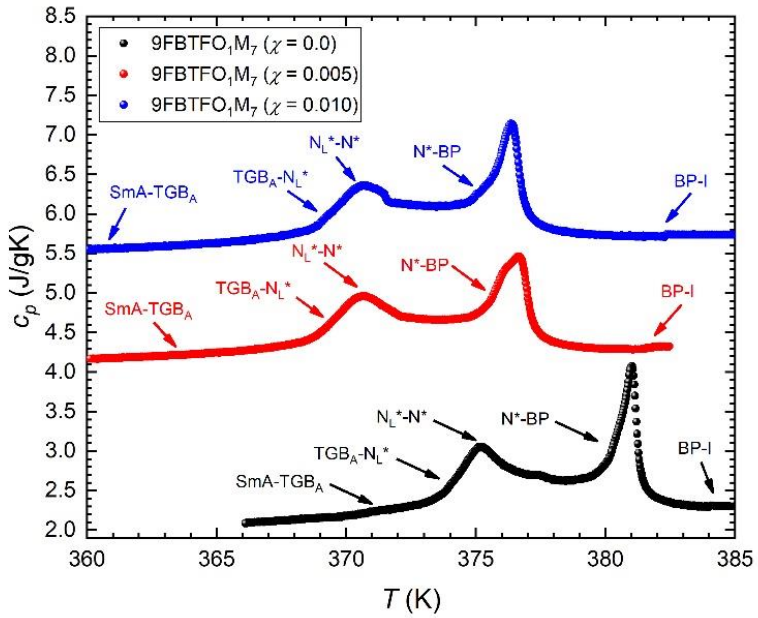

Figure 21: AC calorimetry results of the specific heat capacity c_p for 9FBTFO$_1$M$_7$-Au NP mixtures ($\chi = 0.0$, $\chi = 0.005$, and $\chi = 0.010$) as a function of temperature T. The temperature profiles were obtained by cooling the samples at a 200 mK/h rate. The $c_p(T)$ profiles for $\chi = 0.005$, and $\chi = 0.010$ are shifted upwards for a better comparison.

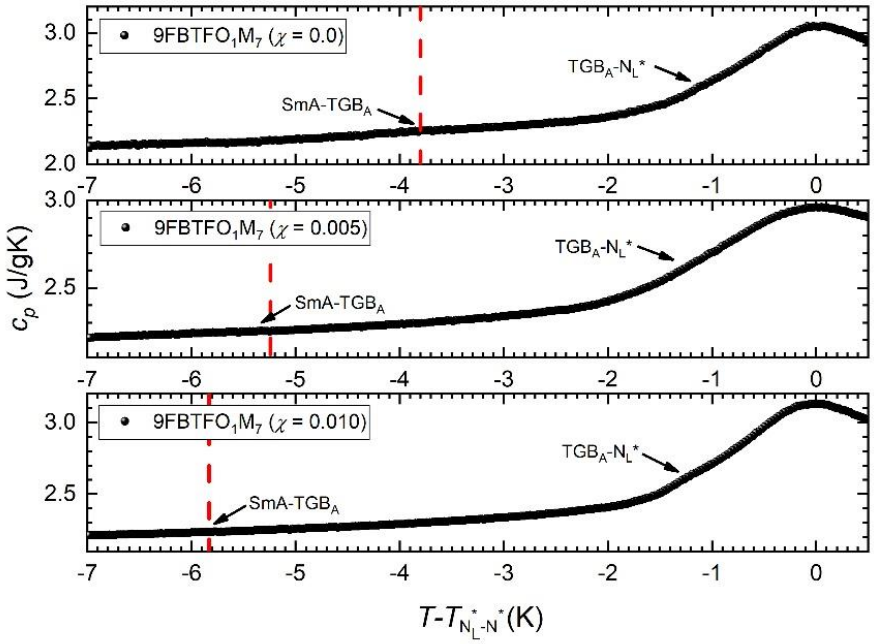

Figure 22: AC calorimetry results of the specific heat capacity c_p for 9FBTFO$_1$M$_7$-Au NP mixtures ($\chi = 0.0$, $\chi = 0.005$, and $\chi = 0.010$) as a function of temperature $T - T_{N_L^*-N^*}$. The red line, representing the SmA - TGB$_A$ phase transition point, is seen to be shifting towards lower values.

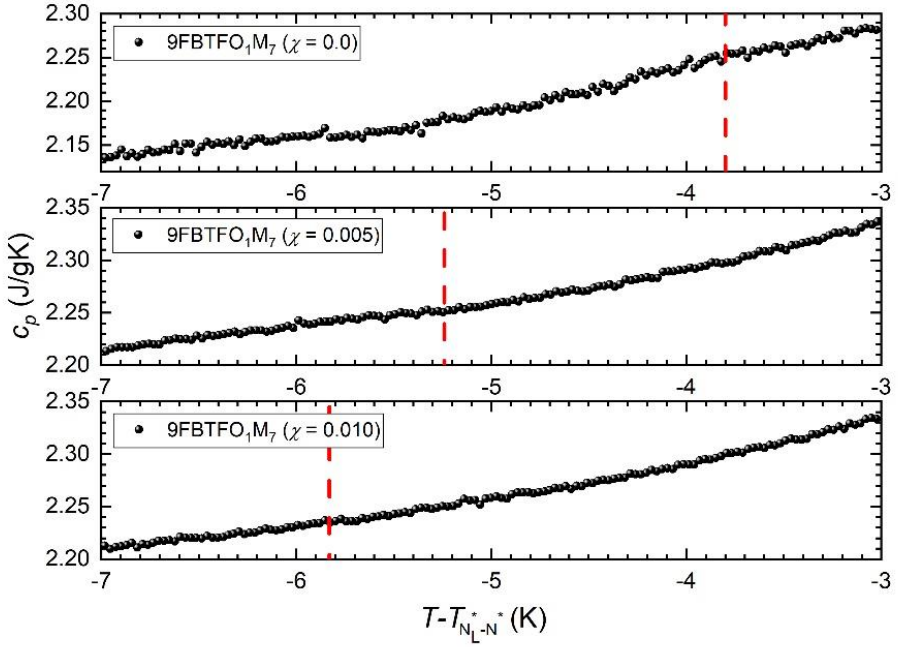

Figure 23: AC calorimetry results of the specific heat capacity c_p for 9FBTFO$_1$M$_7$-Au NP mixtures ($\chi = 0.0$, $\chi = 0.005$, and $\chi = 0.010$) as a function of temperature $T - T_{N_L^*-N^*}$. The red line, representing the SmA - TGB$_A$ phase transition point, is seen to be shifting towards lower values.

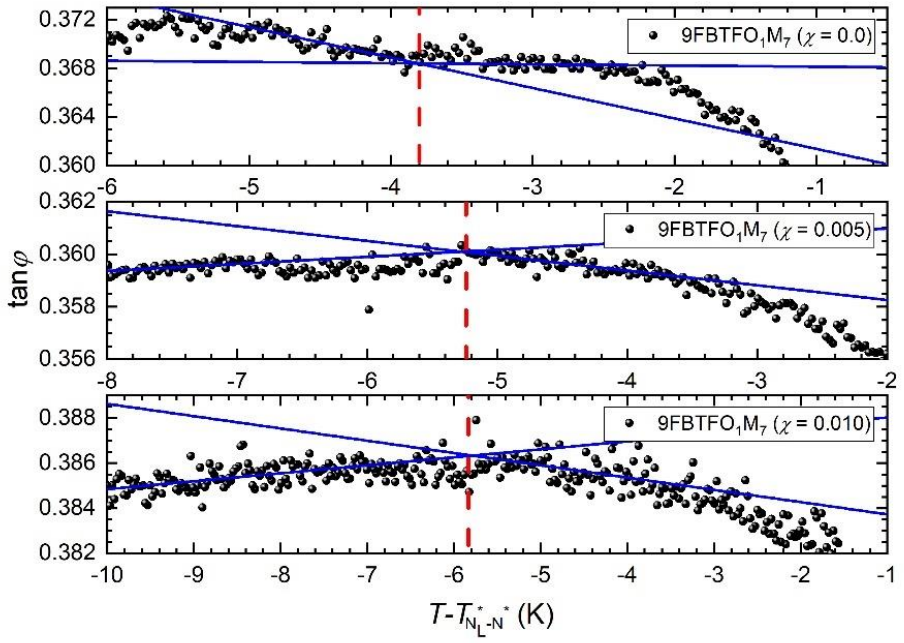

Figure 24: AC calorimetry results of $\tan\varphi$ as a function of temperature $T - T_{N_L^*-N^*}$, where φ is the phase shift. These measurements are required to determine the temperature point of the SmA - TGB$_A$ phase transition. The blue tangent lines are fitted to determine the slope change which represents the phase transition point.

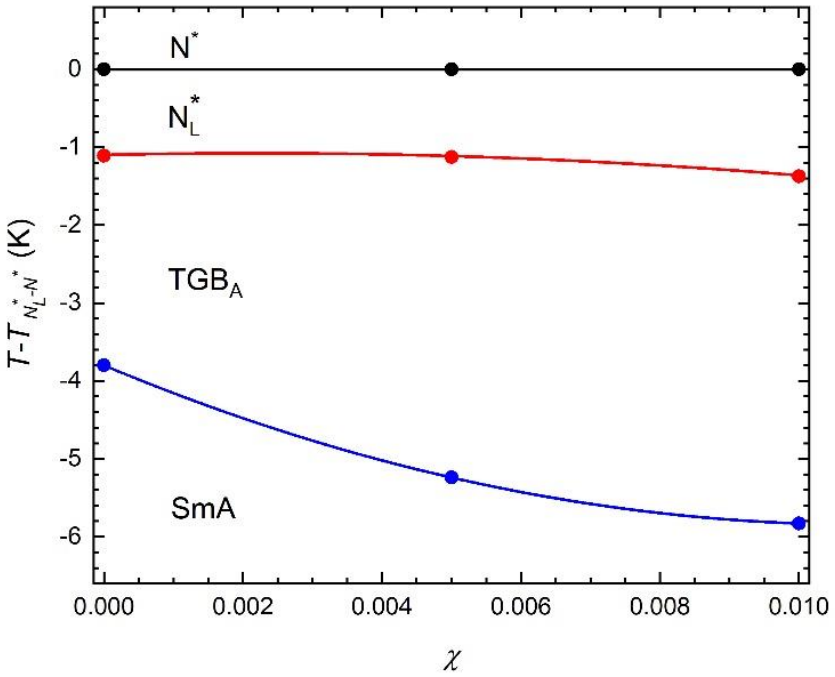

Figure 25: The $\chi - T$ phase diagram for 9FBTFO$_1$M$_7$-Au NP mixtures.

2.8.2.2 Polarized optical microscopy measurement results of mixtures of 9FBTFO$_1$M$_7$ with spherical Au nanoparticles

The set of images (Figure 26) shows the N* - N$_L^*$ - TGB$_A$ - SmA phase sequence in 9FBTFO$_1$M$_7$-Au NP mixtures upon cooling the samples. The N* phase displays a thread-like and occasional oily-streak texture [108,109]. The N$_L^*$ phase, similar to the N* phase, displays a thread-like texture but with a pronounced color modulation in the Grandjean orientation [108]. The helical axis of the smectic layers is parallel to the light propagation, leading to different colors. Upon further cooling, the TGB$_A$ phase with a relatively long pitch is observed [108]. Lastly, a mostly homogeneous SmA phase is observed, with some remnants of the TGB$_A$ phase still as a color modulation [108].

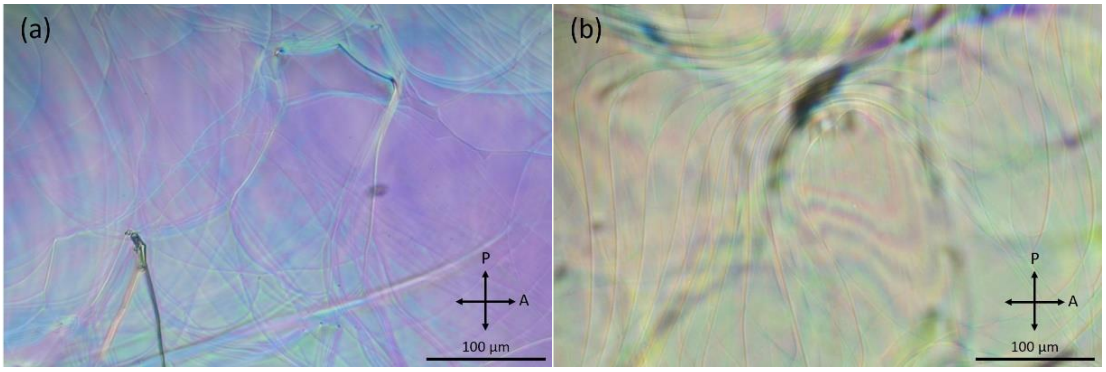

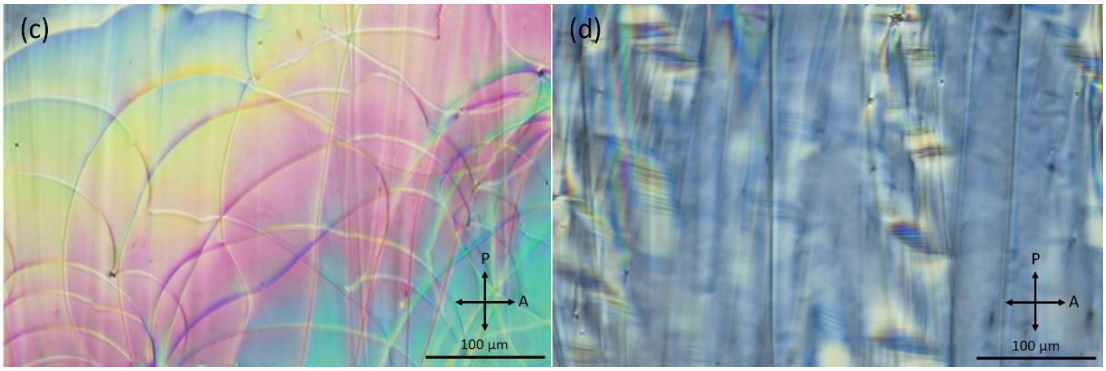

Figure 26: The POM images of the N* (a), N_L* (b), TGB_A (c), and SmA phases (d) observed in 9FBTFO$_1$M$_7$-Au NP mixtures.

2.8.3 Mixtures of 10FBTFO$_1$M$_7$ with spherical Au nanoparticles

This section presents the high-resolution heat capacity measurement results of 10FBTFO$_1$M$_7$-Au NP mixtures, followed by the POM measurement results. Mixtures with a mass concentration of $\chi = 0.01$ and $\chi = 0.02$ were synthesized. The measurement data was obtained by performing an AC calorimetry cooling run at a 200 mK/h cooling rate. POM was used in order to determine the type of LC phases present in the sample.

2.8.3.1 High-resolution heat capacity measurement results of mixtures of 10FBTFO$_1$M$_7$ with spherical Au nanoparticles

The 10FBTFO$_1$M$_7$ displays the same phase sequence on the lower temperature wing of the second-order peak as 9FBTFO$_1$M$_7$ but with an additional SmC* - SmA phase transition being present at lower temperatures (Figure 27). Again, as for 9FBTFO$_1$M$_7$, the temperature ranges of the LC phases are shifted towards lower temperatures, with the exception of the SmC* phase, which remains relatively static or even shifts slightly towards higher temperatures as we increase χ. By aligning the $c_p(T)$ profiles along the phase transition temperature $T_{N_L^*-N^*}$, we can observe the shift of the SmA - TGB_A phase transition point towards lower values, thereby increasing the temperature range in which the combined TGB_A + N_L* are stable by 2.66 K and 4.77 K for $\chi = 0.01$ and $\chi = 0.02$, respectively (Figure 28 and 29). Compared to the SmA - TGB_A phase transition in 9FBTFO$_1$M$_7$, the phase transition is clearly observable with a distinct mean-field-like shape that begins to round as we increase χ. In addition, the SmC* - SmA phase transition point is being shifted towards higher values, thereby shrinking the temperature range in which the SmA phase is stable. This might suggest that by increasing χ we are approaching a triple point. A similar observation, when it comes to the rounding of the c_p anomaly was obtained by Thanassoulas et al. [110]. On the other hand, contrary to our observations, they observed an increase in the temperature range of the SmA phase and a reduction in the SmC* phase. There might be multiple causes for this discrepancy: the LC compound used was CE8, with an exceptionally stable SmA phase in a range over 50 K, and the nanoparticles used were CdSe nanoparticles surface-treated with oleylamine (OA) and tri-octylphosphine. Figure 30 shows the $\chi - T$ phase diagram for 10FBTFO$_1$M$_7$-Au NP mixtures. Similarly, as for 9FBTFO$_1$M$_7$, the temperature range of the combined TGB_A + N_L* phases is greatly increased. It can also be seen that the temperature range of the SmA phase is decreasing, approaching a TGB_A - SmA - SmC* triple point.

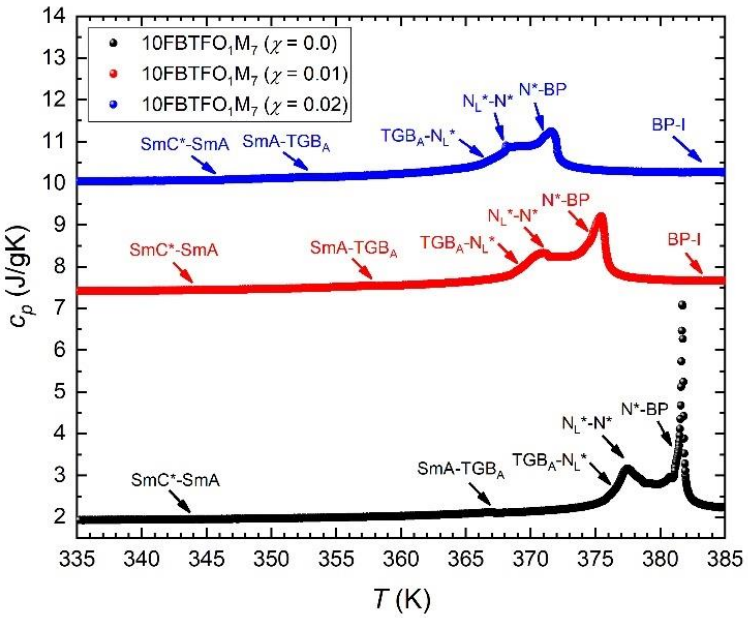

Figure 27: AC calorimetry results of the specific heat capacity c_p for 10FBTFO$_1$M$_7$-Au NP mixtures ($\chi = 0.0$, $\chi = 0.01$, and $\chi = 0.02$) as a function of temperature T. The temperature profiles were obtained by cooling the samples at a 200 mK/h rate. The $c_p(T)$ profiles for $\chi = 0.01$, and $\chi = 0.02$ are shifted upwards for a better comparison.

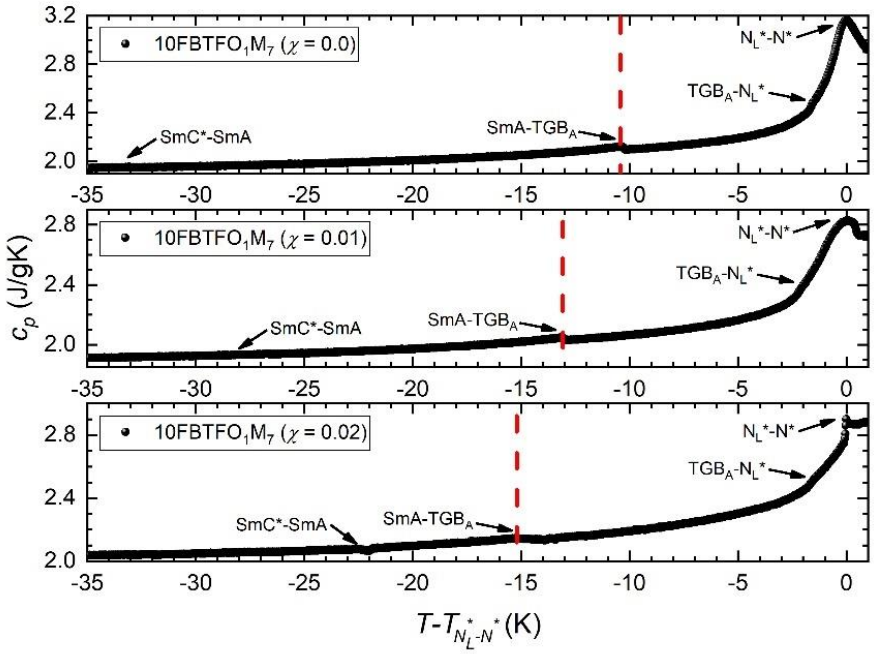

Figure 28: AC calorimetry results of the specific heat capacity c_p for 10FBTFO$_1$M$_7$-Au NP mixtures ($\chi = 0.0$, $\chi = 0.01$, and $\chi = 0.02$) as a function of temperature $T - T_{N_L^*-N^*}$. The red line, representing the SmA - TGB$_A$ phase transition point, is seen to be shifting towards lower values.

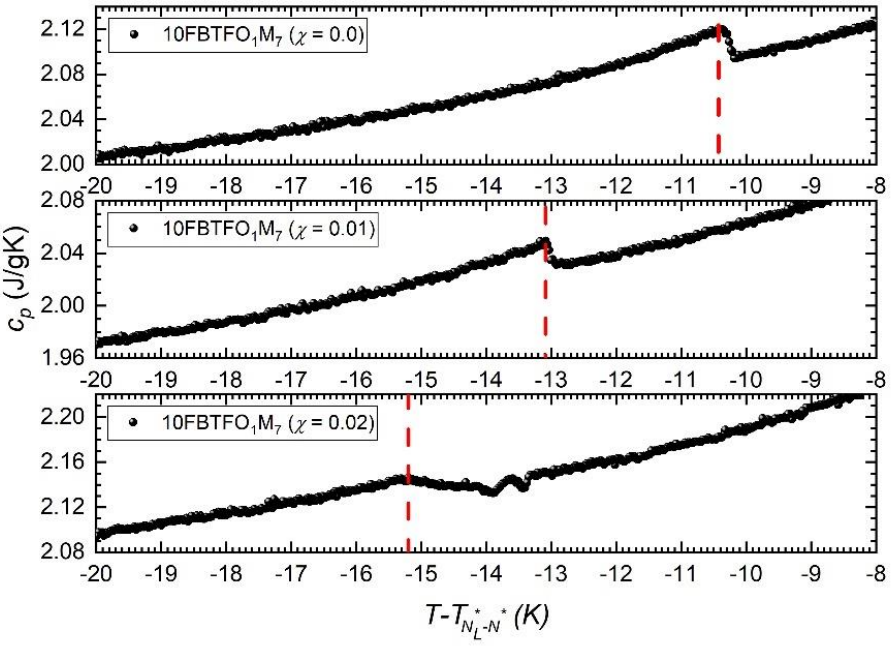

Figure 29: AC calorimetry results of the specific heat capacity c_p for 10FBTFO$_1$M$_7$-Au NP mixtures ($\chi = 0.0$, $\chi = 0.01$, and $\chi = 0.02$) as a function of temperature $T - T_{N_L^*-N^*}$. The red line, representing the SmA - TGB$_A$ phase transition point, is seen to be shifting towards lower values.

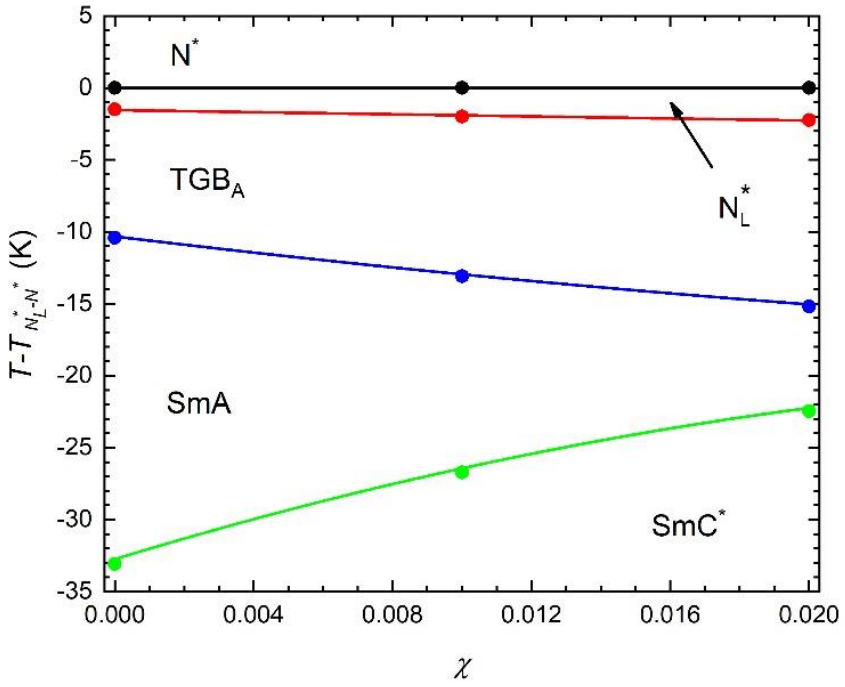

Figure 30: The $\chi - T$ phase diagram for 10FBTFO$_1$M$_7$ + Au NP mixtures.

2.8.3.2 Polarized optical microscopy measurement results of mixtures of 10FBTFO$_1$M$_7$ with spherical Au nanoparticles

The set of images (Figure 31) shows the N*- N$_L^*$- TGB$_A$ - SmA - SmC* phase sequence in 10FBTFO$_1$M$_7$-Au NP mixtures upon cooling the samples. The LC textures observed in these samples are similar to the ones observed in 9FBTFO$_1$M$_7$-Au NP mixtures. The N* phase displays a thread-like and oily-streak texture, with the thread-like texture still present in both N$_L^*$ and TGB$_A$ phases with the addition of a color modulation in the Grandjean orientation [108,109]. Further cooling from the SmA phase, the SmC* phase displays a typical SmA phase fan-shaped texture superimposed by a line pattern due to the helical superstructure [108].

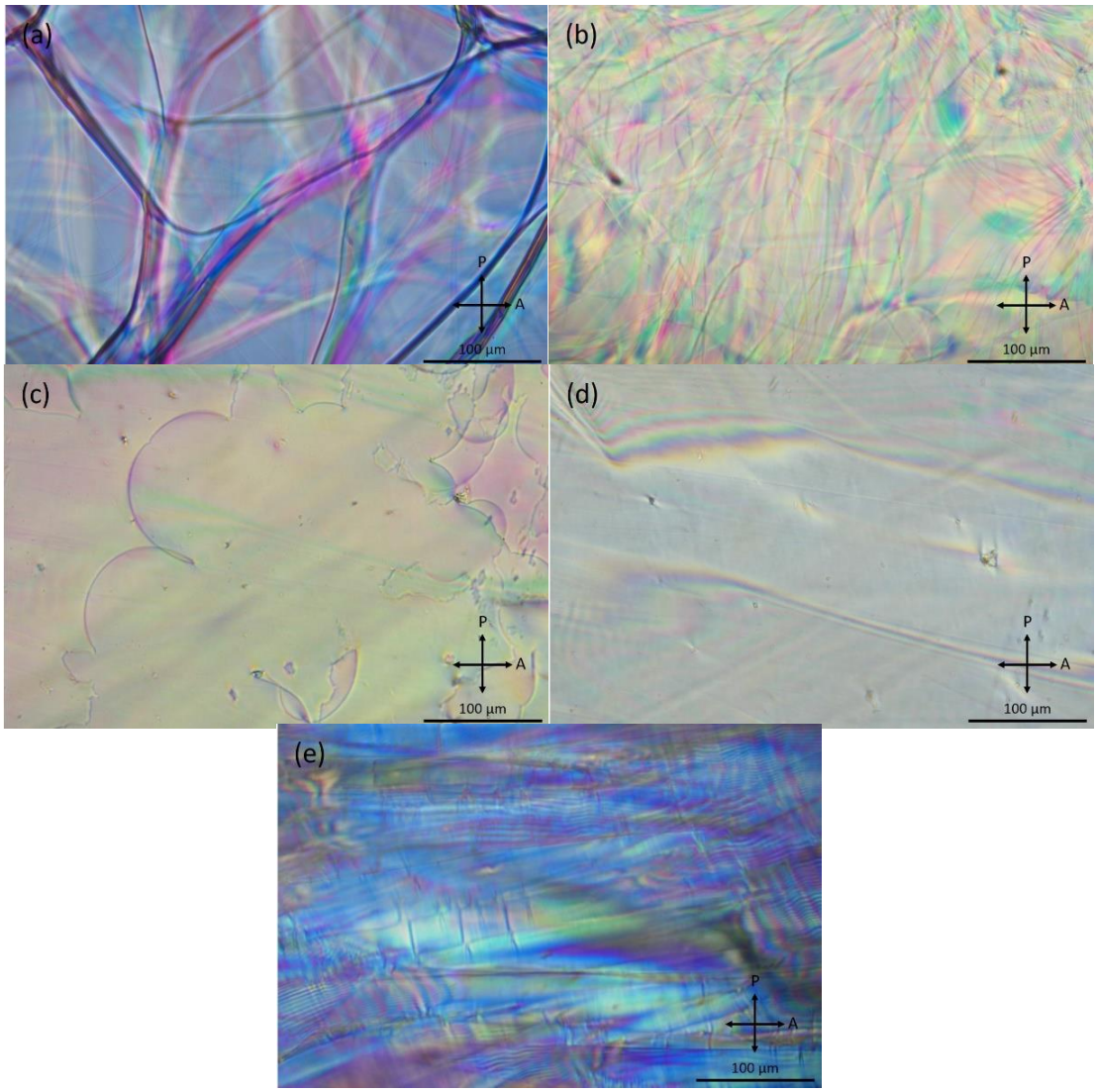

Figure 31: The POM images of the N* (a), N$_L^*$ (b), TGB$_A$ (c), SmA (d), and SmC* phases (e) observed in 10FBTFO$_1$M$_7$-Au NP mixtures.

2.8.4 Mixtures of 11FBTFO$_1$M$_7$ with spherical Au nanoparticles

This section presents the high-resolution heat capacity measurement results of 11FBTFO$_1$M$_7$-Au NP mixtures, followed by the POM measurement results. Mixtures with a mass concentration of $\chi = 0.005$ and $\chi = 0.010$ were synthesized. The measurement data

was obtained by performing an AC calorimetry cooling run at a 200 mK/h cooling rate. POM was used in order to determine the type of LC phases present in the sample.

2.8.4.1 High-resolution heat capacity measurement results of mixtures of 11FBTFO$_1$M$_7$ with spherical Au nanoparticles

In the case of 11FBTFO$_1$M$_7$, the low-temperature wing of the second-order peak displays only the TGB$_A$ - N$_L^*$ - N* phase sequence, with the SmC* phase appearing further at lower temperatures (Figure 32). As in both previous cases, the presence of NP causes a shift in the temperature ranges of the LC phases towards lower values. Aligning the $c_p(T)$ profiles along the phase transition temperature $T_{N_L^*-N^*}$, we can determine whether there has been an increase in the temperature range of the combined TGB$_A$ + N$_L^*$ phase. In Figures 33 and 34, we can observe that there is a slight shift of the SmC* - TGB$_A$ phase transition point, thereby increasing the temperature range of the TGB$_A$ + N$_L^*$, by 0.11 K and 0.28 K for $\chi = 0.005$ and $\chi = 0.010$, respectively. This increase is not as pronounced as in the cases of 9FBTFO$_1$M$_7$ and 10FBTFO$_1$M$_7$, where the shift occurred in the SmA - TGB$_A$ phase transition point. It would seem that the presence of NP does have a significantly larger impact on the stability of the SmC* phase, given that the NP-stabilized TGB$_A$ phase does not encroach substantially into the SmC* phase, compared to the SmA phase. It has been demonstrated that homogeneously dispersed NPs alter the average layer spacing in smectics, leading to elastic distortions that are energetically costly for the system [91,111]. We also observe the rounding of the mean-field-like c_p anomaly with increasing χ. Figure 35 shows the $\chi - T$ phase diagram for 11FBTFO$_1$M$_7$-Au NP mixtures. Unlike in our two previous cases, the temperature range of the combined TGB$_A$ + N$_L^*$ phase barely increases with increasing χ.

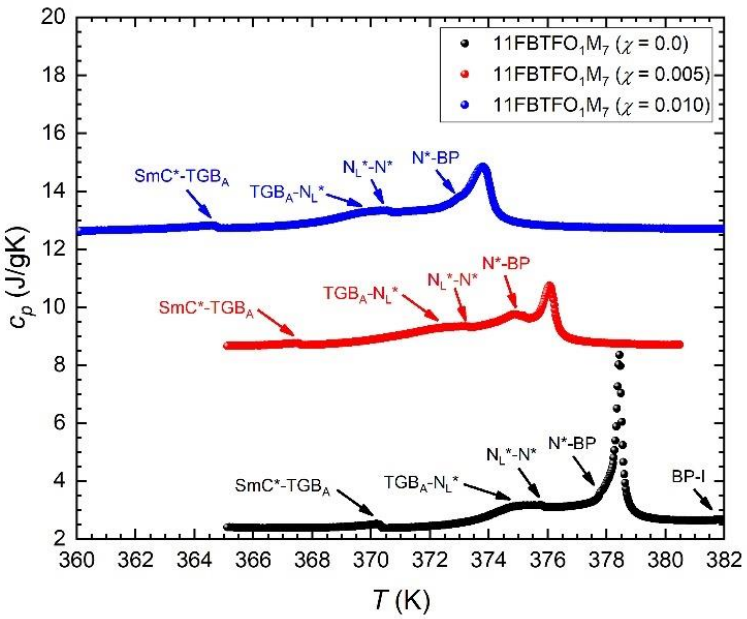

Figure 32: AC calorimetry results of the specific heat capacity c_p for 11FBTFO$_1$M$_7$-Au NP mixtures ($\chi = 0.0$, $\chi = 0.005$, and $\chi = 0.010$) as a function of temperature T. The temperature profiles were obtained by cooling the samples at a 200 mK/h rate.

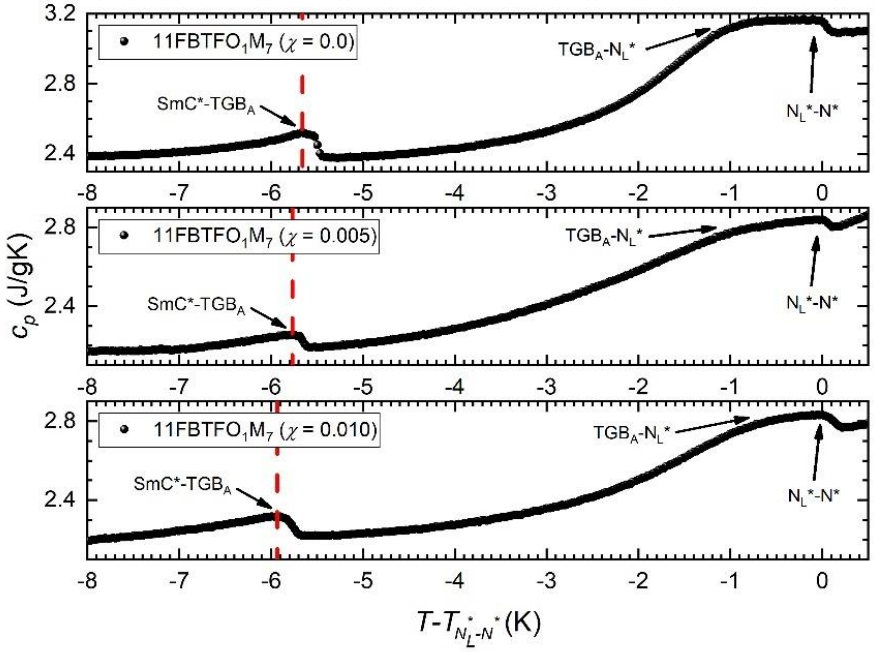

Figure 33: AC calorimetry results of the specific heat capacity c_p for 11FBTFO$_1$M$_7$-Au NP mixtures ($\chi = 0.0$, $\chi = 0.005$, and $\chi = 0.010$) as a function of temperature $T - T_{N_L^*-N^*}$. The red line, representing the SmA - TGB$_A$ phase transition point, is seen to be shifting towards lower values.

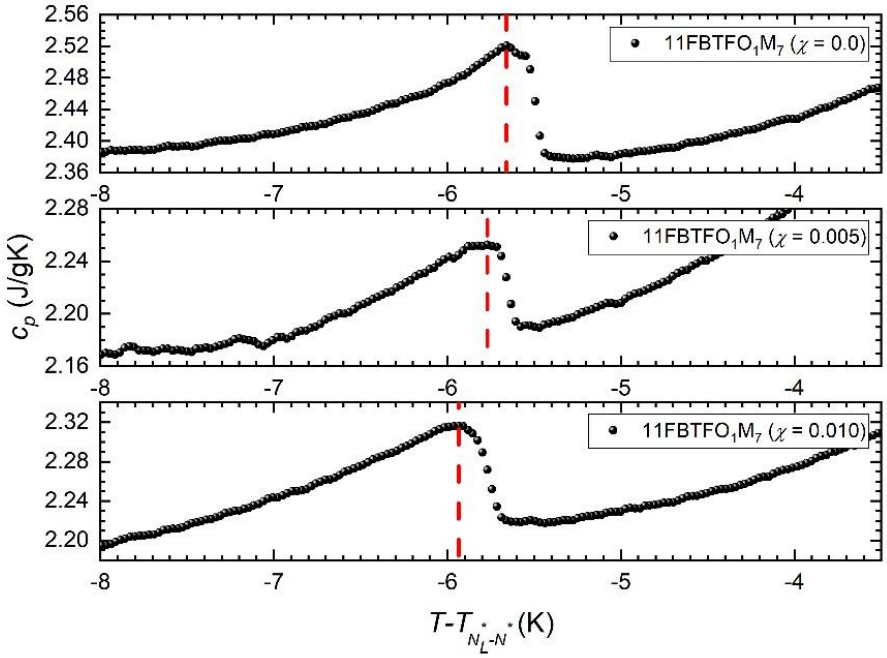

Figure 34: AC calorimetry results of the specific heat capacity c_p for 11FBTFO$_1$M$_7$-Au NP mixtures ($\chi = 0.0$, $\chi = 0.005$, and $\chi = 0.010$) as a function of temperature $T - T_{N_L^*-N^*}$. The red line, representing the SmA - TGB$_A$ phase transition point, is seen to be shifting towards lower values.

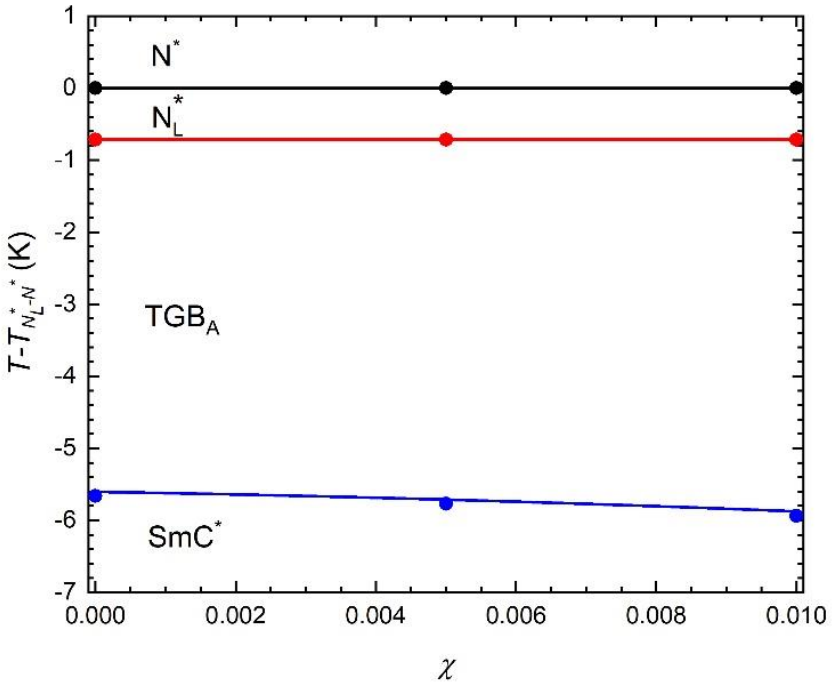

Figure 35: The $\chi - T$ phase diagram for 11FBTFO$_1$M$_7$-Au NP mixtures.

2.8.4.2 Polarized optical microscopy measurement results of mixtures of 11FBTFO$_1$M$_7$ with spherical Au nanoparticles

The set of images (Figure 36) shows the N*- N$_L^*$- TGB$_A$ - SmC* phase sequence in 11FBTFO$_1$M$_7$-Au NP mixtures upon cooling the samples. Analogous to the previous two sets of images, the textures for the N*, N$_L^*$, TGB$_A$, and SmC* phases display the same features.

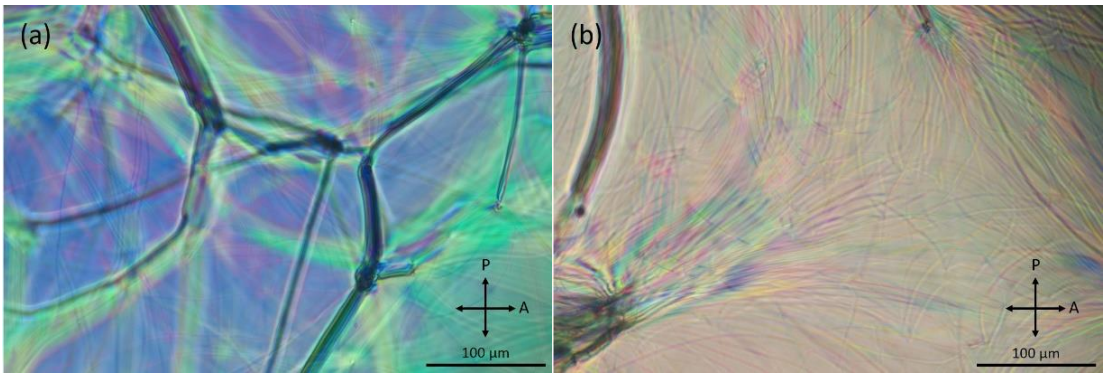

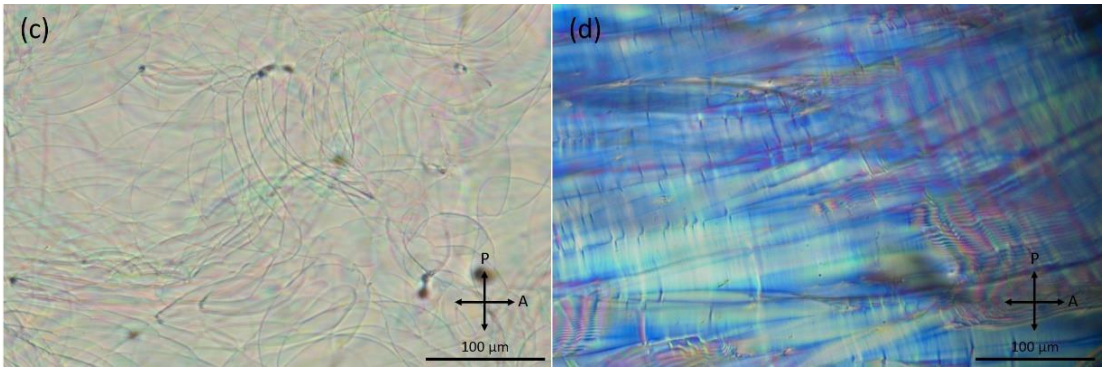

Figure 36: The POM images of the N* (a), N_L^* (b), TGB_A (c), and SmC^* phases (d) observed in 11FBTFO$_1$M$_7$-Au NP mixtures.

2.8.5 Discussion of results

The high-resolution calorimetry and POM results of nFBTFO$_1$M$_7$-Au NP mixtures ($n = 9$, 10, 11) demonstrate that homogeneously dispersed surface-functionalized Au NP can effectively stabilize the TGB_A phase with its defect line structures in the form of grain boundaries. As previously mentioned, the stabilizing effect appears via the ADCT mechanism, as is demonstrated in other works [50,52,88,89,92,98,100]. The ADCT mechanism combines the so-called DCR mechanism and the adaptive nature of the surface-functionalized NP with respect to the surrounding LC ordering.

The descriptive power of the DCR mechanism was first shown in the case of defect stabilization in the BP phases. Specifically, randomly shaped polymer coils were used to stabilize disclination lines in BP phases [98]. It was demonstrated that substituting the energetically costly essentially melted isotropic cores of the disclination line with polymer coils reduced the free energy penalty of said disclination lines. The thermal energy required to form disclination lines is reduced, thereby stabilizing the LC system thermodynamically.

There is also an additional mechanism by which NP-induced stabilization of LC phases with topological defects can occur. It has been demonstrated that the saddle-splay elasticity in the presence of NP can also contribute to the stabilization of the TGB_A phase, due to the introduction LC-NP interfaces [59,89,100]. A simple Landau-de Gennes-Ginzburg mesoscopic model introduced by S. Kralj is used to estimate the impact of NPs on the stability of the TGB_A phase. The free energy is expressed as the sum of volume and surface contribution:

$$F = \iiint f_V d^3\vec{r} + \oiint f_i d^2\vec{r}. \tag{55}$$

The volume integral is carried out over the whole LC body. In contrast, the surface integral is carried out over the surface of the confining volume of the LC body and over any NP-LC interfaces. The volume free energy density f_V is expressed as the sum:

$$f_V = f^{(n)} + f^{(s)} + f_{el}, \tag{56}$$

with $f^{(n)}$, $f^{(s)}$, and f_{el} being the nematic, smectic, and Frank elastic free energy densities expressed in Equations (5), (11), and (13), respectively. The f_i term represents the surface density interaction. Considering only bulk LC samples, f_i will determine the local NP-LC interface interaction.

Adding NP of concentration χ to an LC sample with smectic ordering, one expects that NP will cause a dilation of the smectic layers. Minimizing the compressibility term ($C_\perp$) in Equation (11), we get the condition:

$$q_0\vec{n} = \nabla\phi. \tag{57}$$

Applying $\nabla\times$ to both sides of Equation (57), one obtains $q_0\nabla\times\vec{n} = \nabla\times\nabla\phi = 0$. The issue becomes strongly chiral LCs, since $\nabla\times\vec{n}\neq 0$. This frustration can be resolved by either melting the smectic order or by introducing dislocations into the LC system. Since the TGB_A phase has a non-zero smectic ordering, NP must remain predominately within the melted cores of screw dislocations. Thus, the free energy condensation term will be decreased due to the DCR mechanism. It is estimated that this decrease is:

$$F_c^{(TGB)}(\chi) = \left|f^{(s)}(\eta_s)\right|\left(V_{LC} - V_{sd}^{(tot)}\right) - \left|f^{(s)}(\eta_s)\right|V_{NP}^{(tot)}, \tag{58}$$

with η_s being the equilibrium smectic order in the absence of any dislocations, V_{LC} the volume of the LC, $V_{sd}^{(tot)}$ the total volume of the melted defect cores, and $V_{NP}^{(tot)}$ the total volume occupied by the trapped NP [59,100].

Observing the radial distribution of the nematic director field from the center of an isolated screw dislocation, one sees that the configuration is reminiscent of the double twist distortions found within BP phases compared to a single twist found in cholesterics (Figure 37) [112]. In a chiral LC, the elastic free energy $f^{(n)}$ is composed of the achiral nematic terms plus an additional chiral term proportional to the twist term ($\vec{n}\cdot\nabla\times\vec{n}$). Let us assume $\vec{n} = (\cos(q_0 z), \sin(q_0 z), 0)$ representing a single twist configuration. It turns out that the f_{el} becomes a linear combination of the twist (K_2) and saddle-splay (K_{24}) terms, with the twist term providing a favorable contribution to the free energy and the saddle-splay term providing an unfavorable contribution. On the other hand, a double-twist configuration could be expressed as $\vec{n} = (-q_0 y, q_0 x, 1)/\sqrt{1+{q_0}^2(x^2+y^2)}$. The only non-zero term in the elastic free energy is the twist term, providing a favorable contribution. However, it is impossible to fill the whole space with a double twist configuration which forces the system to form disclination lines within a finite amount of space. These impose an elastic penalty on the free energy [113]. Comparing both configurations, the favorable contributions are the same, while the unfavorable are different. Whether the LC system will prefer one configuration over the other will be determined by the saddle-splay term, more specifically on the value of K_{24}, which can be expressed as surface free energy along the disclination lines as internal surfaces [114]. In order to estimate the impact of NP on the saddle-splay term, it is best to express $\vec{n}$ in the cylindrical coordinate system as $\vec{n} = (0, \sin\theta(\rho), \cos\theta(\rho))$. One can approximately take $\theta(\rho) = \tan^{-1}\left(1/(\rho q_0)\right)$ in the limit $\rho/d \gg 1$, where d is the average smectic layer spacing [115]. The saddle-splay free energy per unit cell volume can be approximately expressed as:

$$\frac{F_{24}^{(TGB)}(\chi_V)}{V} \sim -\frac{K_{24}\chi_V a_{24}}{2rd}, \tag{59}$$

where χ_V refers to the volume concentration of NP instead of the mass concentration χ, r is the typical radius of NP, and a_{24} is a dimensionless quantity:

$$a_{24} = \frac{1}{4\pi^2[1+1/(4\pi r^2/d^2)]^2(r/d)^3}. \tag{60}$$

The presence of NP clearly leads to a decrease in the saddle-splay free energy term. Simple calculations demonstrate that the saddle-splay term contribution is by an order of magnitude larger than the contribution of the ADCT mechanism [50,89].

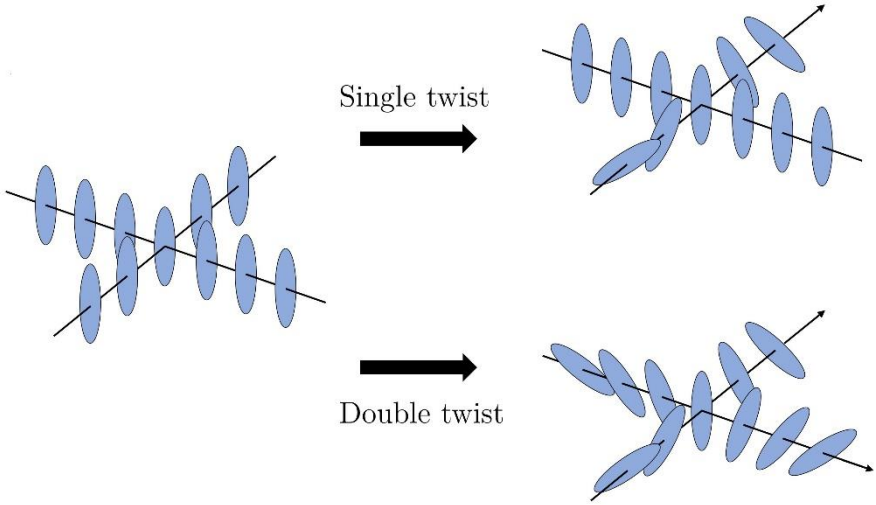

Figure 37: A regular nematic structure forming either a single twist structure typical for N* phases or a double twist structure typical for BP phases in chiral LC.

Comparing $\chi - T$ phase diagrams presented in Figures 25, 30, and 35, the TGB_A - SmA phase transition point in $9FBTFO_1M_7$ initially decreases and plateaus as we increase χ, while the TGB_A - SmC^* phase transition point in $11FBTFO_1M_7$ remains virtually static. In $10FBTFO_1M_7$, the SmA phase existence region shrinks as the TGB_A and SmC^* phase existence range expands, trending towards TGB_A - SmA - SmC^* triple point. This phenomenon could be explained when one constructs the $n - T$ phase diagram. Figure 38 shows the $n - T$ phase diagrams for pure samples ($\chi = 0.0$) and for LC-Au NP mixtures with $\chi = 0.01$. The nearly vertical line separating the SmA and SmC^* phases can be thought of as a kind of morphotropic phase boundary (MPB) analogous to the MPB in ferroelectrics separating regions with a tetragonal symmetry from those of rhombohedral symmetry by varying the composition of the ferroelectric [116–121]. Ferroelectrics in the vicinity of the MPB display enhanced dielectric properties, while piezoelectric materials display enhanced electromechanical properties [122,123]. This is the consequence of the free energy surface being nearly spherically degenerate along the MPB, facilitating easy polarization rotation and a metastable coexistence range for the tetragonal and rhombohedral phases [124,125]. The presence of a large enough electric field can then drive the sample to transition between energetically similar configurations. In the case of nFBTFO$_1$M$_7$, the varying composition is represented by the number of carbon atoms in the terminal chain (n) and the driving external "field" being the Au NP mass concentration χ. Since the $10FBTFO_1M_7$ sample lies in the vicinity of this MPB, the SmA and SmC^* phases are energetically degenerate. As we have previously mentioned, NPs are predominantly located within defect lines, since the modulation of smectic layers is energetically costly. This implies that the TGB_A and SmC^* phases with their dislocations are energetically more desirable configurations than the SmA phase, where the presence of NPs causes an energetically unfavorable smectic layer modulation. Therefore, a small amount of NPs is enough to drive the system from the SmA phase towards the SmC^* phase.

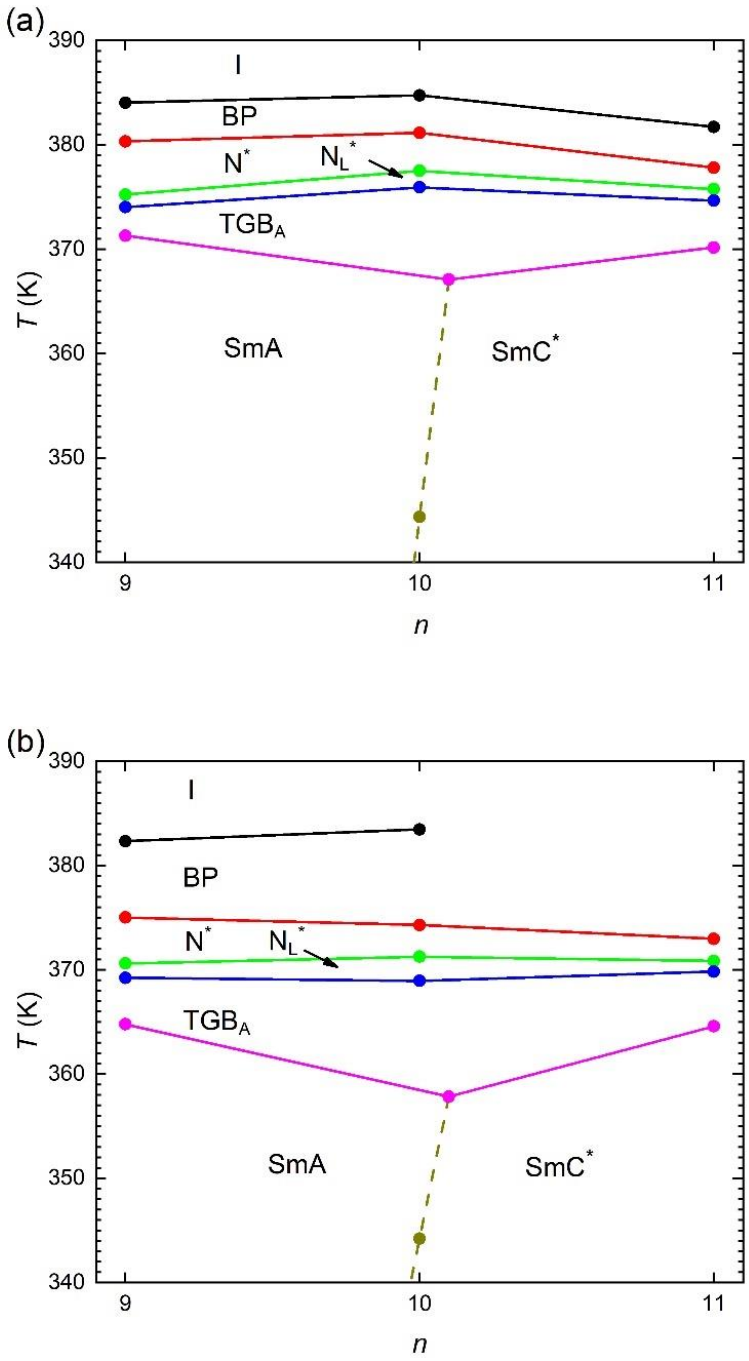

Figure 38: The $n-T$ phase diagrams for a) pure samples ($\chi = 0.0$) and b) for LC-Au NP mixtures with $\chi = 0.01$. The dashed line separating the SmA and SmC* phases can be considered a kind of MPB analogous to the MPB in ferroelectrics.

Chapter 3

Caloric effects

When Indian rubber is rapidly stretched, it warms up. Blind natural philosopher John Gough first observed this phenomenon in the early 19th century by touching the rubber with his lips [126]. If this heat is allowed to dissipate, the rubber cools down upon releasing the uniaxial stress. Similar effects were observed for various materials by Joule in 1859 [127]. Shortly after, Lord Kelvin provided a thermodynamic interpretation of these effects [128], now known as caloric effects. External fields conjugate to specific order parameters cause an entropy change in the energy reservoir subsystem related to the order parameter. In the case of adiabatic conditions, the system as a whole compensates for this subsystem entropic change with a thermal entropy change, i.e., temperature change. A schematic representation of such a process in a dipolar system is given in Figure 39.

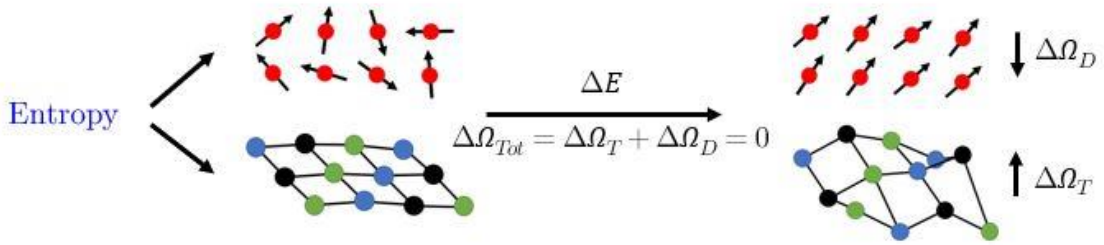

Figure 39: Schematic representation of an entropy exchange between two subsystems, which, under adiabatic conditions, leads to a temperature change in the system.

We shall look at Maxwell's relations to see why this is a possibility. The Maxwell relation based on the Gibbs free energy G is derived as follows. We write down the expression for dG:

$$dG = -\Omega dT + Vdp - \alpha dM, \tag{61}$$

where Ω is the entropy, V is the volume, dT is the temperature change, dp is the change in pressure, α is some other order parameter that describes the system, and dM is the change in a field conjugate to the order parameter α. It is presumed that the system is at constant atmospheric pressure, hence $dp = 0$. We see that G is a function of T and M. Alternatively, one can write Equation (61) as:

$$dG = \left(\frac{\partial G}{\partial T}\right)_M dT + \left(\frac{\partial G}{\partial M}\right)_T dM. \tag{62}$$

Equating both expressions gives:

$$\Omega = -\left(\frac{\partial G}{\partial T}\right)_M, \alpha = -\left(\frac{\partial G}{\partial M}\right)_T. \tag{63}$$

Since G is an exact differential:

$$\left(\frac{\partial^2 G}{\partial T \partial M}\right) = \left(\frac{\partial^2 G}{\partial M \partial T}\right), \tag{64}$$

we have the following Maxwell relation:

$$\left(\frac{\partial \Omega}{\partial M}\right)_T = \left(\frac{\partial \alpha}{\partial T}\right)_M. \tag{65}$$

To further expand this expression, the reciprocity theorem:

$$\left(\frac{\partial x}{\partial y}\right)_z \left(\frac{\partial y}{\partial z}\right)_x \left(\frac{\partial z}{\partial x}\right)_y = -1, \tag{66}$$

as well as the reciprocal theorem is used:

$$\left(\frac{\partial x}{\partial y}\right)_z = \frac{1}{\left(\frac{\partial y}{\partial x}\right)_z}, \tag{67}$$

to rewrite $(\frac{\partial \Omega}{\partial M})_T$ as:

$$\left(\frac{\partial \Omega}{\partial M}\right)_T = -\left(\frac{\partial T}{\partial M}\right)_\Omega \left(\frac{\partial \Omega}{\partial T}\right)_M. \tag{68}$$

Some partial differentials in Maxwell's relations relate to measurable properties, such as heat capacity. Specifically:

$$\left(\frac{\partial \Omega}{\partial T}\right)_M = \frac{C_M}{T}, \tag{69}$$

where C_M is the heat capacity at constant external field M. Combining Equations (62), (68), and (69), the expression for an adiabatic temperature change of a material is:

$$\Delta T(T, M) = -\int_{M_1}^{M_2} \frac{T}{C_M} \left(\frac{\partial \alpha}{\partial T}\right)_M dM. \tag{70}$$

In practice, the usual input data consist of experimental values of $\alpha(T, M)$ and $C_M(T)$. Solving the integral numerically, one can obtain a value for ΔT. The issue becomes if $C_M(T)$ contains singularities. In such a case, the Maxwell approach cannot give us a reliable answer for ΔT. Later on, we will consider an alternative approach based on the separation of the entropy based on the system's entropy subsystems.

All caloric effects fall broadly into at least one of the following categories: magnetocaloric (MCE), electrocaloric (ECE), and mechanocaloric effects, which is further subdivided into elastocaloric (eCE) and barocaloric effects (BCE). A brief overview is given in Table 1.

Table 1: Overview of different caloric effects, the order parameters associated with each effect, and the external fields conjugate to the order parameters.

Caloric effect	Order parameter	Conjugate field
Magnetocaloric effect (MCE)	Magnetization $\vec{M}$	Magnetic field $\vec{H}$
Electrocaloric effect (ECE)	Polarization $\vec{P}$	Electric field $\vec{E}$
Elastocaloric effect (eCE)	Strain ε	Uniaxial stress σ
Barocaloric effect (BCE)	Volume V	Hydrostatic pressure p

Materials exhibiting caloric effects are particularly interesting due to their potential to be implemented in solid-state cooling technologies, making them a more environmentally friendly alternative to the current vapor-compression cooling technologies. However, all of them have their advantages and disadvantages, which must be considered when designing new-generation cooling devices [129]. In this work, we shall mainly focus on the ECE in solid-state solutions of BT and the eCE in MC-LCE.

3.1 Experimental Techniques used in the Study of Caloric Effects

In addition to calorimetric measurements, presented in Section 1.6.1, here we present other measurement techniques used in order to characterize samples, as well as to determine the caloric temperature changes.

3.1.1 Dielectric spectroscopy

Dielectric spectroscopy is used to determine the samples' phase transition region before measuring the ECE. It has been shown that the largest electrocaloric (EC) response in relaxor ferroelectrics is achieved near the phase transition, which takes place on the low-temperature slope of the dielectric peak [123,130–138]. The sample preparation is performed in the same way as for ECE measurements. The frequency dependence of the complex dielectric permittivity $\varepsilon = \varepsilon' - i\varepsilon''$ is measured using an Agilent model E4980A precision LCR meter. The temperature is determined using data from the thermistor resistance, measured by the Keithley digital multimeter. In contrast, the stable bath temperature is provided by the Lakeshore model 340 temperature controller.

3.1.2 Electrocaloric measurements and analysis

For ECE measurements, our home-made high-resolution calorimeter with a few modifications is used.

Ceramic samples (Figure 40) are polished on both sides using high-grit sandpaper to ensure a smooth flat surface and to thin the sample down, if needed. Both smoothed surfaces are now coated with a silver paste, which upon drying will act as our electrodes. Thin gold wires of thickness 50 μm are glued to the silver electrodes using a two-component silver-based conducting adhesive EPO-TEK EJ2312. Finally, a small glass bead 500 kΩ thermistor is glued on the surface using a 2-component adhesive Torr Seal. The sample is then hermetically sealed by two copper blocks in the same way as samples for high-resolution calorimetric measurements.

Figure 40: Example of a ceramic sample. Top row before polishing and bottom row after preparation.

Instead of applying an input power to the sample, the Krohn-Hite model 5920 signal is now connected to a Kepco model BOP 1000M bipolar operational power supply/amplifier, which amplifies the Krohn-Hite signal voltage to assure a sufficiently high applied electric-field. The Keithley 2002 digital multimeter is used for data acquisition of the resistance of the 500 kΩ thermistor, and an external multimeter is used to determine the applied voltage. The Lakeshore model 340 temperature controller is used to stabilize the surrounding bath temperature. The whole measurement process is performed by a computer, with the exception of determining the applied voltage, which must be done manually.

A step-like electrical signal is applied to the sample in a standard ECE measurement. The duration of this signal is long enough for the sample to reach thermal equilibrium with the surrounding bath. Upon applying the signal, the sample temperature rapidly increases to a certain saturated temperature, which begins to decrease back down to the surrounding bath temperature slowly. After a long enough time, the electric signal is removed and the sample temperature rapidly drops to a certain saturated temperature, which slowly increases back to the surrounding bath temperature. In order to determine the temperature change ΔT, the long temperature relaxation tail of the internally thermally equilibrated sample is fitted using the ansatz:

$$T(t) = T_B + \Delta T e^{-\frac{t}{\tau_{ext}}}, \tag{71}$$

where $\tau_{ext} = RC_p$ is the external characteristic thermal relaxation time in which the whole sample exchanges heat with its surrounding. In most cases, some Joule heating is present and is subtracted from the data using the ansatz:

$$T_j(t) = T_B + \Delta T_j \left(1 - e^{-\frac{t}{\tau_{ext}}}\right). \tag{72}$$

The remaining result $T(t) - T_j(t)$ is then fitted by the exponential decay ansatz to determine the actual value of ΔT. Considering the additional parts connected to the sample, which are the silver electrodes, gold wires, and thermistor, we have to additionally correct ΔT by subtracting their contribution to heat absorption during the internal heat equilibration. This gives us the true value:

$$\Delta T_{ECE} = \Delta T \sum_i \frac{C_p^i}{C_p^{sample}}, \tag{73}$$

where $C_p^i = m_i c_p^i$ are the heat capacities of each constituent that make up the sample and C_p^{sample} is the heat capacity of the EC active material. In other words, part of the material that is covered by silver electrodes.

3.1.3 Elastocaloric and thermomechanical measurements and analysis

The main-chain liquid crystalline elastomer (MC-LCE) sample preparation employs the conventional two-step Finkelmann procedure [139]. 1,1,3,3-Tetramethyldisiloxane is used as a chain extender, and 2,4,6,8,10-Pentamethylcyclopentasiloxane as a 5-point crosslinker. The chemical structure of a mesogen is shown in Figure 41 [140]. Toluene was used as a solvent, and a solution of dichloro(1,5-cyclooctadiene)platinum(II) in dichloromethane as a catalyst. The second crosslinking step was carried out in the N phase. Crosslinker density, temperature, applied uniaxial stress during the second crosslinking process, and the concentration of LC mesogens used to swell the sample were varied to obtain samples with different physical and chemical properties.

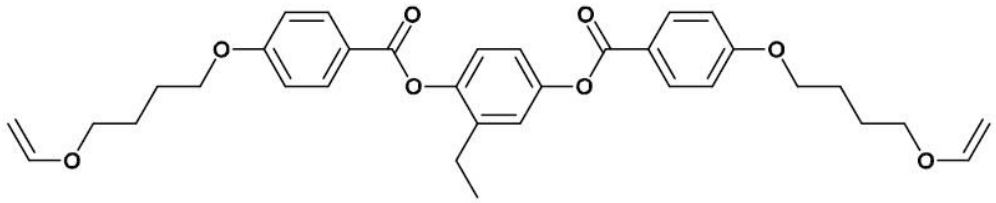

Figure 41: Chemical formula of the LC molecule used in the MC-LCE.

For eCE and thermomechanical measurements, a home-made setup was used, which is able to measure length, strain, and temperature simultaneously.

LCE samples in the form of strips are cut to a length l_0, typically ranging from a few mm to several cm. Strips of Kapton tape are glued on each side of the sample using a two-component adhesive Loctite Hysol 1C. A small glass bead thermistor is attached to the middle of the sample using Neostik Universal contact rubber glue. Gold wires of thickness 50 µm are soldered to the thermistor wires. The sample is then connected to glass holders and inserted into our home-made setup. An image of a prepared sample is given in Figure 42.

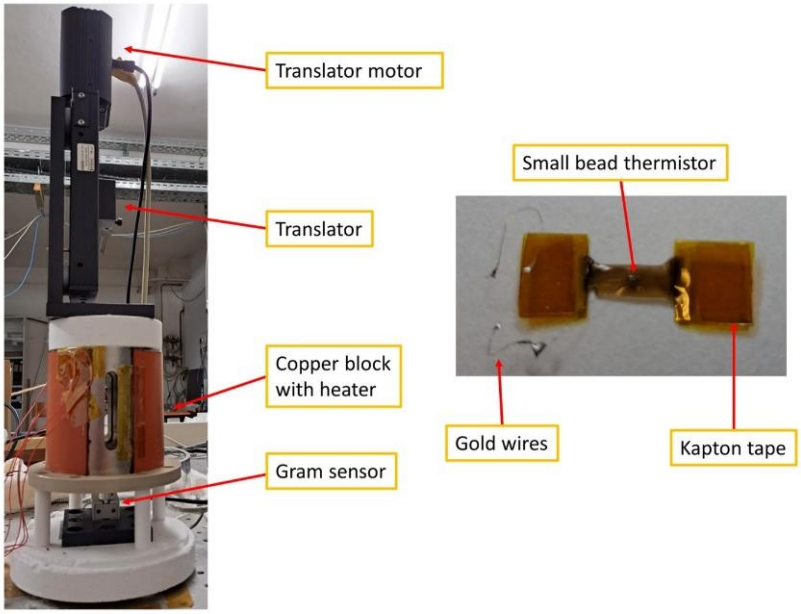

Figure 42: Image of the home-made setup for eCE and thermomechanical measurements and a prepared MC-LCE sample.

The sample is inserted into a copper block with an attached heater. The temperature of the copper block is stabilized with a Lakeshore model 350 temperature controller. On one side, the glass holder is connected to a translator, and on the other side, to a precision gram sensor. The precision gram sensor, capable of measuring compression and tension, is used to measure strain experienced by the LCE samples. The temperature of the sample was determined using data of the thermistor resistance measured by a Keithley 2002 digital multimeter. All the data from the digital multimeter, the precision gram sensor, and the translator are collected by a computer, enabling the control of all the parameters of the experiment.

Thermomechanical measurements are performed by heating the sample within the copper block. During heating, we maintain a small constant tension (a force equivalent to 400 mg) on the sample allowing the translator to move by an appropriate amount as the sample contracts. The translator's motion is dictated by the gram sensor as it detects a change in tension when the sample changes its length. The sample length l is then measured as a function of the sample temperature T.

Each measurement of the eCE is performed by stretching the sample by a finite amount Δl. This stretching is, however, not performed instantaneously but in a sequence of finite-time movements. After receiving the triggering signal from the computer, the translator accelerates with an acceleration of $a = 1$ mm/s^2 until it reaches the half way point of Δl, $l_1 = \frac{\Delta l}{2}$, at $t = t_1$. After that, it immediately starts to decelerate with an acceleration $a =$ -1 mm/s^2 until it reaches $\Delta l = l_1 + l_2$ at time $t = t_1 + t_2$. The whole sequence of movements is given as:

$$\Delta l = \begin{cases} 0, & t < 0 \\ \frac{1}{2}at^2, & 0 \leq t \leq t_1 \\ l_1 + v(t - t_1) - \frac{1}{2}a(t - t_1)^2, & t_1 \leq t \leq t_1 + t_2 \\ l_1 + l_2, & t > t_2 \end{cases}, \tag{74}$$

where $v = at_1$ and $l_2 = v(t_2 - t_1) - \frac{1}{2}a(t_2 - t_1)^2$. This nonuniform translator movement implies a nonuniform stress field. This must be taken into consideration during the data analysis.

Based on the raw data of the elastocaloric (eC) temperature change ΔT_{eCE} as a function of stretching length Δl, one can infer a linear dependence, implying that the heat change ΔQ can be written as:

$$\Delta Q = mc_p \Delta T = K \Delta l. \tag{75}$$

From here on, we use the zero-dimensional analysis model, where we neglect any temperature gradients within the sample due to fast internal thermal relaxation times. The power equation is expressed as:

$$P = C_p^{sys} \frac{dT}{dt} + \frac{T - T_B}{R}. \tag{76}$$

Power P is directly related to the temperature variation of the sample and its heat loss to the bath. Temperatures T and T_B are the measured sample temperature and surrounding bath temperature, R is the thermal resistance of the thermal link between the sample and its surrounding, and C_p^{sys} is the heat capacity of the whole system composed of all subsystems involved. Then, combining Equations (74) and (75), we obtain the eC heat change per time during the translator movement:

$$P = \frac{dQ}{dt} = \begin{cases} 0 & t < 0 \\ \alpha t & 0 \leq t \leq t_1 \\ 2\alpha t_1 - \alpha t & t_1 \leq t \leq t_1 + t_2 \\ 0 & t > t_2 \end{cases}, \tag{77}$$

where $\alpha = Ka$. Rearranging the terms in Equation (76), we obtain the expression for the time evolution of temperature:

$$\frac{dT}{dt} + \frac{T}{C_p^{sys} R} - \left(\frac{P}{C_p^{sys}} + \frac{T_B}{C_p^{sys} R} \right) = \frac{dT}{dt} + \frac{T}{\tau} - \left(\frac{P}{C_p^{sys}} + \frac{T_B}{\tau} \right) = 0, \tag{78}$$

the solution of which is:

$$T = \begin{cases} T_B & t < 0 \\ T_B + C_1 e^{-t/\tau} + \alpha(t - \tau) & 0 \leq t \leq t_1 \\ T_B + C_2 e^{-t/\tau} + \alpha(2t_1 + \tau - t) & t_1 \leq t \leq t_1 + t_2 \\ T_B + C_3 e^{-t/\tau} & t > t_2 \end{cases}, \tag{79}$$

where:

$$C_1 = \alpha \tau, \tag{80}$$

$$C_2 = \frac{C_1 e^{-t_1/\tau} - 2\alpha\tau}{e^{-t_1/\tau}}, \tag{81}$$

$$C_3 = \frac{C_2 e^{-t_2/\tau} + \alpha(2t_1 + \tau - t_2)}{e^{-t_2/\tau}}. \tag{82}$$

Using the above set of functions to fit the experimental data, the amplitude of the temperature change ΔT can be determined. However, the value obtained in this way is smaller than the actual eC temperature change since the heat dissipation occurring due to the attached components on the sample, which are the thermistor, adhesive, gold wires, and Kapton tape, have yet to be considered. Therefore, to take these heat losses into account, additional corrections to ΔT have to be made by subtracting their contribution to heat absorption during the internal heat equilibration:

$$\Delta T_{eCE} = \Delta T \sum_i \frac{C_p^i}{C_p^{sample}}, \tag{83}$$

where $C_p^i = m_i c_p^i$ are the heat capacities of each constituent that make up the sample and C_p^{sample} is the heat capacity of the eC active material.

When eCE measurements are performed on samples with a comparable thickness to the thermistor, an additional correction must be considered. Let us denote r as the radius of the region on the LCE of thickness d, in which the temperature disturbance due to the thermistor is present. Using the heat equation, one can make a straightforward estimate of the radius r:

$$r = \sqrt{\frac{\lambda_s t}{\rho_s c_{p,s}}}, \tag{84}$$

with λ_s, ρ_s, and $c_{p,s}$ denoting the thermal conductivity, density, and specific heat of the sample. The mass of the disturbed region is $m = \rho_s \pi r^2 d$. Inserting the expression for r into the expression for m yields:

$$m(t) = \frac{\pi \lambda_s d}{c_{p,s}} t. \tag{85}$$

The heat fluxes exiting the sample with cross-section S and entering the thermistor are:

$$P_1 = \frac{\lambda_s S}{r} \Delta T_1, \tag{86}$$

$$P_2 = \frac{2\lambda_t S_t}{l_t} \Delta T_2. \tag{87}$$

Here $\Delta T_1 = T_s - T_m$, where T_s is the sample temperature, and T_m is the temperature that is measured by the thermistor, while $\Delta T_2 = T_m - T_B$, where T_B is the temperature of the bath. λ_t, S_t, and l_t refer to the thermal conductivity, cross-section area and length of the thermistor and gold wires. The correction factor is then defined as:

$$k = \frac{T_s - T_0}{T_m - T_0}. \tag{88}$$

Taking into account that $P_1 = P_2$, the following expression for k is obtained:

$$k = 1 + \frac{1}{\pi \lambda_s d R_t}, \tag{89}$$

with R_t denoting the total heat resistance of both the thermistor and gold wires. Typical values of λ_s are in the range of 1-1.5 W/mK, the values for d are between 0.1-0.4 mm, and the values of R_t around 1.8×10^5 K/W. This gives the typical values of k between 1.01 to 1.10.

The external stress field σ, on the other hand, can be determined from the applied force $\mathcal{F}$. The applied stress difference is:

$$\Delta\sigma = \frac{d\mathcal{F}}{dS} = \frac{\Delta(mg)}{S_r \frac{l_r}{l_s}}, \tag{90}$$

where S_r and l_r are the sample cross-section area and sample length at room temperature, and l_s is the sample length at the beginning of the measurement. The measured force is given in the form of weight mg.

3.2 Ferroelectrics

Ferroelectricity is a property of certain materials with a spontaneous electric polarization, which can be reversed by a large enough external electric field. Ferroelectric materials, such as Rochelle salt $NaKC_4H_4O_6 \cdot 4H_2O$ and BT, are composed of crystals where the structural units are tiny electric dipoles: the positive and negative charge centers are slightly separated. When some of these dipoles line up in clusters, they form domains, which can predominantly be oriented by a strong electric field. Reversing the orientation of the electric field reverses the predominant orientation of the ferroelectric domains. This does not happen instantaneously, though, and the reorientation or switching lags behind the change in the electric field. This lag of the electric polarization behind the external electric field is ferroelectric hysteresis. Ferroelectricity ceases to exist above a certain temperature, called the Curie temperature. This is due to heat fluctuations of the dipoles, which is sufficient to overcome the forces that spontaneously align them. They exhibit a wide array of functional properties, such as polarization switching, piezoelectricity, pyroelectricity, and nonlinear optical and dielectric behavior. These properties are crucial for application in capacitors, pyroelectric devices, transducers, sonars, actuators, IR detectors, and microwave phase filters [70].

We shall limit ourselves to ferroelectric materials with a perovskite structure. The perovskite oxides ABO_3, with a relatively simple chemical and crystallographic structure, have contributed most to our understanding of ferroelectric and antiferroelectric phenomena. Figure 43 presents an ideal cubic structure of perovskites, where the A cations are placed in the cube's corners and the B cation at the center, while the X anions are placed at the center of the faces of the cube. The A cations are monovalent or trivalent metal ions and are larger than the B cations, which are trivalent or hexavalent. The X anion is oxygen but can be substituted by fluorine and chlorine ions. In the case of BT, the larger A cation is Ba^{2+}, the smaller B cation is Ti^{4+}, and the X anion is O^{2-} [70,141].

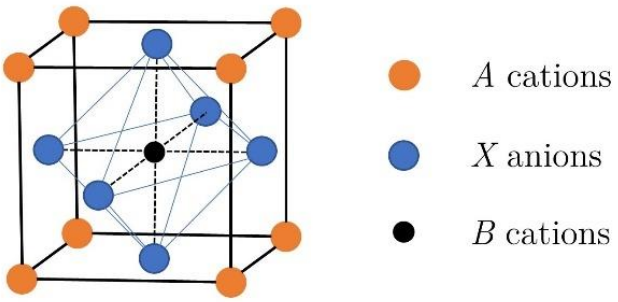

Figure 43: Ideal cubic structure of perovskites with A cations placed in the corners of the cube, X anions in the centers of the faces of the cube, and B cations in the cube's center.

Ferroelectric transitions can be classified into two groups: displacive and order-disorder. The order-disorder type transition, associated with hydrogen-bonded crystals, is caused by the movement of hydrogen protons between two energetically equivalent states that present a potential minimum. At a high enough temperature, known as the Curie temperature T_C, the hydrogen protons have a high enough thermal energy to overcome the potential barrier between the two states, which can now both be occupied with an equal probability. This arbitrary distribution of hydrogen protons represents a disordered system. The consequence is a symmetrical distribution of elongated hydrogen bonds, destroying the spontaneous nonzero polarization. Below the Curie temperature T_C, the transitions between potential minimums are severally reduced due to the insufficient thermal energy of the hydrogen protons. They remain stuck in one of the potential minimums, resulting in an ordered system and a net nonzero polarization [142–145].

Perovskite structured crystals exhibit the displacive type transition. This is where ions are displaced from their original position. The material is in a paraelectric state at high temperatures with a cubic structure and zero net polarization. By cooling it below the Curie temperature T_C, the B cations displace relative to the X anions [146–148]. The direction of this displacement is determined by the competition between short-range interactions (Pauli repulsion) and long-range interactions (Coulomb attraction, dipole-dipole interaction). In this tetragonal structure, the centers of positive and negative charges do not coincide anymore, resulting in an appearance of a spontaneous dipole moment and, thus in polarization. The nature of this particular ferroelectric phase transition can be either first- or second-order, with the first-order transition being associated with a discontinuous change in spontaneous polarization. In contrast, the second-order transition is associated with a continuous change in spontaneous polarization.

3.3 Phenomenological Description of Phase Transitions in Ferroelectrics

The Landau-Ginzburg-Devonshire thermodynamic theory gives a macroscopic description of ferroelectric transitions [149,150]. It considers the expansion of the free energy F in terms of the macroscopic polarization P:

$$F = F_0 + gP + \frac{1}{2}AP^2 + \frac{1}{3}BP^3 + \frac{1}{4}CP^4 + \cdots - EP, \tag{91}$$

where F_0 is the free energy in the paraelectric state, g, A, B, and C are expansion coefficients, and E is an external electric field. In general, g, A, B, and C can be functions of various physical parameters, such as temperature or pressure. In this case, only A is considered to be a function of temperature. We must also note that not all terms in the expansion are allowed due to symmetry considerations. If a crystal is centrosymmetric in the paraelectric phase, which means it has a center of inversion, then odd terms are not allowed. Assuming no external electric field is present, the free energy expansion can be written as:

$$F = F_0 + \frac{1}{2}A(T)P^2 + \frac{1}{4}B'P^4 + \frac{1}{6}C'P^6 + \cdots \tag{92}$$

In the ferroelectric phase, the polarization P is the spontaneous polarization P_S the size of which represents a thermodynamically stable value of F. To estimate P_S, we minimize F in terms of P, which leads to the equation of state:

$$\left(\frac{\partial F}{\partial P}\right)_{P=P_S} = A(T)P_S + B'P_S^3 + C'P_S^5 = 0. \tag{93}$$

Here we only took the first three terms into account. Whether the transition is first- or second-order is determined by the sign of B'.

In the case of a first-order transition, ($B' < 0$), the results are two minima in F when $T \leq T_C$ (Figure 44). The first solution $P_S = 0$ is the trivial solution and corresponds to the paraelectric phase. The nontrivial solution representing the ferroelectric phase is:

$$P_S = \pm\sqrt{\frac{-B' + \sqrt{B'^2 - 4A(T)C'}}{2C'}}, \tag{94}$$

where we assume the expansion coefficient $A(T)$ to be of the form $A_0(T - T^*)$, with T^* being the supercooling temperature. Note that $T^* \neq T_C$. The Curie temperature T_C represents the point where a discontinuous jump in spontaneous polarization occurs due to the onset of the nontrivial minimum in F as a function of P. The Curie-Weiss temperature T^*, which is lower than T_C, represents the point where the trivial solution $P_S = 0$ ceases to be a metastable state.

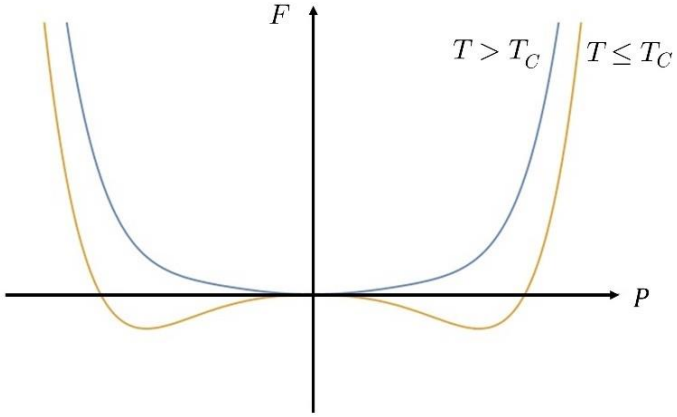

Figure 44: Free energy F as a function of polarization P at two temperatures: $T > T_C$ and $T \leq T_C$. At $T > T_C$, only the paraelectric phase, $P_S = 0$, is stable, while at $T \leq T_C$ the ferroelectric phase represented by the two minima, $P_S \neq 0$ is stable.

In the case of a second-order transition ($B' > 0$), we neglect the higher-order terms, such as $\frac{1}{6}C'P^6$. The spontaneous polarization in the ferroelectric phase is determined from the equation of state:

$$\left(\frac{\partial F}{\partial P}\right)_{P=P_S} = A(T)P_S + B'P_S^3 = 0, \tag{95}$$

which yields:

$$P_S = \pm\sqrt{\frac{-A_0(T-T^*)}{B'}}. \tag{96}$$

We can see that the temperature evolution of F yields only one minimum above T^* at $P_S = 0$ corresponding to the paraelectric phase (Figure 45). Below T^* we have the appearance of two minima represented by the solution of Equation (96) which correspond to the ferroelectric phase.

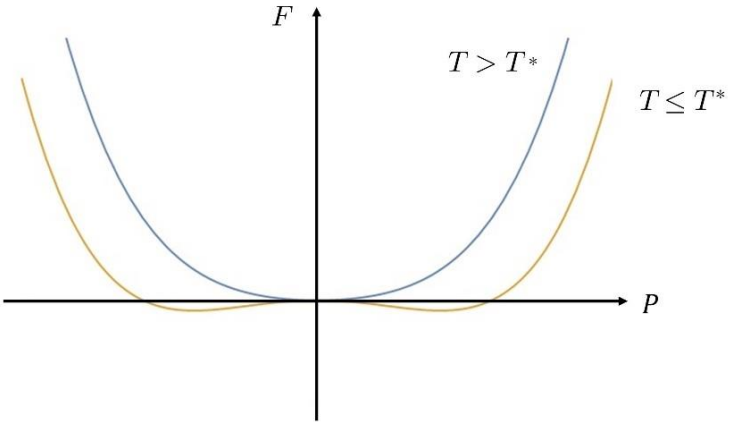

Figure 45: Free energy F as a function of polarization P at two temperatures: $T > T^*$ and $T \leq T^*$. At $T > T^*$, only the paraelectric phase, $P_S = 0$, is stable, while at $T \leq T^*$ the ferroelectric phase represented by the two minima, $P_S \neq 0$, is stable.

3.4 Electrocaloric Effect in Ferroelectrics

The ECE is a physical phenomenon appearing in materials with a dipolar constituency. It requires the coupling between the external electric field and dipolar order parameter, which results in the change of the dipolar order and, thus, the change in the dipolar subsystem entropy. Applying a strong enough external electric field E causes the dipoles to align themselves with E. The dipolar subsystem went from a less ordered to a more ordered state. This causes a decrease in the dipolar subsystem entropy $\Delta\Omega_{dip} < 0$. If this re-ordering happens fast enough, the material does not have enough time to exchange heat with its surrounding, then the process is adiabatic. In such a process, the change in the material's total entropy has to be zero:

$$\Delta\Omega = \Delta\Omega_T + \Delta\Omega_{dip} = 0, \tag{97}$$

where $\Delta\Omega_T$ is the change in the lattice or thermal subsystem entropy. Assuming that $\Delta\Omega_T$ does not depend on the external field, a small thermal entropy change at temperature T is:

$$d\Omega_T = \frac{C_p dT}{T}. \tag{98}$$

Integration leads to the expression:

$$\Delta\Omega_T = \int_{T_1}^{T_2} \frac{C_p dT}{T} = C_p \ln \frac{T_2}{T_1}, \tag{99}$$

where C_p is assumed to be a constant. Generally, this is not true, however, if a small enough temperature interval $[T_1, T_2]$ is taken, one can approximate C_p as being constant. Combining Equations (97) and (99), the expression for the final temperature is:

$$T_2 = T_1 e^{-\frac{\Delta\Omega_{dip}}{C_p}}. \tag{100}$$

To determine $\Delta\Omega_{dip}$, Equation (91) is differentiated with respect to T at a constant E to obtain:

$$\Omega_{dip} = -\left(\frac{\partial F}{\partial T}\right)_E = -\frac{1}{2} A_0 P^2. \tag{101}$$

The change in entropy $\Delta\Omega_{dip}$ is then:

$$\Delta\Omega_{dip} = -\frac{1}{2} A_0 \Big(P^2(T_2, E_2) - P^2(T_1, E_1) \Big), \tag{102}$$

where $P(T_1, E_1)$ and $P(T_2, E_2)$ are determined from the equations of state. Using Equations (100) and (102), the expression for the final temperature is:

$$T_2 = T_1 e^{\frac{A_0 \left(P^2(T_2, E_2) - P^2(T_1, E_1) \right)}{2C_p}}. \tag{103}$$

This self-consistent equation for T_2 can be solved numerically. Thus, the EC temperature change is $\Delta T_{ECE} = T_2 - T_1$.

The search for high-efficiency, low-cost, and environmentally friendly alternatives to vapor cooling systems has generated a growing interest in EC materials. Ever since Mischenko et al. [151] reported a giant EC temperature change $\Delta T_{ECE} = 12$ K in $Pb(Zr_{0.95}Ti_{0.05})O_3$ ferroelectric thin film, research into the ECE in ferroelectrics drastically increased [152–155]. The ECE has been reported in various ferroelectric thin and thick films, polymers, single crystals and bulk ceramics [133,151,152,156]. To date, conventional lead-based ferroelectric materials have produced the best results [151,157–159]. Nevertheless, these lead-based materials suffer from environmental concerns. Over the years, various lead-free refrigeration materials have been investigated, such as BT, $SrTiO_3$, and $Na_{0.5}Bi_{0.5}TiO_3$ [152,160–162].

BT-based compounds have been extensively studied as an environmentally friendly material with excellent dielectric, ferroelectric and piezoelectric properties [163–165]. It is well known that a large EC response usually occurs in the vicinity of the ferroelectric to paraelectric phase transition [138]. Thus, to be able to use BT as an EC material, one must shift the Curie temperature ($T_C = 395$ K) to lower values. This can be done by appropriately doping the *A*- and *B*-sites of the BT lattice, which may also simultaneously enhance the ECE [166–170].

3.5 Doping of Barium Titanate

Extensive studies have been performed on doping of the *A*-site [171–173], *B*-site [174–176], or both [177,178] to tune the physical properties of BT. Adding even a minuscule amount of an appropriate dopant can dramatically affect its electrical properties.

When doping BT, consideration has to be taken whether the M dopant, substituting Ba^{2+} ($MTiO_3$) or Ti^{4+} ($BaMO_3$), can form a stable perovskite structure. This is generally the case with isovalent substitution on either *A* or *B* site of the perovskite structure and can be predicted based on the Goldschmidt tolerance factor and the octahedral factor [179]. On the other hand, if the M dopant does not form a stable perovskite structure, then there is a maximum amount of M that can be introduced into BT. The resulting compound constitutes an M-doped BT.

The process of introducing a dopant with a different valence than that of the ion it is substituting is known as substitutional aliovalent doping. For example, the most common dopants for *A* site substitution in BT are either monovalent (K^+, Na^+, Li^+), trivalent (La^{3+}, Nd^{3+}), or tetravalent (Ge^{4+}), while for *B* site substitution, they are either divalent (Ni^{2+}, Cu^{2+}, Fe^{2+}), trivalent (Ce^{3+}, Gd^{3+}, Ga^{3+}, Fe^{3+}, Al^{3+}, Mn^{3+}), or pentavalent (Nb^{5+}).

Doping ferroelectrics with donors "soften" them. These "softened" ferroelectrics are characterized by higher domain wall mobility. This can be attributed to a relieved internal stress caused by Ba^{2+} or Ti^{4+} vacancies and the transfer of electrons between these ionized vacancies [124,180–182]. However, the primary charge compensation mechanism in donor-doped ferroelectrics remains an open question [183].

Doping ferroelectrics with acceptors "hardens" them [124]. Acceptors hinder the movement of domain walls. This is mainly attributed to volume and surface effects. The stabilization of the domain structure is due to oxygen vacancies that accompany acceptor doping through the formation of defect dipoles [184]. These dipoles act as an internal bias field that pins the domains [176,185,186]. In thermodynamic equilibrium, the symmetry of the defect dipoles conforms to that of the surrounding crystal. This is due to the symmetry-conforming principle of point defects [187,188]. With oxygen vacancies hopping between neighboring positions next to dopants, defect dipoles can achieve reorientation [189,190]. Therefore, it is postulated that the oxygen vacancies move to the domain walls [185,191,192]. The observance of aging in Mn-doped BT single-domain crystal strongly supports the volume effect as the main hardening mechanism in ferroelectric [193].

Domain wall motion is a major contribution to the dielectric properties of ferroelectrics. One can significantly improve the dielectric response by enhancing the 180° domain wall mobility in tetragonal BT without introducing large dielectric losses mostly caused by 90° domain wall mobility and electronic conduction [172,194]. As mentioned, when doping BT with donors, *A*-site vacancies, *B*-site vacancies, and/or electrons are induced for charge balancing. This softening mechanism of donor doping increases the permittivity. For example, *A*-site doping with Nb^{3+} achieves a relative permittivity of 11800 and 36000 for *A*-site La^{3+}-Zr^{4+} co-doping as compared to 4500-10000 in pure BT [195–198]. On the other hand, the induced electrons from donor doping increase the conduction and thus increase dielectric losses [172,173]. In acceptor-doped BT, positively charged oxygen vacancies are induced for charge compensation [190,193,199,200]. Their existence decreases domain wall mobility, contributing to a decrease in permittivity [193]. As a result, relative permittivity decreases to 1800 or 1000 with an increase of Fe^{3+} or Mn^{3+} up to 1 at% on *B*-sites, respectively [201]. This is also true when introducing Zn^{2+} on *B*-sites, where the permittivity reduces by nearly 1000 [202]. Moreover, oxygen vacancies may contribute to conductivity, thereby increasing dielectric losses [203].

In addition to affecting permittivity, doping can also change phase transition temperatures. BT is paraelectric with a centrosymmetric cubic symmetry above the Curie temperature. Cooling it below T_C, it undergoes a series of transitions: first to a tetragonal phase at $T_C = 395$ K, then to an orthorhombic phase at $T_{T-O} = 280$ K, and finally to a rhombohedral phase at $T_{O-R} = 185$ K [124,204,205]. Because dopants have an ionic radius different from the one of the host ions, the oxygen octahedron surrounding a dopant is distorted, which leads to a different phase transition temperature. When smaller ions substitute Ba^{2+}, the surrounding oxygen ions displace towards the dopant, resulting in more open space and enabling larger displacements of Ti^{4+} [206]. As a consequence, the tetragonal phase is destabilized and T_C decreases. Ce^{3+} doped BT with a concentration of 3 at% decreases T_C to 313 K, and in A-site La^{3+} doped BT T_C decreases while T_{T-O} increases with increasing concentration up to 6 at%, leading to a narrower existence temperature range of the tetragonal phase [207,208]. Replacing Ti^{4+} ions with ions of different radii distorts the surrounding oxygen octahedron. A tetragonal phase destabilizes when larger ions push the oxygen ions towards the neighboring octahedra, reducing the space for the displacement of Ti^{4+} ions. Consequently T_C is shifted to lower temperatures, as well as T_{T-O} might be shifted as well [206]. Similar effects are observed when smaller ions replace Ti^{4+} ions [209].

3.6 Measurement Results of the Electrocaloric Effect in Doped Barium Titanate

In this section, the results of the dielectric and ECE measurements of $B_{0.8}Ca_{0.2}TiO_3$ (BCT), $B_{0.8}Ca_{0.2}Zr_{0.02}Ti_{0.98}O_3$ (BCZT), $Ba_{0.9}Sr_{0.1}TiO_3$ (BSTS-0), $Ba_{0.9}Sr_{0.1}Ti_{0.95}Sn_{0.05}O_3$ (BSTS-5), and $Ba_{0.9}Sr_{0.1}Ti_{0.9}Sn_{0.1}O_3$ (BSTS-10) are presented. These polycrystalline ceramics were synthesized via the conventional solid-state reaction method by researchers from the IMED-Lab, Cadi-Ayyas University in Marrakech, Morocco [170,210].

3.6.1 Electrocaloric effect in BCT and BCZT

Temperature dependence of the dielectric constant ε' at a frequency of 1 kHz for BCT and BCZT is shown in Figure 46. These measurements show that the ferroelectric to paraelectric phase transition temperature is around $T_C = 389$ K for both BCT and BCZT. The largest ECE response is expected to appear at the low-temperature slope of the ε', which in this case is in the range from around 375 K to approximately 390 K.

The directly measured EC temperature changes under various electric fields in the vicinity of T_C for BCT and BCZT are presented in Figures 47 and 48 [210]. In both samples, the largest temperature changes ΔT_{ECE} are achieved in the vicinity of T_C, at $T = 385$ K. The maximum temperature changes were $\Delta T_{ECE} = 0.474$ K and $\Delta T_{ECE} = 0.668$ K at an applied electric field of $E = 14$ kV/cm for BCT and BCZT, respectively. In comparison, the indirect measurements have shown a temperature change $\Delta T_{ECE} = 0.37$ K and $\Delta T_{ECE} = 0.68$ K at an applied field of $E = 24$ kV/cm [210]. It is quite clear that the indirect measurements understate the size of the EC response.

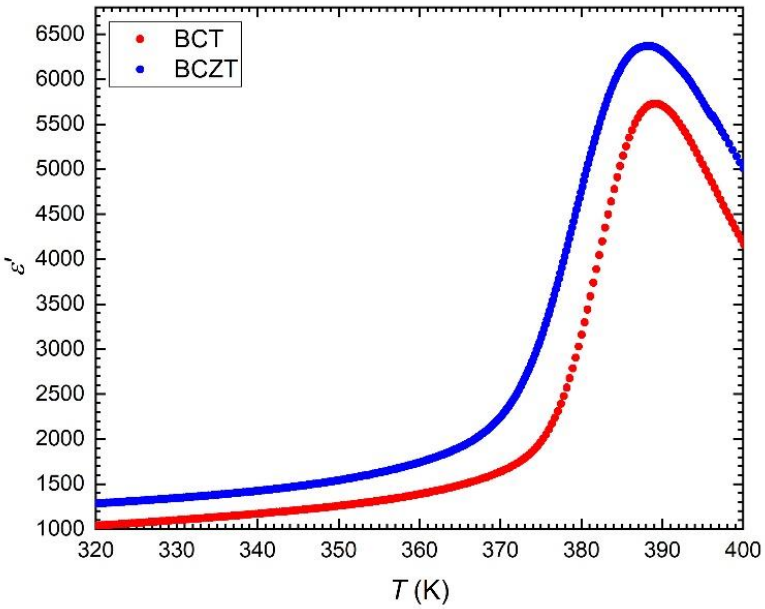

Figure 46: Measurement results of the dielectric constant ε' as a function of temperature T at a frequency of 1 kHz for BCT and BCZT.

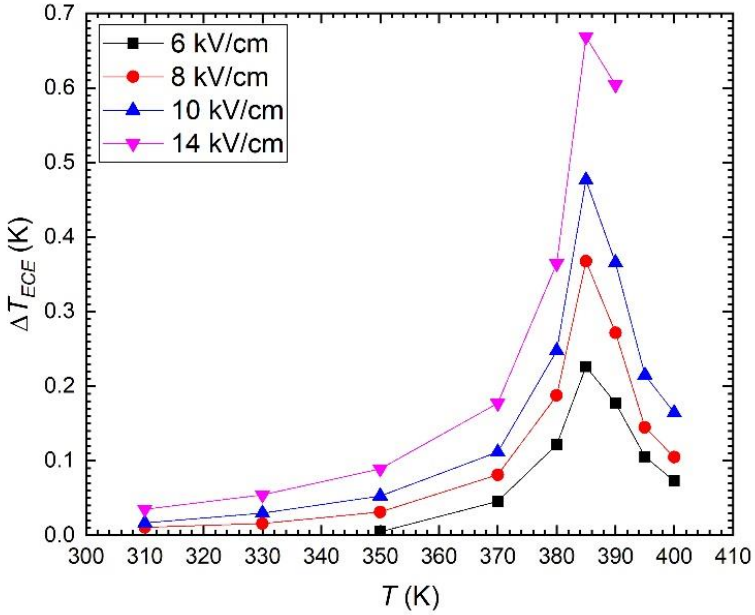

Figure 47: Measurement results of ECE for BCT as a function of temperature T for various electric fields E [210].

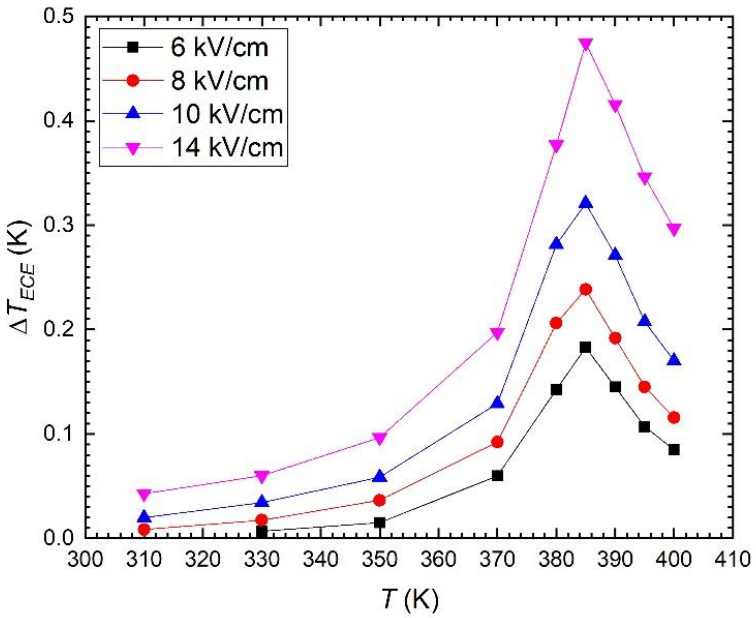

Figure 48: Measurement results of ECE for BCZT as a function of temperature T for various electric fields E [210].

Introducing 2% of Zr^{4+} into the BCT lattice enhances the EC properties of the BCT ceramic. At an applied electric field of $E = 8$ kV/cm, the values of ΔT_{ECE} obtained are 0.23 K and 0.36 K for BCT and BCZT ceramics, respectively. These are the highest when compared to those reported in the literature. Kaddoussi et al. measured a temperature change ΔT_{ECE} of 0.25 K around 360 K at an external field $E = 8$ kV/cm in $Ba_{0.95}Ca_{0.05}Zr_{0.1}Ti_{0.9}O_3$ [211]. Hanani et al. reported an EC response of $\Delta T_{ECE} = 0.492$ K at 360 K under an applied electric field $E = 17$ kV/cm in rod-like $Ba_{0.85}Ca_{0.15}Zr_{0.10}Ti_{0.90}O_3$ ceramic synthesized via surfactant-assisted solvothermal technique [212]. Sanlialp et al. reported that BZT-32BCT ceramics exhibit a maximum temperature change ΔT_{ECE} of 0.33 K at 337 K under an applied external field of $E = 20$ kV/cm [213]. While it is true that introducing 2% of Zr^{4+} into the BCT lattice did enhance the EC response, the temperature at which these relatively large temperature changes occur is still rather high, at $T = 385$ K.

3.6.2 Electrocaloric effect in BSTS-0, BSTS-5, and BSTS-10

Temperature dependence of the dielectric constant ε' at a frequency of 1 kHz for BSTS-0, BSTS-5, and BSTS-10 is shown in Figures 49. The ferroelectric to paraelectric phase transition temperatures T_C are at around 367 K for BSTS-0, 334 K for BSTS-5, and 298 K for BSTS-10.

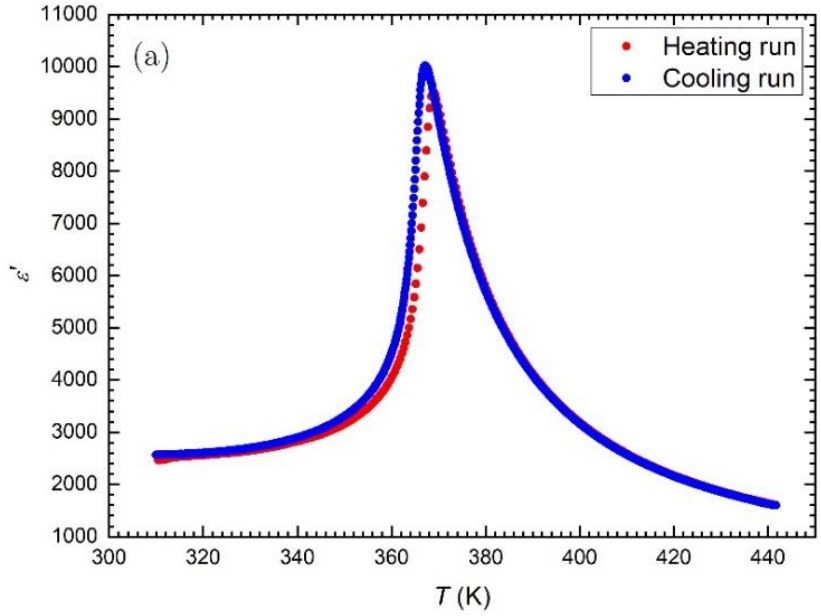
(a)
Heating run
Cooling run
ε'
T (K)

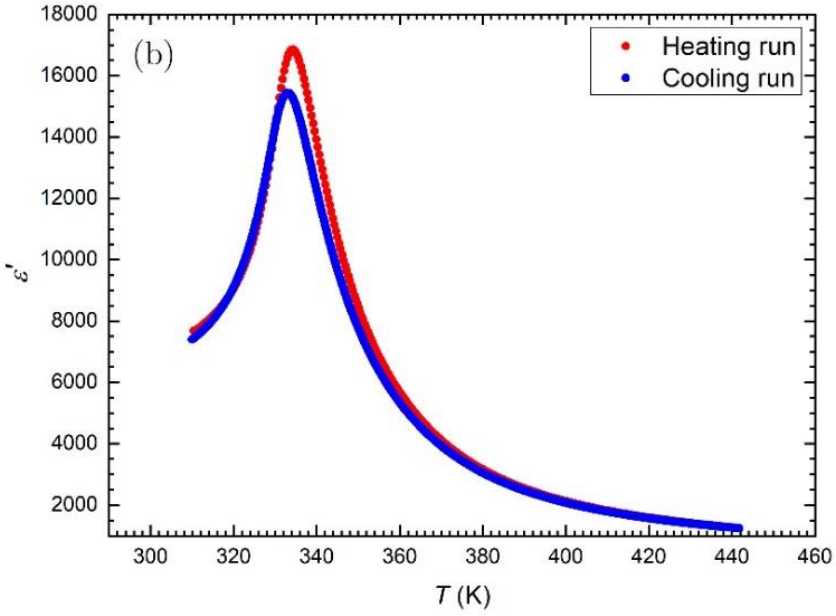
(b)
Heating run
Cooling run
ε'
T (K)

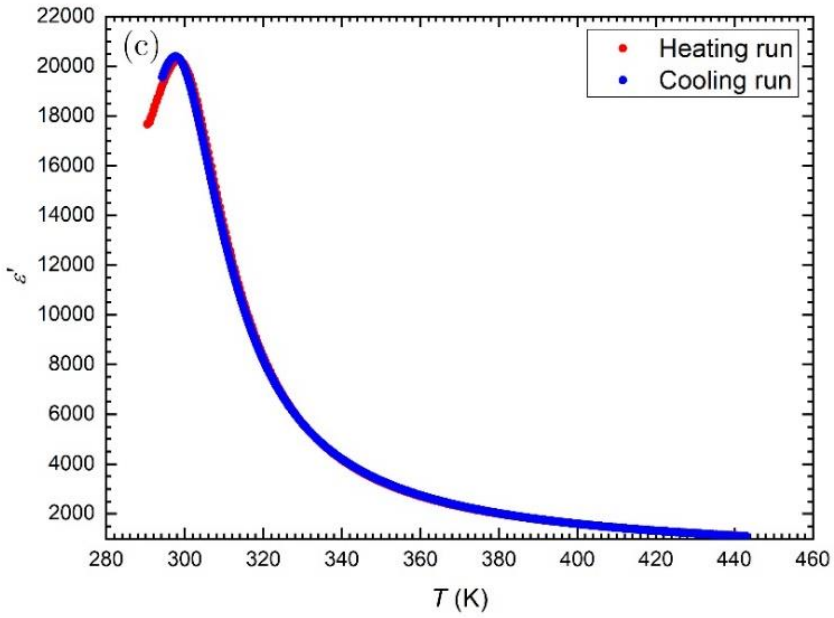

Figure 49: Dielectric spectroscopy results of the dielectric constant ε' as a function of temperature T at a frequency of 1 kHz for a) BSTS-0, b) BSTS-5, and c) BSTS-10.

The directly measured EC temperature changes under various electric fields in the vicinity of T_C for BSTS-0, BSTS-5, and BSTS-10 are presented in Figure 50 [214]. The largest temperature changes occur in the vicinity of T_C in all three samples. In all three samples the peak of the temperature change ΔT_{ECE} shifts a bit to higher temperatures with an increasing applied electric field E. The undoped sample BSTS-0 shows the largest temperature change $\Delta T_{ECE} = 0.52$ K at an applied electric field $E = 7.4$ kV/cm, while the doped samples BSTS-5 and BSTS-10 show a temperature change $\Delta T_{ECE} = 0.45$ K and $\Delta T_{ECE} = 0.19$ K at applied electric fields $E = 16.0$ kV/cm and $E = 8.5$ kV/cm, respectively. On the other hand, the doped samples show a broader peak in the vicinity of the phase transition temperature, which is consistent with the diffuse phase transition behavior of BSTS ceramics [70,215].

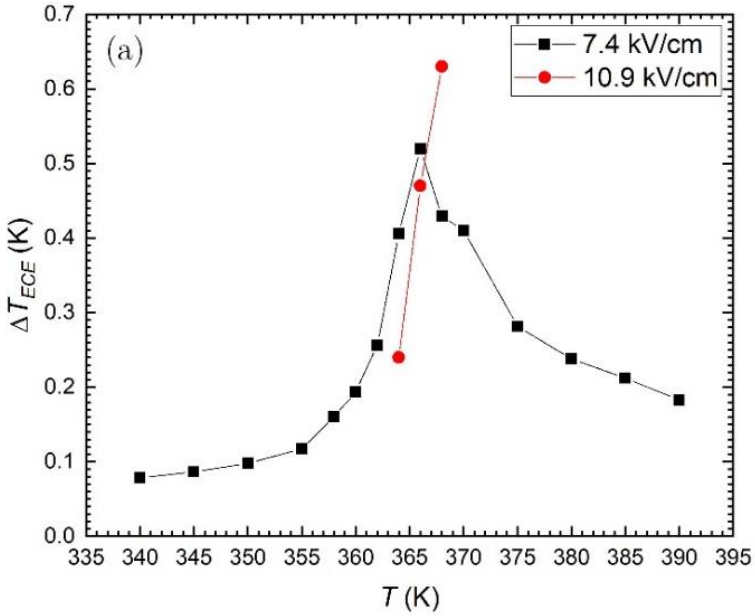
(a)
7.4 kV/cm
10.9 kV/cm
ΔT_{ECE} (K)
T (K)

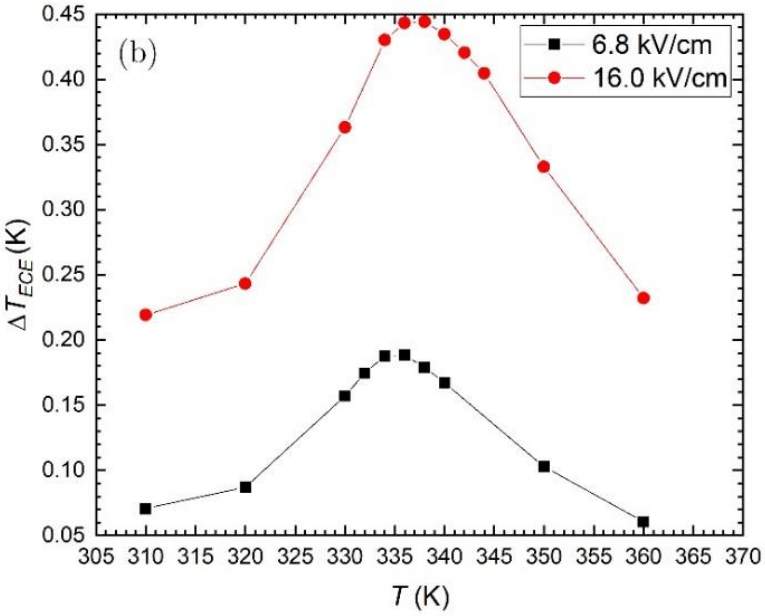
(b)
6.8 kV/cm
16.0 kV/cm
ΔT_{ECE} (K)
T (K)

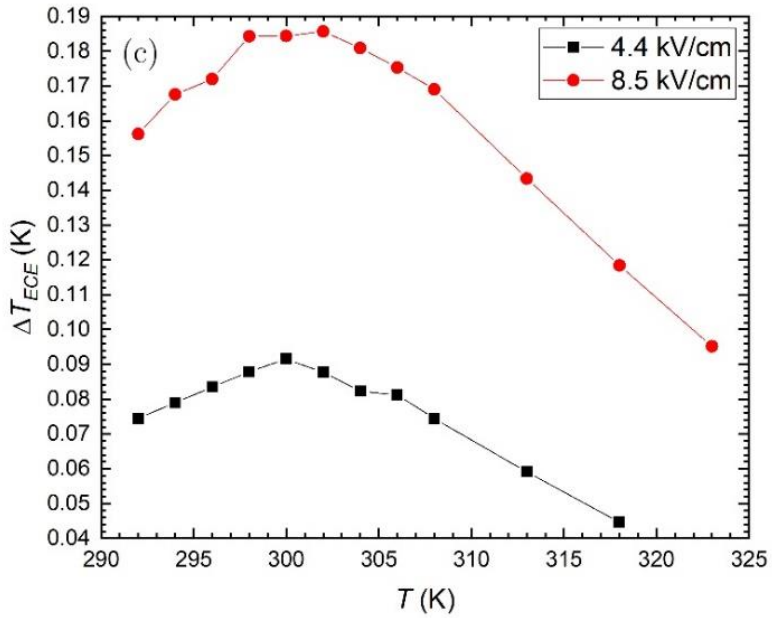

Figure 50: ECE measurement results ΔT_{ECE} as a function of temperature T for various values of the applied electric field for a) BSTS-0, b) BSTS-5, and c) BSTS-10 [214].

To compare the ECE of different materials, the EC responsivity, $\xi = \Delta T_{ECE}/\Delta E$, is chosen as a suitable parameter since it is independent of the dimensions and shape of the samples. A high EC response at a low applied electric field gives an EC responsivity of $\xi =$ 0.70 K mm/kV in the BSTS-0 sample. An increase in the concentration of Sn leads to a decrease in the EC response and a broader peak. The EC responsivity for BSTS-5 and BSTS-10 are $\xi = 0.29$ K mm/kV and $\xi = 0.22$ K mm/kV, respectively. In Table 2, we compare various lead-free ferroelectrics. The BSTS samples display one of the highest EC responsivity compared to lead-free ferroelectrics and lead-based ferroelectrics.

Table 2: Comparison of EC characteristics of BSTS ceramics with other typical ferroelectric materials. These values were obtained using the direct method of determining the EC response.

Material	T_C (K)	ΔT_{ECE} (K)	E (kV/cm)	ξ (K mm/kV)	Ref.
$Ba_{0.90}Sr_{0.10}TiO_3$	366	0.522	7.4	0.70	[214]
$Ba_{0.90}Sr_{0.10}Ti_{0.95}Sn_{0.05}O_3$	338	0.463	16.0	0.29	[214]
$Ba_{0.90}Sr_{0.10}Ti_{0.90}Sn_{0.10}O_3$	302	0.190	8.5	0.22	[214]
$BaTi_{0.89}Sn_{0.11}O_3$	317	0.63	20	0.31	[168]
$Ba_{0.85}Sr_{0.15}Sn_{0.05}Ti_{0.95}O_3$	320	1.44	30	0.48	[169]
$Ba_{0.82}Sr_{0.18}Sn_{0.065}Ti_{0.935}O_3$	304	0.49	20	0.25	[216]
$BaTiO_3$ (single-crystal)	402	0.9	12	0.75	[152]
$PbMg_{1/3}Nb_{2/3}O_3$	340	2.5	90	0.27	[136]

3.7 Liquid Crystalline Elastomers (LCEs)

LCEs are materials in which LC molecules are incorporated into a crosslinked polymer matrix. Depending on the type of incorporation, we differentiate between two types of LCEs: main-chain (MC-LCEs) and side-chain (SC-LCEs) LCEs. As the name suggests, MC-LCEs have LC molecules incorporated directly into the polymer backbone. SC-LCEs, on the other hand, have LC molecules attached laterally to the polymer backbone. LCEs combine the elastic properties of elastomers with the orientational and positional ordering of LC. The coupling between the orientational order and elasticity of elastomers is responsible for some peculiar properties with respect to isotropic rubbers. Cooling down the material from I to N is expressed in the elongation of the material in the direction of the nematic director. The shape change is driven by changes in the director field. These mechanical changes can be influenced by electrical, magnetic, thermal, and optical excitations [65,217–219]. This gives them great potential for applicational purposes as sensors and actuators [61–68,220,221].

Polymers are long chains of segments called monomers. The number of segments composing a polymer chain may be large ($N = 10^2$ - 10^4). The rubbery response of networks depends on the separation of scales between the effective step length l, the distance over which a chain can essentially bend, and the total length of a chain L. In the case of $L \ll l$, this corresponds to an almost completely rigid rod molecule of length L. We shall be focusing on sufficiently long chains, where the entropic nature of polymers is more pronounced. Polymers can be considered entropic springs, since extending the polymer chain drastically reduces the number of possible configurations or chain conformations. After freeing the chain from these constraints, it will relax to a configuration that maximizes the entropy or alternatively, decreases the system's free energy. One must note, however, that polymers are liquids. This is where using crosslinkers to create a rubbery network comes into play.

Binding polymers together via crosslinkers fixes their topology and creates an elastic solid – an elastomer. In such a network, monomers remain highly mobile and thus liquid-like. Due to thermal fluctuations the chains move as rapidly as in a polymer melt, but only as far as their topological constraint will allow them. Due to the entropic nature of polymers, elastomers recover their original shape when an external influence is removed. Such systems, where constraints limit fluctuations, are known as 'quenched' in statistical mechanics. Rigidity and shape memory stem directly from this [60].

As previously mentioned, two strategies for incorporating LC molecules into a polymer chain exist. They can be linked together head-to-tail to form a main-chain polymer. The linkage must be chosen in such a fashion as to ensure sufficient flexibility of the chains. Otherwise, they can be pendant to a flexible polymer backbone. They form side-chain polymers with a topology of a comb [222]. Again, the linkage to the backbone must be chosen carefully to allow the chain conformation freedom while not over-diluting or over-constraining the N phase [223]. Methods of crosslinking polymers into an elastomer varied from chemical, using copolymerization with a small group of reactive groups on a chain and adding bi- or tri-functional crosslinking agents, to radiation processes using UV light with photoinitiators or gamma-radiation [139,224–226]. Without any special attention during the crosslinking process, LCEs always form polydomain textures. Director variation is imprinted by crosslinking; thus, the polydomain state is thermodynamically stable, which is very difficult to eliminate. Over the years, many attempts at aligning polydomain nematic elastomers with electric and magnetic fields were made. These methods were successful only in cases where swelling elastomers with a nematic solvent of molecules similar to those incorporated in the elastomer [227–229]. This showed that the rubbery network presents too much resistance to the electric and magnetic fields. The next logical choice was using stress fields to achieve alignment. Küpfer and Finkelmann developed a two-step crosslinking procedure to produce well-aligned monodomain elastomers [139]. In the first step, nematic polymers are lightly crosslinked to form a weak gel. This gel is then stretched in a uniaxial fashion in either the I or N phase. This achieves an alignment of the incorporated LC. Keeping the gel stretched, a second crosslinking is initiated which fixes the enforced uniaxial alignment. If a large enough stress is applied during the second crosslinking, the final elastomer will be a nematic monodomain below the transition temperature. It can be noted that a nematic monodomain elastomer is optically transparent, while a polydomain sample is optically opaque, unless it is stretched.

In a nematic monodomain elastomer, its macroscopic shape is directly determined by the nematic order of the system. Since one can change the nematic order with temperature, and thus the macroscopic shape, what is observed is known as a thermomechanical response. When an MC-LCE is heated from the N or SmA phase to the I phase, it will contract along the direction of the nematic director. This process is reversible. The elastomer will elongate along the direction of the nematic director once it is cooled from the I to the N or SmA phase. Large extensions are only possible due to the memory effect of imprinting a large stress field into the elastomer during the second crosslinking process [230]. The thermomechanical profile depends on the nature of the phase transition. If the phase transition is a first-order phase transition, the profile is a fast 'on-off' profile. If the phase transition is second-order, the profile is a slow, continuous change (Figure 51) [231].

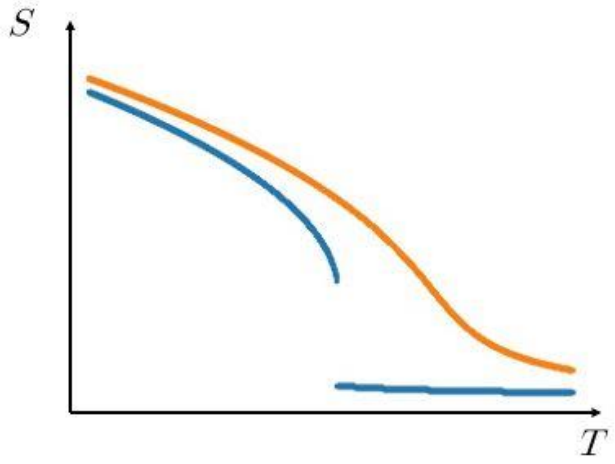

Figure 51: Typical temperature profiles of the order parameter S, similar to the thermomechanical response's temperature profiles. The blue line represents a fast on-off response corresponding to a first-order transition, while the orange lines represent a slow continuous response corresponding to a second-order transition.

The initial impression was that the MC-LCE created by the Finkelmann two-step crosslinking process are supercritical systems with low heterogeneity (low quenched disorder), where the phase evolution is gradual, and the order parameter changes continuously with temperature [231]. Therefore, it was thought that to drive the transition towards the critical regime, where the order parameter exhibits a jump, one had to dope the elastomers with a large enough amount of conventional N LC [232,233]. It turned out that the nature of the thermomechanical response could be determined during the Finkelmann process. Varying the crosslinker concentration, the internal stress during the crosslinking process, and the swelling of the samples affect the profile and magnitude of the thermomechanical response [53,234–236].

3.8 Elastocaloric Effect in Liquid Crystalline Elastomers

As already stated, the eCE is an adiabatic temperature change of a sample when an external uniaxial stress is applied to it. LCEs also exhibit a thermomechanical response, where the sample experiences internal stress and extends or contracts with a temperature variation. Since the order parameter and average chain conformations are coupled, one could logically ask whether applying an external uniaxial stress field to the sample generates a temperature change in the sample. The external uniaxial stress field will extend the polymer chains along a single direction. This, in effect, will also cause the LC molecules attached to the polymer chains to re-orientate and align along the stretching direction. This implies a drop in the LC subsystem entropy $\Delta\Omega_{LC}$. The process is adiabatic if this process happens fast enough so that the sample does not have enough time to exchange heat with its surrounding. In such a case, the total entropy of the system must not change:

$$\Delta\Omega = \Delta\Omega_T + \Delta\Omega_{LC} = 0, \tag{104}$$

where $\Delta\Omega_T$ is the change in the thermal subsystem entropy. Assuming that $\Delta\Omega_T$ does not depend on the external field, a small thermal entropy change at temperature T is:

$$d\Omega_T = \frac{C_p dT}{T}. \tag{105}$$

Integration leads to the expression:

$$\Delta\Omega_T = \int_{T_1}^{T_2} \frac{C_p dT}{T} = C_p \ln\frac{T_2}{T_1}, \tag{106}$$

where C_p is assumed to be constant. Generally, this is not true, however, if one takes a small enough temperature interval $[T_1, T_2]$ one can approximate C_p as being constant. Combining Equations (104) and (106), the expression for the final temperature is:

$$T_2 = T_1 e^{-\frac{\Delta\Omega_{LC}}{C_p}}. \tag{107}$$

In order to determine $\Delta\Omega_{LC}$, the Landau-de Gennes free energy density expression for an N LC is used (Equation (5)) with an additional term expressing the coupling between the S and an applied external uniaxial stress σ:

$$f = \frac{1}{2}a_0(T - T^*)S^2 - \frac{1}{3}bS^3 + \frac{1}{4}cS^4 - \sigma S. \tag{108}$$

Taking the negative derivative of $F = \int f \,\mathrm{d}V$ with respect to T at constant σ, gives:

$$\Omega_{LC} = -\left(\frac{\partial F}{\partial T}\right)_\sigma = -\frac{1}{2}A_0 S^2, \tag{109}$$

$$\Delta\Omega_{LC} = -\frac{1}{2}A_0\Big(S_2^2(T_2, \sigma_2) - S_1^2(T_1, \sigma_1)\Big). \tag{110}$$

Using Equations (107) and (110), the expression for the final temperature is:

$$T_2 = T_1 e^{\frac{A_0\left(S_2^2(T_2,\sigma_2) - S_1^2(T_1,\sigma_1)\right)}{2C_p}}. \tag{111}$$

This self-consistent equation for T_2 can be solved numerically. The values for S_1 and S_2 are obtained from the condition:

$$\left(\frac{\partial f}{\partial S}\right)_T = a_0(T - T^*)S - bS^2 + cS^3 - \sigma = 0. \tag{112}$$

Thus, the eC temperature change is $\Delta T_{eCE} = T_2 - T_1$.

3.9 Simulation and Measurement Results of the Elastocaloric Effect in Main-Chain Liquid Crystalline Elastomers

This section presents the simulation results of the thermomechanical and eC response in MC-LCE. The impact of various parameters in the free energy expression on the thermomechanical and eC response was studied. The measurement results of MC-LCE with varying crosslinker concentrations, internal stress and temperature during the second crosslinking process, and swelling with an LC solvent are presented.

3.9.1 Simulation results of main-chain liquid crystalline elastomers

Firstly, a predictive study of MC-LCE is performed via computer simulations. This is done in order to know what can be expected from the experimental measurements. Equation (108) is used but with an additional term introduced by Petridis and Terentjev [237]. They demonstrated that the presence of network crosslinkers as the source of quenched orientational disorder involves adding an additional term to the Landau free energy expression:

$$f = \frac{1}{2}a_0(T - T^*)S^2 - \frac{1}{3}bS^3 + \frac{1}{4}cS^4 + \frac{d_0}{4S^4} - \sigma S, \tag{113}$$

with the constant d_0 defined as:

$$d_0 = \frac{3\gamma}{2\pi^2(\kappa\beta a^2)^3}k_B T, \tag{114}$$

where $\kappa \sim k_b T/a$ is the Frank elastic constant in the one constant approximation, a is the nematic coherence length, $\beta = 1/k_b T$, and γ is the coupling constant between the order parameter S and the strength of disorder. An increase in crosslinker concentration can be thought of as increasing the disorder strength or in other words, increasing the value of the coupling constant γ. For simplicity, a dimensionless form of this expression is used, namely:

$$\tilde{f} = \frac{81c^3}{4b^4}f = rs^2 - 2s^3 + s^4 + \frac{d}{s^4} - hs, \tag{115}$$

with s, r, d, and h being the dimensionless order parameter, temperature, disorder strength, and uniaxial stress, respectively. To determine the thermomechanical and eC response, the value s for various values of r, d, and h must be calculated. This involves solving the expression $d\tilde{F}/ds|_{r,d,h\,=\,\text{const.}} = 0$. Due to the form of Equation (115), this has to be performed numerically. We present two types of results: one where the value of d is held at a constant value and the other where the value of h is held at a constant value. This will provide information on how the disorder and the stress terms affect the system individually.

From Equations (70) and (113) one can observe that the temperature change ΔT is proportional to $(\partial S/\partial T)_\sigma$. From experiments [238,239], we know that the order parameter S and relative length l/l_0 of monodomain MC-LCE closely follow one another. Thus, if the qualitative behavior of the order parameter as a function of temperature is known, the qualitative behavior of contraction and elongation of the MC-LCE as a function of temperature will also be known. Figure 52 presents the plot of the order parameter s as

a function of temperature r [240]. In both cases, when the values of h and d are increased, the discontinuous jump in s, associated with a first-order phase transition, decreases until it eventually ceases to exist above a certain critical value. The system transitions from a subcritical to a critical and to a supercritical regime. With the presence of uniaxial stress, the system is introduced to an additional ordering force. This means that the system needs to be introduced to much more thermal energy to nullify the effects of the ordering stress completely. Hence the system remains in a paranematic (PN) state at high temperatures, as can be seen by the fact that the order parameter s never quite reaches the value $s = 0$. Similarly, in the case of the disorder strength, the crosslinkers locally provide an easy anisotropy axis, along which it is favorable for the local nematic director to align itself due to steric and long-range van der Waals forces. At high enough disorder strengths, the nematic director is aligned along the local anisotropy axis, giving a residual order parameter s.

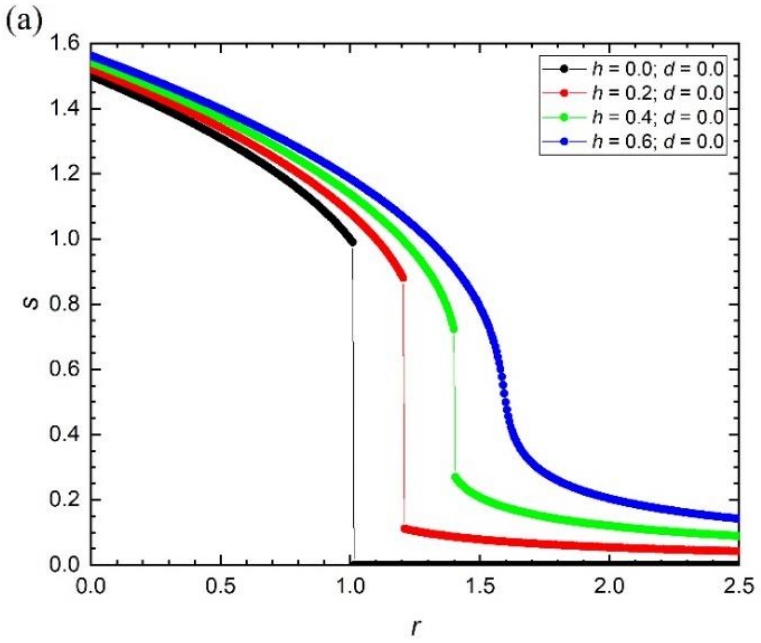

(b)

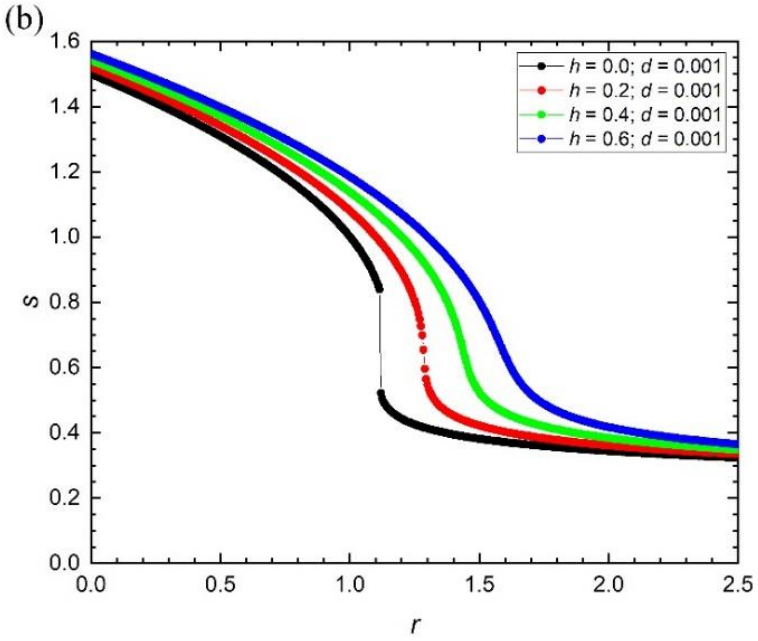
h = 0.0; d = 0.001
h = 0.2; d = 0.001
h = 0.4; d = 0.001
h = 0.6; d = 0.001
s
r
0.0
0.2
0.4
0.6
0.8
1.0
1.2
1.4
1.6
0.5
1.5
2.0
2.5

(c)

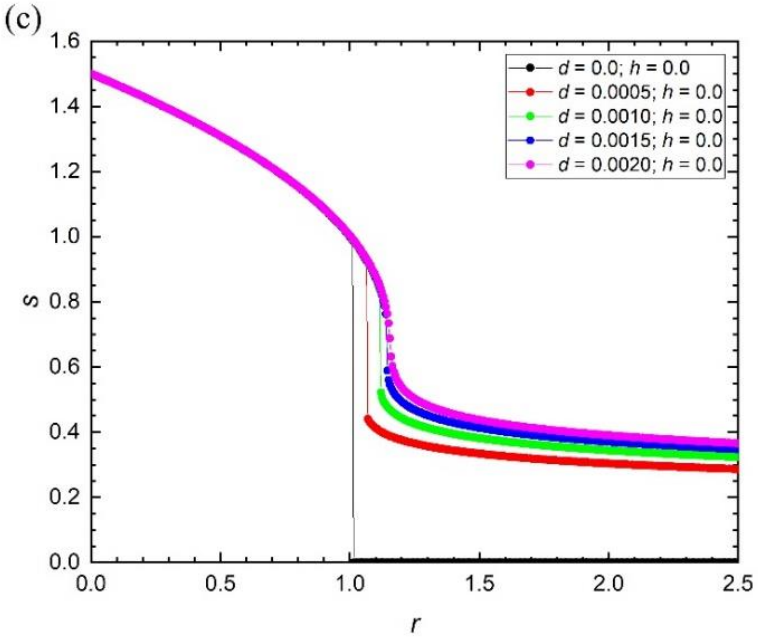
d = 0.0; h = 0.0
d = 0.0005; h = 0.0
d = 0.0010; h = 0.0
d = 0.0015; h = 0.0
d = 0.0020; h = 0.0
s
r
0.0
0.2
0.4
0.6
0.8
1.0
1.2
1.4
1.6
0.5
1.5
2.0
2.5

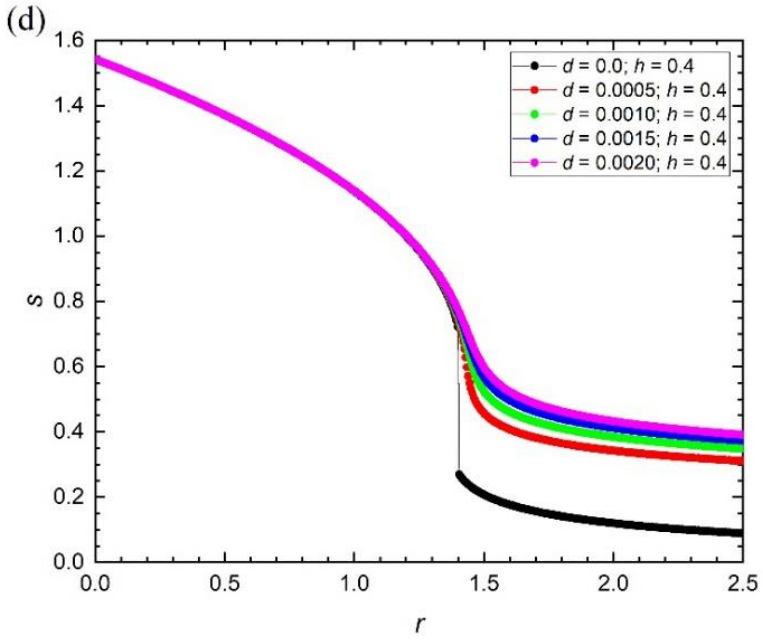

Figure 52: Order parameter s as a function of temperature r. (a) The applied stress h is varied with the disorder strength being held at a constant value $d = 0.0$. (b) The applied stress h is varied with the disorder strength being held at a constant value $d = 0.001$. (c) The disorder strength d is varied with the applied stress being held at a constant value $h = 0.0$. (d) The disorder strength d varied with the applied stress being held at a constant value $h = 0.4$ [240].

Figure 53 shows the derivative ds/dr as a function of temperature r [240]. We observe that as the system approaches the critical value, as we increase both h and d, the peak value of $|ds/dr|$ decreases and becomes broader. Given these results, what would be expected is that the eC response decreases. This is based on Equation (70), where an adiabatic temperature change of a material experiencing uniaxial stress is:

$$\Delta T(T,\sigma) = -\int_{\sigma_1}^{\sigma_2} \frac{T}{\rho c_\sigma}\left(\frac{\partial \lambda}{\partial T}\right)_\sigma d\sigma. \tag{116}$$

From the term $(\partial\lambda/\partial T)_\sigma$, where $\lambda = l/l_0$ is the relative length and l_0 is the length of the sample in the I phase, we can see that the greater the change in length as a function of temperature at a constant uniaxial stress, the greater the temperature change. This term is associated with the thermomechanical response. In practice, this would mean that samples with a greater crosslinker concentration and greater preloading express a smaller temperature change. This makes sense if we look at Equation (111), where the eC response depends on the difference between the value of the order parameter Q in an initial (T_1, σ_1) and final state (T_2, σ_2). In this model, this would be the difference between $s_1(r_1, h_1)$ and $s_2(r_2, h_2)$. Any influence decreasing this difference will directly impact the eC response.

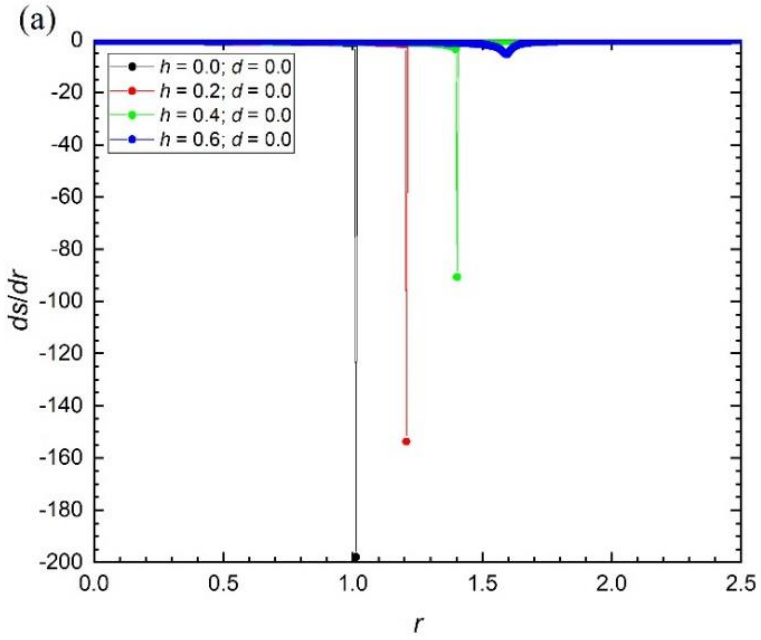
(a)
h = 0.0; d = 0.0
h = 0.2; d = 0.0
h = 0.4; d = 0.0
h = 0.6; d = 0.0
ds/dr
r
0
-20
-40
-60
-80
-100
-120
-140
-160
-180
-200
0.0
0.5
1.0
1.5
2.0
2.5

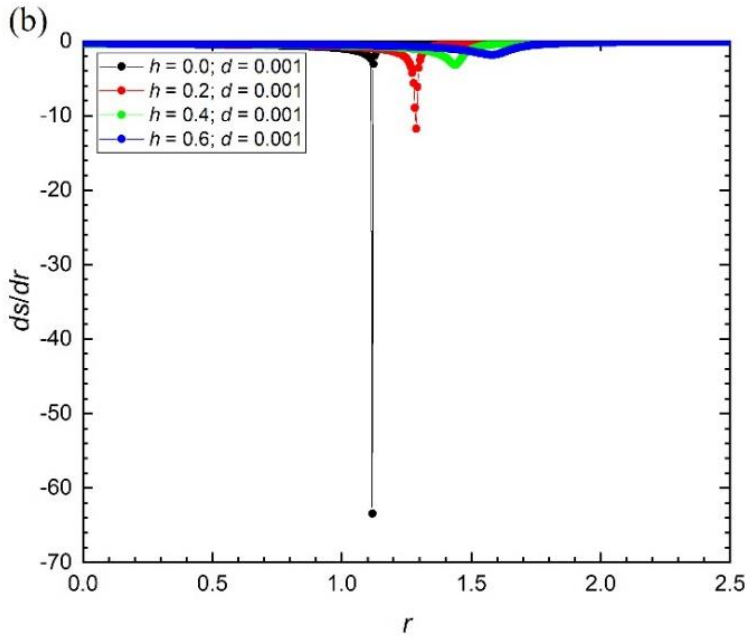
(b)
h = 0.0; d = 0.001
h = 0.2; d = 0.001
h = 0.4; d = 0.001
h = 0.6; d = 0.001
ds/dr
r
0
-10
-20
-30
-40
-50
-60
-70
0.0
0.5
1.0
1.5
2.0
2.5

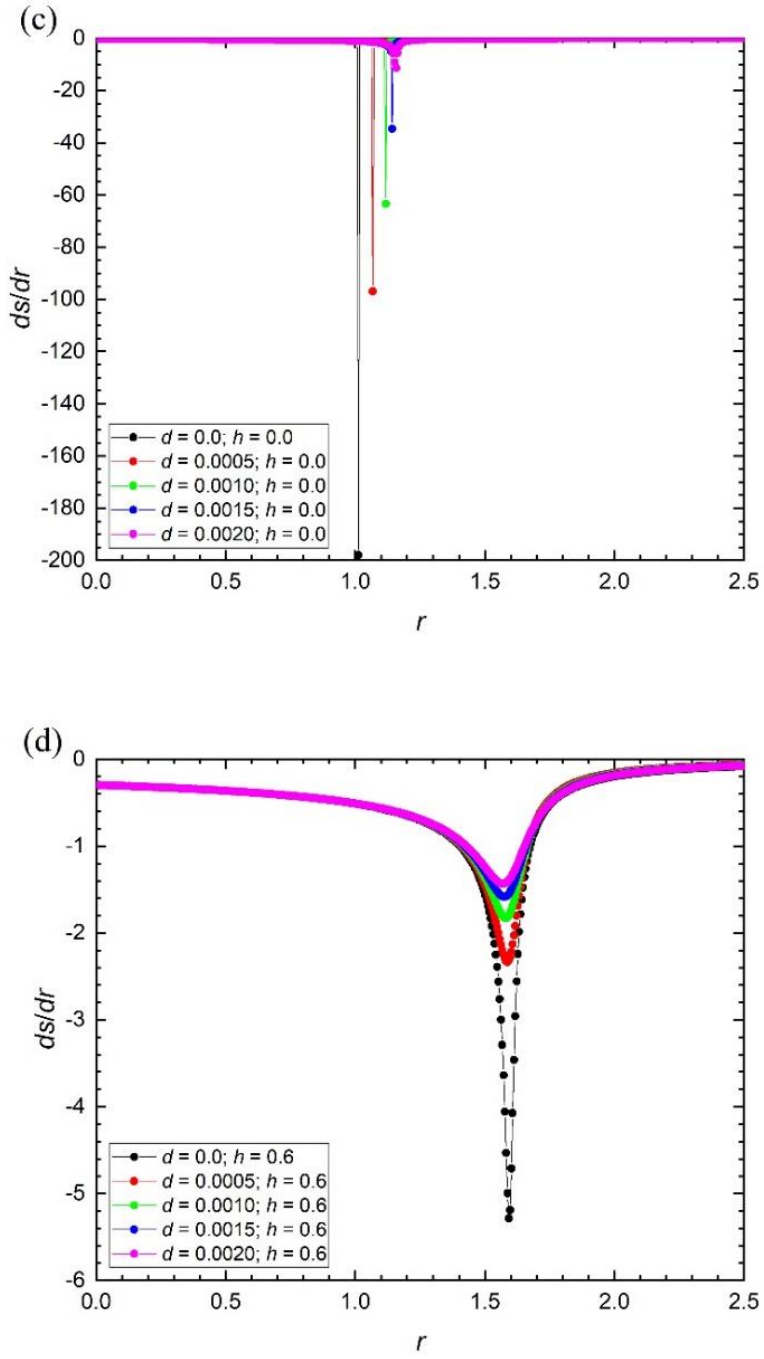

Figure 53: Derivative ds/dr as a function of temperature r. (a) The applied stress h is varied with the disorder strength being held at a constant value $d = 0.0$. (b) The applied stress h is varied with the disorder strength being held at a constant value $d = 0.001$. (c) The disorder strength d is varied with the applied stress being held at a constant value $h = 0.0$. (d) The disorder strength d is varied with the applied stress being held at a constant value $h = 0.6$ [240].

Figure 54 shows the eC temperature change Δr_{eCE} as a function of temperature r, where the sample is preloaded with a constant stress h_p and we vary the applied external stress h_e and disorder strength d [240]. We observe that an increasing h_e leads to a larger

Δr_{eCE}, which is expected. On the other hand, an increase in d leads to a decrease in Δr_{eCE}. Figure 55 also shows Δr_{eCE} as a function of r, only this time, we apply the same h_e but with different h_p and varying d [240]. As before, an increasing d leads to a smaller Δr_{eCE}, as well as an increasing h_p also leads to a smaller Δr_{eCE} and shifting the peak towards higher temperatures. Figure 56 shows Δr_{eCE} as a function of r, where the h_e and h_p are held at a constant value, but d is varied [240]. Again, an increasing d reduces Δr_{eCE}. In all three scenarios, the Δr_{eCE} peak was shifted towards higher temperatures. This can be understood by looking at Figure 52a. Looking at the difference in s between the lines with values of $h = 0.2$ and $h = 0.0$, the difference will be largest around the value of $r = 1.0$. On the other hand, looking at the difference between the lines with values of $h = 0.6$ and $h = 0.4$, the difference will be the largest around the value of $r = 1.4$. Hence the shift towards larger values of r.

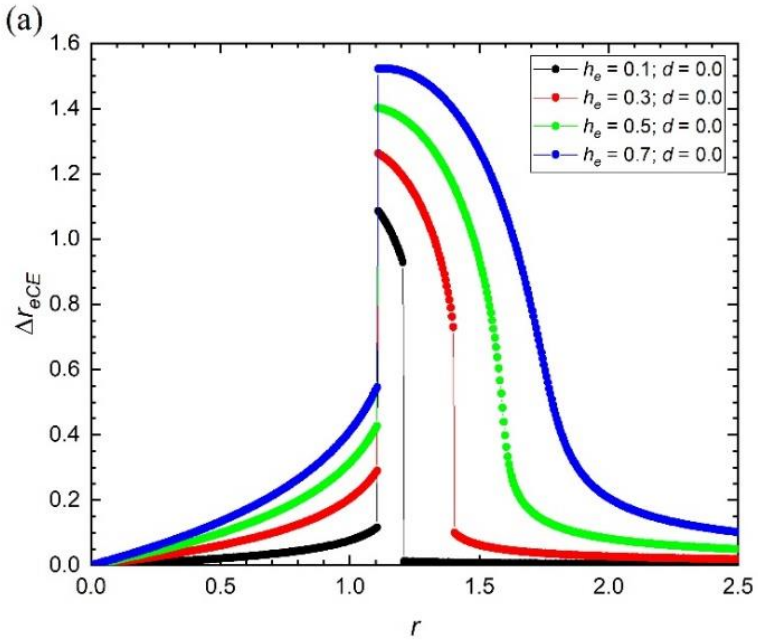

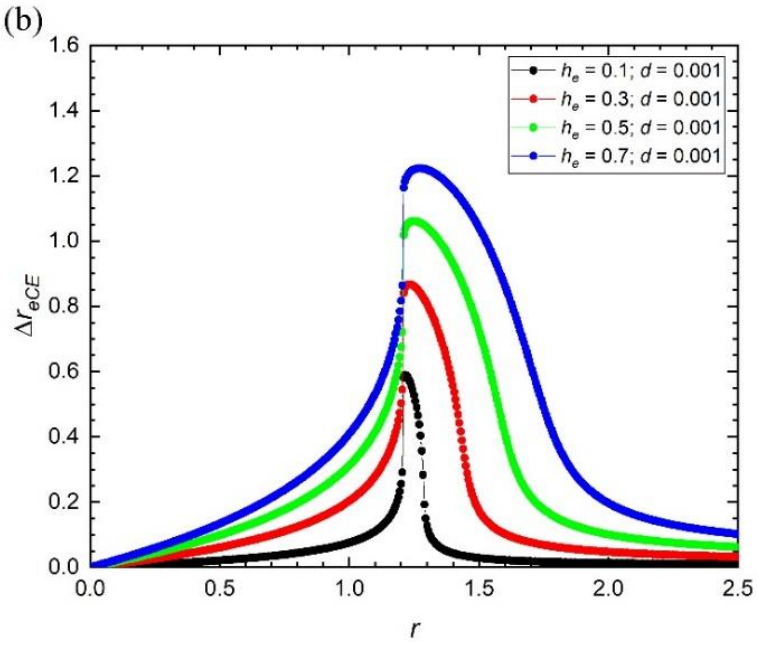

Figure 54: eC temperature change Δr_{eCE} as a function of temperature r. (a) The applied external stress h_e is varied with the preloaded stress h_p and disorder strength being held at a constant value of $h_p = 0.1$ and $d = 0.0$. (b) The applied external stress h_e is varied with the preloaded stress h_p and disorder strength being held at a constant value of $h_p = 0.1$ and $d = 0.001$ [240].

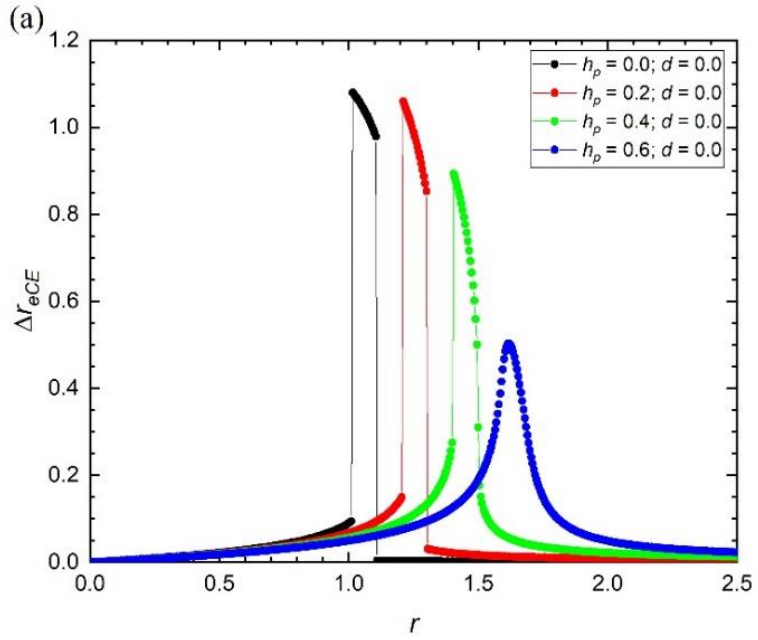

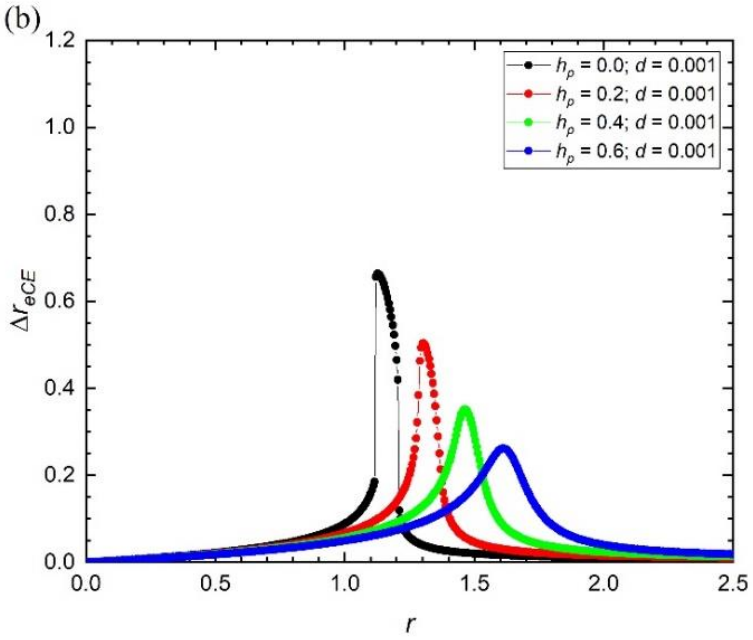

Figure 55: eC temperature change Δr_{eCE} as a function of temperature r. (a) The preloaded stress h_p is varied with the applied external stress h_e and disorder strength being held at a constant value of $h_e = 0.1$ and $d = 0.0$. (b) The preloaded stress h_p is varied with the applied external stress h_e and disorder strength being held at a constant value of $h_e = 0.1$ and $d = 0.001$ [240].

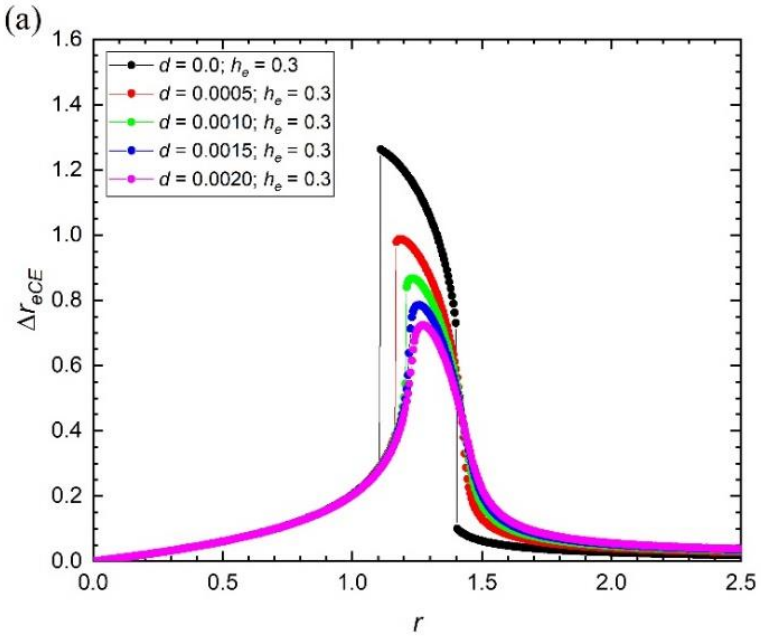

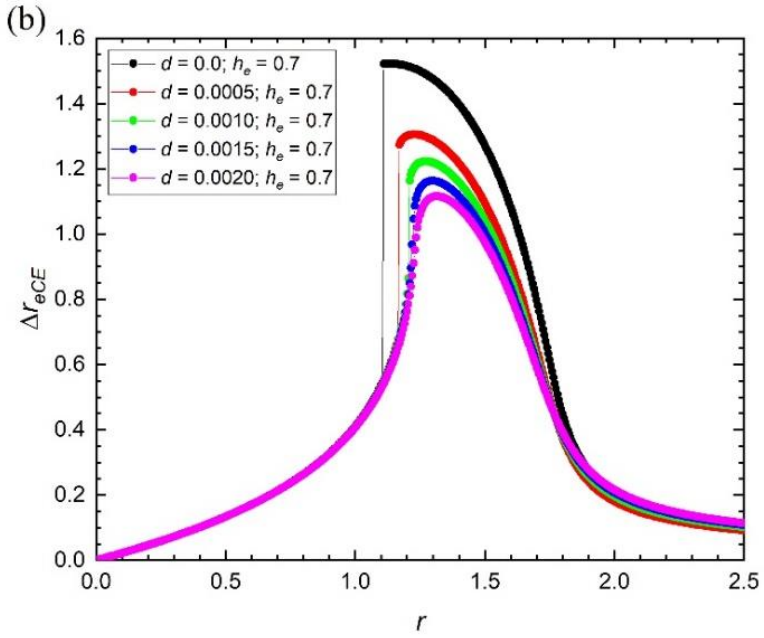

Figure 56: eC temperature change Δr_{eCE} as a function of temperature r. (a) The disorder strength d is varied with the applied external stress h_e and preloaded stress h_p being held at a constant value of $h_e = 0.3$ and $h_p = 0.1$. (b) The disorder strength d is varied with the applied external stress h_e and preloaded stress h_p being held at a constant value of $h_e = 0.7$ and $h_p = 0.1$ [240].

Figure 57 shows the largest eC temperature change Δr_{eCE} as a function of applied stress h, at various temperatures r and a fixed value of disorder strength d [240]. Below a certain critical temperature, Δr_{eCE} increases continuously with an increasing stress h. Above the critical temperature, once the stress reaches a critical value, Δr_{eCE} jumps and afterward continues to increase. A crossover point exists above the critical temperature where the system's Δr_{eCE} at a lower r becomes smaller than at a higher r. An increasing d decreases Δr_{eCE} and shifts the critical temperature towards higher values.

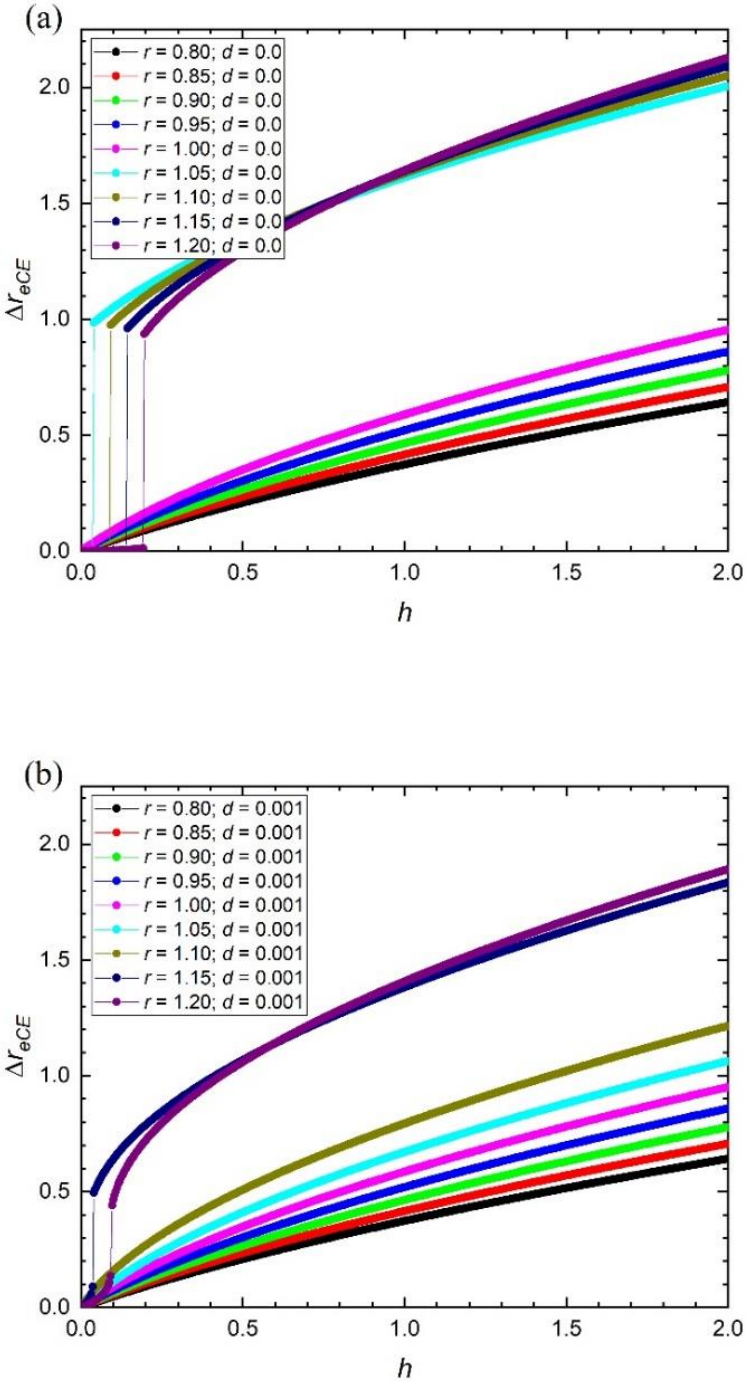

Figure 57: eC temperature change Δr_{eCE} as a function of stress h. (a) The temperature r is varied with the disorder strength d being held at a constant value of $d = 0.0$. (b) Temperature r is varied with the disorder strength d being held at a constant value of $d = 0.001$ [240].

Figure 58 shows the eC temperature change Δr_{eCE} as a function of the applied external stress h_e, with varying values of the preloaded stress h_p and a fixed value of the disorder strength d [240]. Interestingly, at extremely low values of h_e, the systems with a smaller h_p display a larger Δr_{eCE}. However, this is true only up to a certain critical value of h_e

after which there is a crossover and the systems with a larger h_p display a larger Δr_{eCE}. The impact of d is that it lowers the Δr_{eCE}, and shifts the critical h_e to larger values.

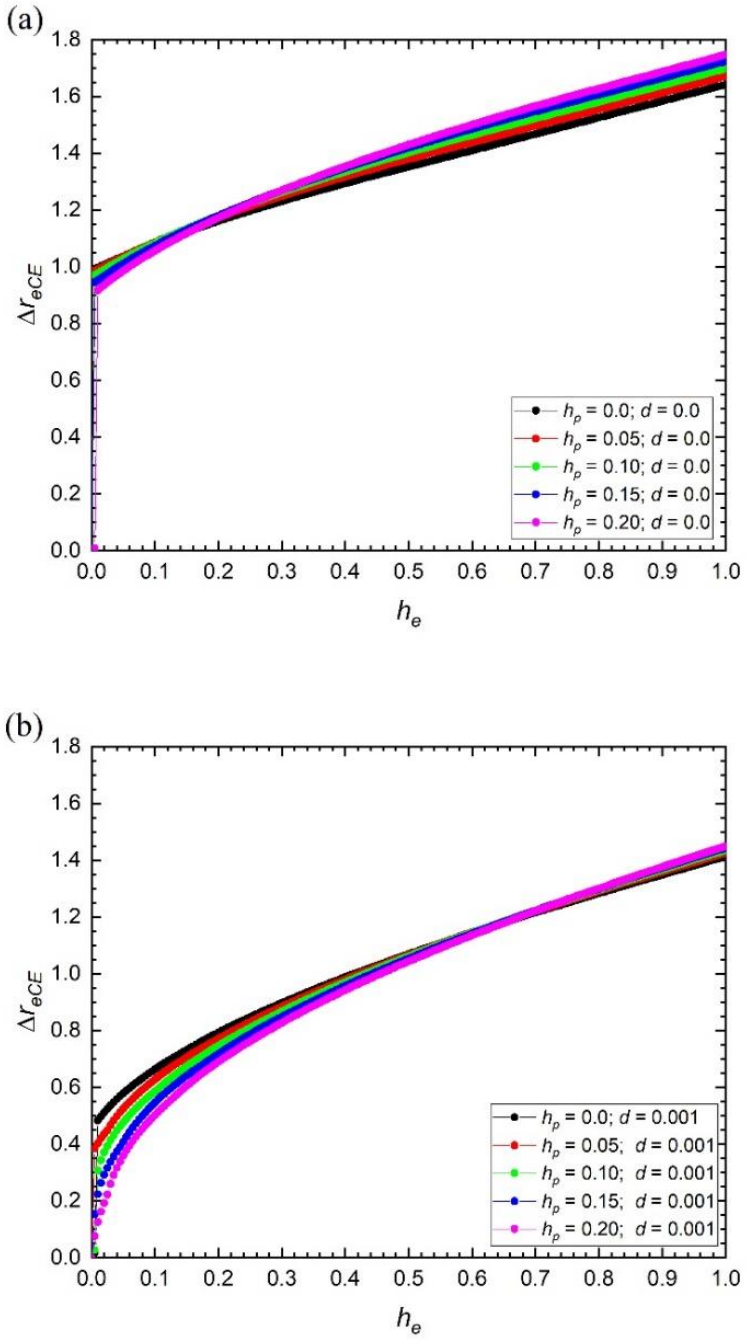

Figure 58: Largest eC temperature change Δr_{eCE} as a function of applied external stress h_e. (a) The preloaded stress h_p is varied with the disorder strength d being held at a constant value of $d = 0.0$. (b) The preloaded stress h_p is varied with the disorder strength d being held at a constant value of $d = 0.001$ [240].

Another important quantity is the eC responsivity. It is defined as the ratio between the eC temperature change Δr_{eCE} and the applied stress Δh. It can be interpreted as a kind of system efficiency: how much work is put into the system versus how large of a temperature change was achieved. Figure 59 shows the eC responsivity $\Delta r_{eCE}/\Delta h_e$ as a

function of the applied external stress h_e, where we varied the preloaded stress h_p and held the disorder strength d constant [240]. We observe that the $\Delta r_{eCE}/\Delta h_e$ is large at extremely low values of h_e followed by a gradual drop. We also observe that the peak value is dependent on h_p. Increasing both h_p and d causes the sharp peak to disappear. We are left with a continuous increase of $\Delta r_{eCE}/\Delta h_e$ towards a certain level, which remains almost constant with increasing h_e.

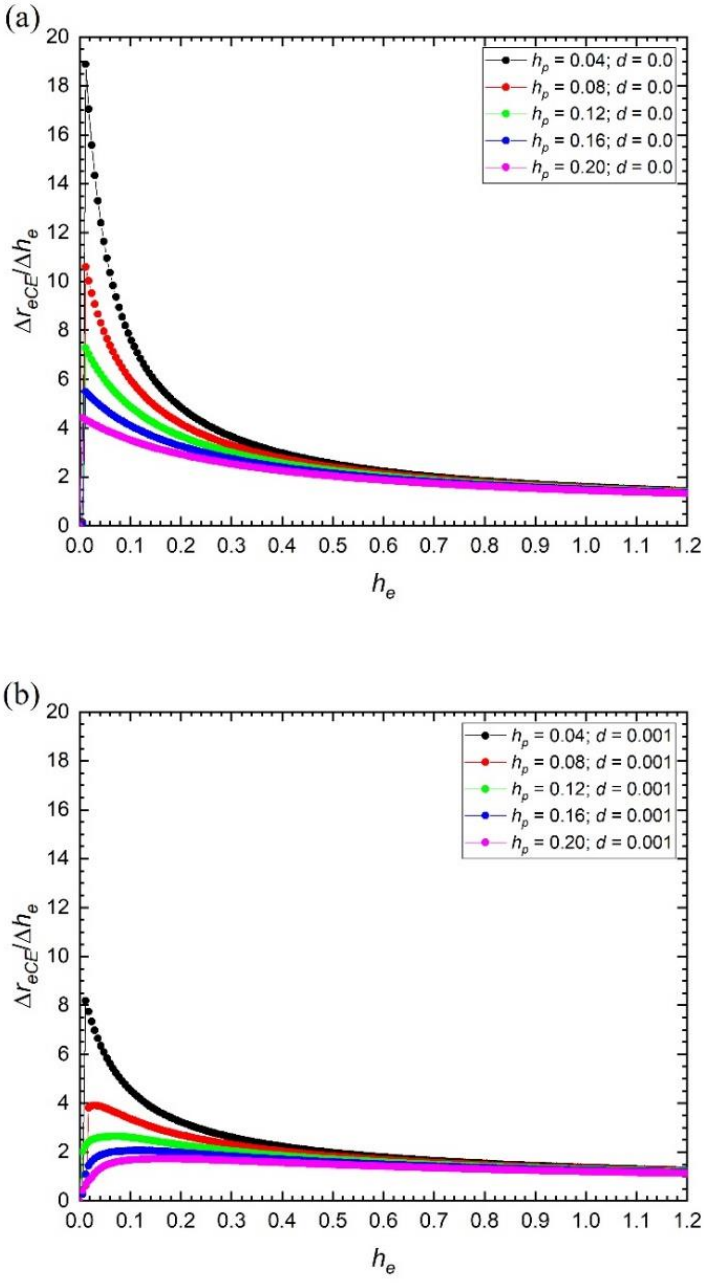

Figure 59: eC responsivity $\Delta r_{eCE}/\Delta h_e$ as a function of the applied external stress h_e. (a) The preloaded stress h_p is varied with the disorder strength d being held at a constant value of $d = 0.0$. (b) The preloaded stress h_p is varied with the disorder strength d being held at a constant value of $d = 0.001$ [240].

What can be learned from this model is that an MC-LCE system will exhibit a larger Δr_{eCE} if h_e is larger, and if h_p, as well as d, are smaller. Also, larger Δr_{eCE} will be

exhibited in the vicinity of the phase transition temperature. The peak of Δr_{eCE} will also tend to shift towards higher temperatures under an increase in h_e, h_p, and d. On the other hand, it is shown that $\Delta r_{eCE}/\Delta h$ will be the largest at very small values of h_e. In a practical sense, this means that the responsivity of the system is high at small values of h_e. However, a larger Δr_{eCE} can still be achieved at larger values of h_e, but with increasingly lowered responsivity $\Delta r_{eCE}/\Delta h$ increasingly larger fields will be required. Therefore, the construction of a heat management device based on MC-LCE will have to consider this. A compromise between the good responsivity and the actual magnitude of the eCE will have to be met.

3.9.2 Calorimetry results of main-chain liquid crystalline elastomers with varying crosslinker concentration

High-resolution calorimetry measurements were performed to determine whether MC-LCE exhibit a first- or second-order phase transition between the N and PN state. Figure 60 shows the experimentally obtained results of AC calorimetry of MC-LCE with crosslinker concentrations $\chi = 0.05$, $\chi = 0.06$, $\chi = 0.07$, $\chi = 0.08$, $\chi = 0.09$, and $\chi = 0.10$ [240–242]. With increasing crosslinker concentration, the phase transition changes from being weakly first-order at low crosslinker concentrations ($\chi \leq 0.07$) to second-order or supercritical at high crosslinker concentrations ($\chi \geq 0.08$). This gives an indication that there might also be some latent heat present at the phase transition in the low crosslinker concentration samples. These results are in good agreement with previous such measurements performed by Cordoyiannis et al. [53]. Using relaxation calorimetry, it was determined that only the $\chi = 0.05$ sample had any detectable amount of latent heat, and even this amount was relatively small, at $L = 0.096$ J/gK. From this, it can be inferred that none of the low concentration samples is truly first-order. While reducing the crosslinker concentration, even more, might produce a sample with a first-order phase transition accompanied with a large amount of latent heat, it turns out that such MC-LCE samples are, at least at present, for us impossible to produce, since they become chemically unstable. They resemble an LC polymer more than they do an LCE. Increasing the crosslinker concentration shifts the phase transition temperature T_C towards higher values. Since increasing the crosslinker concentration makes the elastomer matrix more rigid, it requires more thermal energy to overcome this rigidity. The N phase becomes more stable. Based on these calorimetry results, expectations are that the lower crosslinker concentration samples will give a better eCE than the higher concentration samples.

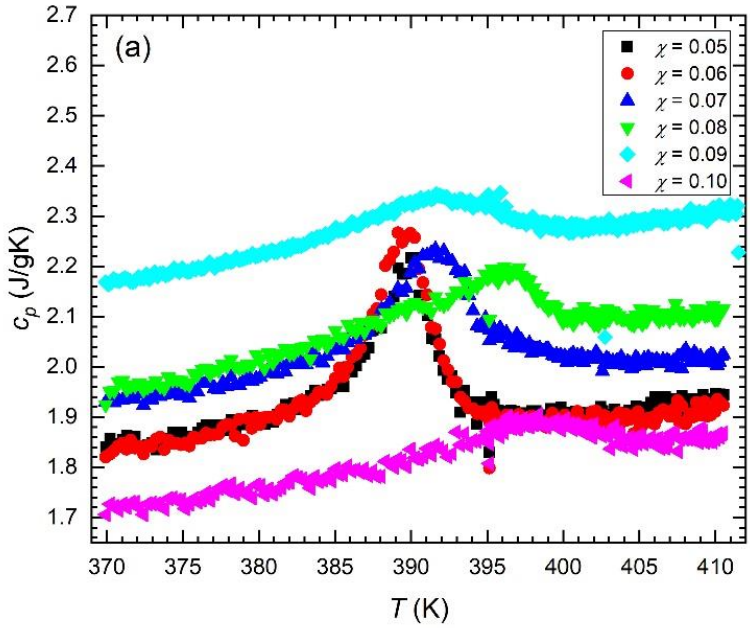
(a)
χ = 0.05
χ = 0.06
χ = 0.07
χ = 0.08
χ = 0.09
χ = 0.10
c_p (J/gK)
T (K)

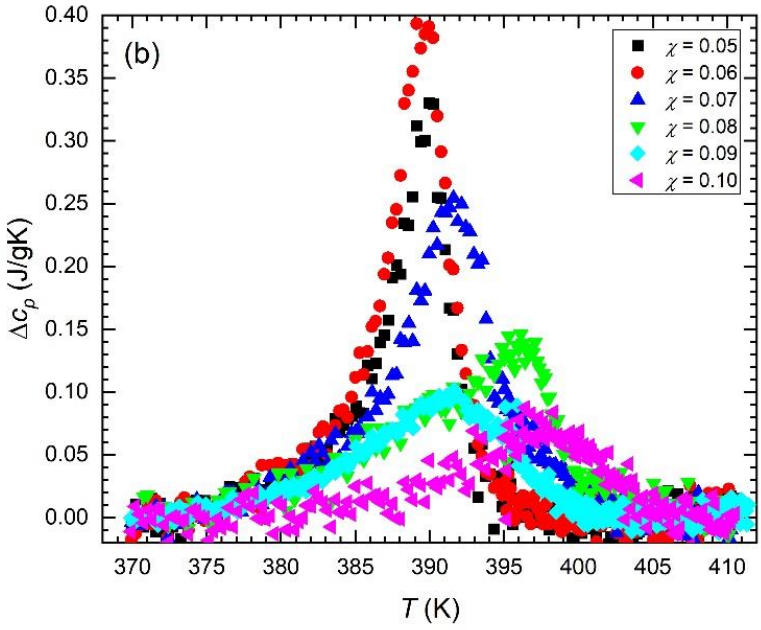
(b)
χ = 0.05
χ = 0.06
χ = 0.07
χ = 0.08
χ = 0.09
χ = 0.10
Δc_p (J/gK)
T (K)

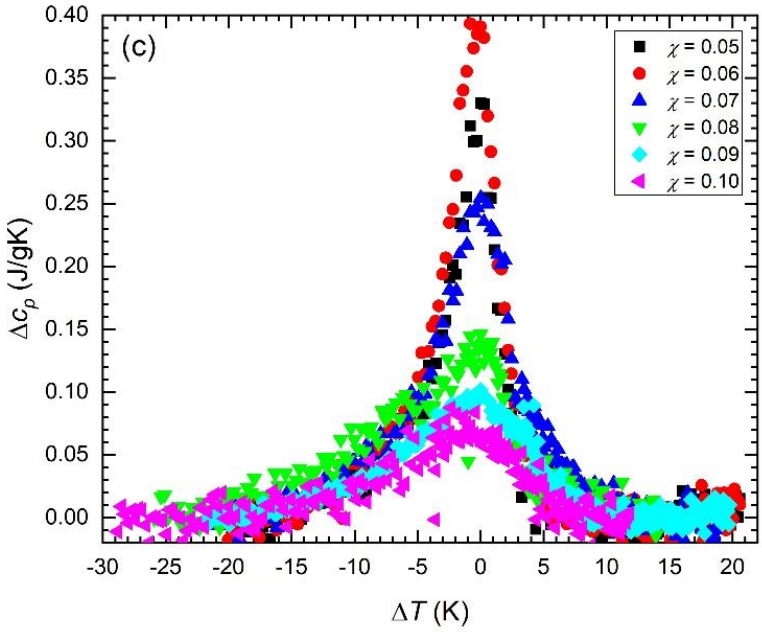

Figure 60: a) Calorimetry measurement results for MC-LCE with various crosslinker concentrations χ. b) Excess specific heat capacity density Δc_p as a function of temperature T. It expresses only the order parameter fluctuation contribution to c_p. c) Excess specific heat capacity density Δc_p as a function of $\Delta T = T_C - T$, so that all the peaks are aligned [240–242].

3.9.3 Thermomechanical results of main-chain liquid crystalline elastomers with varying crosslinker concentration

By measuring the thermomechanical response, one can either confirm or refute the conclusions from the calorimetry measurement results that lower crosslinker concentration samples will have a larger temperature change ΔT_{eCE}. It is expected that the lower concentration samples would have a steeper $l(T)$ curve in the vicinity of the phase transition. This is precisely what is observed. Figure 61 shows $\lambda = l/l_0$, where l_0 is the sample length in the I phase, as a function of temperature T for three samples with crosslinker concentrations $\chi = 0.06$, $\chi = 0.07$, and $\chi = 0.08$, and Figure 62 shows the derivative $d\lambda/dT$ in the vicinity of the phase transition temperature [240,241]. It can be clearly seen that reducing the crosslinker concentration increases $|d\lambda/dT|$. These experimental results are in good agreement with the theoretical results in MC-LCE obtained by Skačej [243], as well as with our own simulations.

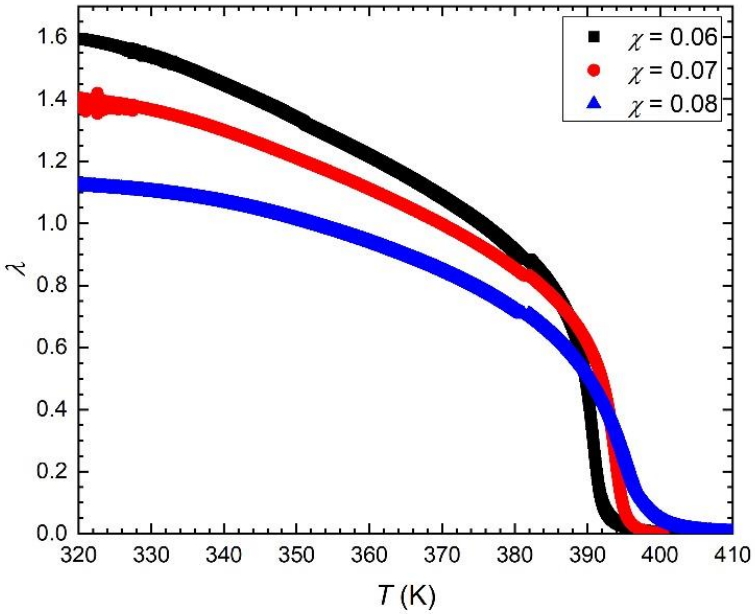

Figure 61: Thermomechanical response of three samples with crosslinker concentrations $\chi = 0.06$, $\chi = 0.07$, and $\chi = 0.08$ [240,241].

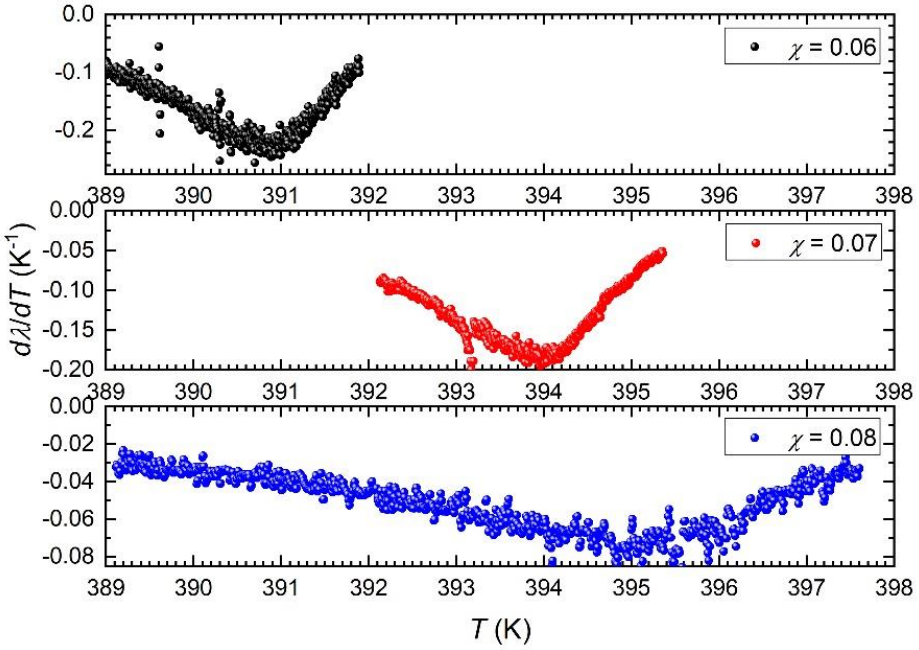

Figure 62: The derivative $d\lambda/dT$ of three samples with crosslinker concentrations $\chi = 0.06$, $\chi = 0.07$, and $\chi = 0.08$. It can be seen that decreasing χ leads to an increase in the value of $|d\lambda/dT|$ and thus is expected to increase the eC response ΔT_{eCE} [240,241].

3.9.4 Elastocaloric effect measurement results of main-chain liquid crystalline elastomers with varying crosslinker concentrations

Here we present the experimental results obtained from direct eC measurements of MC-LCE with various crosslinker concentrations. Each sample was stretched for various percentages of its current length around the vicinity of the phase transition temperature T_C (Figure 63) [240–242]. It can be seen that for larger stretches T_C shifts to higher values. Interpolation was used on the measured data points in order to determine the value of the largest eC response ΔT_{eCE} is and at which temperature T.

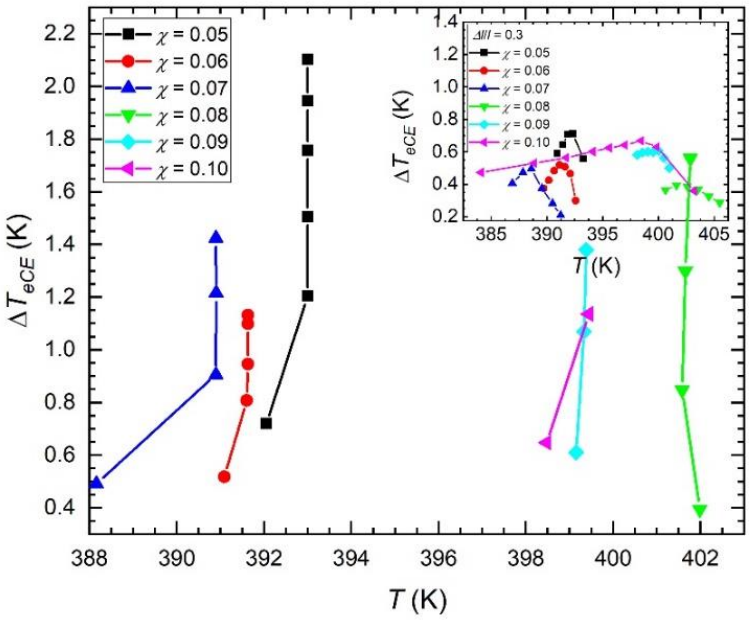

Figure 63: Measurement results of the eC response ΔT_{eCE} as a function of temperature T. The inset shows the measured ΔT_{eCE} for sample extensions of $\Delta l/l = 0.3$ measured in the vicinity of T_C [240–242].

Figure 64 shows the eC response as a function of relative extension $\Delta l/l$. Length l, in this case, is the length of the sample at the current temperature [241]. The largest eC response is achieved by the sample with crosslinker concentrations $\chi = 0.05$. Interestingly the lowest eC response was shown by the $\chi = 0.06$ sample. Samples with larger crosslinker concentrations have ΔT_{eCE} values lying in between the values of the $\chi = 0.05$ and $\chi = 0.06$ samples, with the value of ΔT_{eCE} increasing with crosslinker concentration. We can also see that the samples tend to tear sooner with increasing crosslinker concentration. These results, however, do not tell how much work, in the form of applied uniaxial stress, was used to achieve these relative extensions.

Much more interesting for applicational purposes is the eC response ΔT_{eCE} as a function of applied stress $\Delta\sigma$. Figure 65a shows that, similarly to before, the largest ΔT_{eCE} was achieved by the $\chi = 0.05$ sample for intermediate and large values of $\Delta\sigma$ [240–242]. On the other hand, unlike before, now the increase in crosslinker concentration leads to smaller ΔT_{eCE} at a similar $\Delta\sigma$. A peculiar response is shown by the $\chi = 0.06$ sample, which at low $\Delta\sigma$ shows the largest ΔT_{eCE}, after which it begins to show a lower ΔT_{eCE} than the $\chi = 0.07$ and $\chi = 0.08$ samples at similar values of $\Delta\sigma$. Figure 65b shows the specific entropy change (per unit mass) $\Delta\omega_{eCE} = \Delta\Omega_{eCE}/m = c_p\Delta T_{eCE}/T$ as a function

of $\Delta\sigma$. It is used to calculate the value $\Delta T_{eCE}\Delta\Omega_{eCE}$ in order to estimate the performance of materials, which is similar to the refrigerant capacity $RC = (T_h - T_c)\Delta\Omega$ of the cooling cycle between the cold (T_c) and hot (T_h) ends. The maximum $\Delta\omega_{eCE}$ of 10.4 J/kgK is obtained in the $\chi = 0.05$ sample.

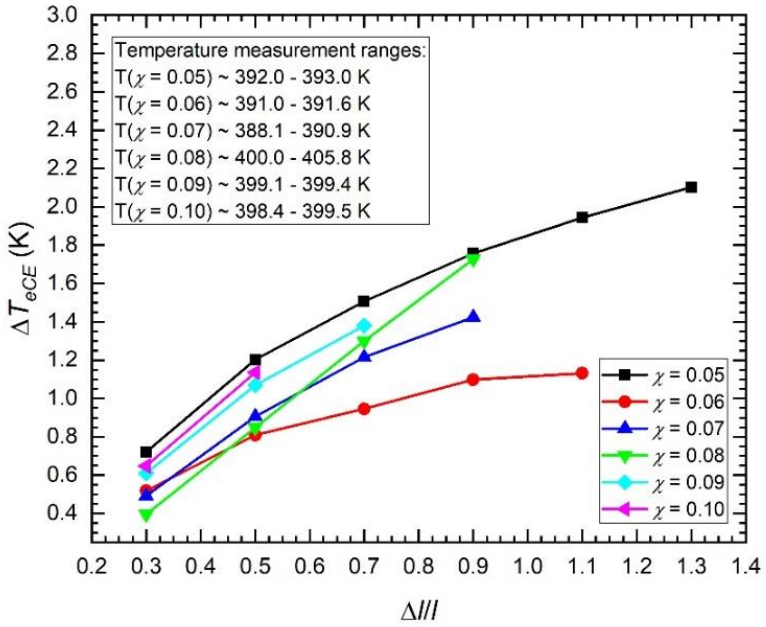

Figure 64: Measurement results of the eC response ΔT_{eCE} as a function of relative extension $\Delta l/l$ [241].

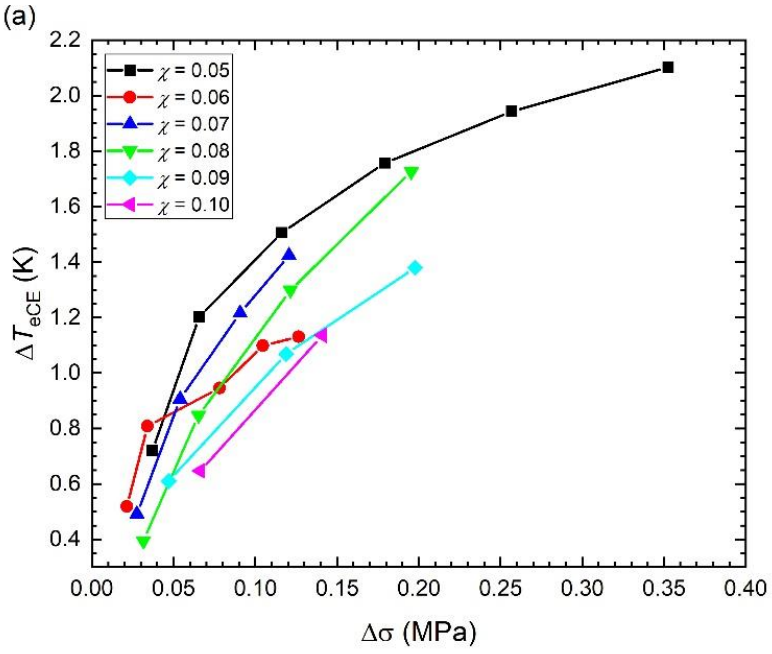

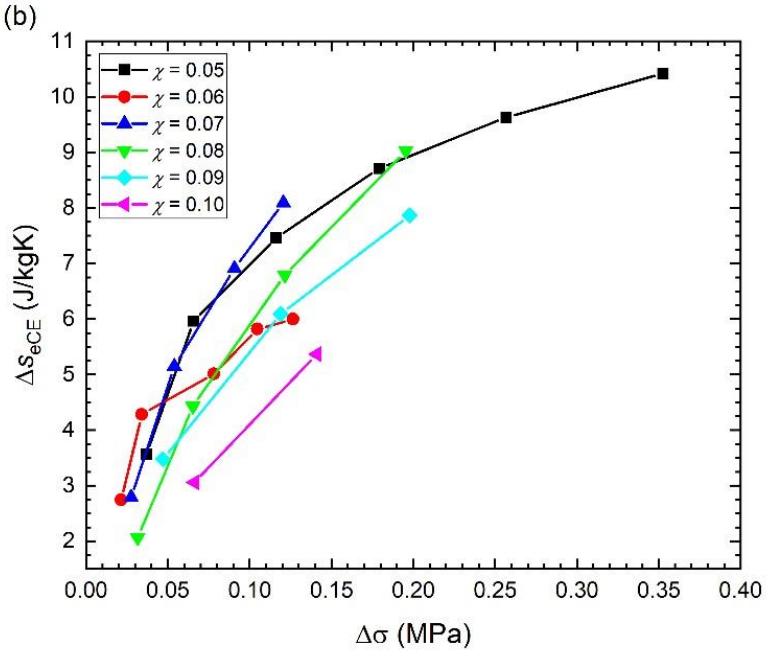

Figure 65: (a) Measurement results of the eC response ΔT_{eCE} as a function of applied uniaxial stress $\Delta\sigma$. (b) Calculated specific entropy change $\Delta\omega_{eCE}$ as a function of $\Delta\sigma$ [240–242].

Finally, we shall look at the eC responsivity $\Delta T_{eCE}/\Delta\sigma$ as a function applied stress $\Delta\sigma$. The eC responsivity can be considered as a measure of conversion efficiency between the applied stress $\Delta\sigma$ and eC response ΔT_{eCE}. Figure 66 shows that at low applied stress $\Delta\sigma$, the $\chi = 0.06$ sample has the most efficient conversion [240–242]. After which, $\Delta T_{eCE}/\Delta\sigma$ rapidly drops for intermediate values of $\Delta\sigma$. Aside from this small initial interval, the $\chi = 0.05$ sample displays the largest $\Delta T_{eCE}/\Delta\sigma$, making it the most efficient sample. We also notice that with increasing $\Delta\sigma$ the $\Delta T_{eCE}/\Delta\sigma$ decreases.

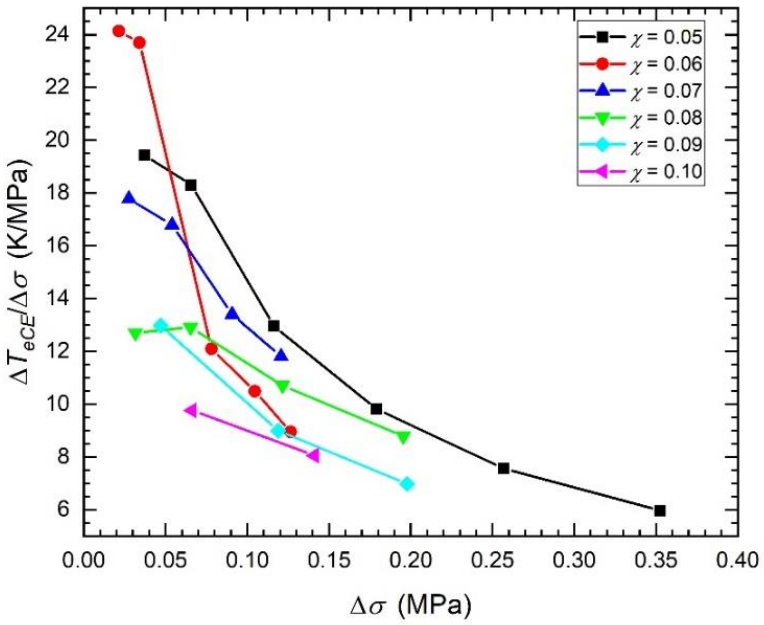

Figure 66: The eC responsivity $\Delta T_{eCE}/\Delta\sigma$ as a function of applied stress $\Delta\sigma$ [240–242].

From these comparisons of MC-LCE with varying crosslinker concentrations, we can conclude that lower crosslinker concentrations produce larger eC responses. They are also less prone to tearing at larger applied stresses. The anomalous behavior of the $\chi = 0.06$ sample was initially thought to be the consequence of minor tearing of the sample during stretching. However, this was refuted by performing another measurement of a $\chi = 0.06$ sample obtained from the same batch as the initial sample, whereby no significant differences in the sample's behavior were observed. This anomalous behavior could thus be attributed to systematic errors associated with the sample preparation. However, there also might be an alternative explanation. Returning to the mathematical model of MC-LCEs, by determining the values of r, h, and d, where the phase transition is first order, one can obtain a region in the $d-h-r$ phase diagram presented in Figure 67 [240,241]. The projections on the rh, rd, and hd planes, colored with blue, green, and red, respectively, determine the region of the first-order phase transition. The dark blue, light green, and dark red bold lines represent the projections of the line of critical points (r_{CP}, h_{CP}, d_{CP}), where the first-order phase transition terminates and becomes second-order. This line of critical points is represented by the black line in Figure 67 [123]. The line of critical points represents the uppermost limit of a combination of values r, h, and d, where the phase transition is still first-order. According to our specific heat results (Figure 60), the $\chi = 0.06$ sample lies very much near the line of critical points. Namely, the $\chi = 0.06$ sample exhibits the maximum in Δc_p and the $\chi = 0.05$ sample exhibits already first-order transition with a moderate latent heat value. In contrast, the samples with higher concentrations χ are increasingly supercritical. The application of a large enough σ to the sample at the critical point causes it to immediately pass into the supercritical regime, which is reflected as a sudden drop in $\Delta T_{eCE}/\Delta\sigma$. In contrast, the $\chi = 0.05$ sample with increasing σ first needs to reach the critical point before entering the supercritical region, thus, slightly elevated values of $\Delta T_{eCE}/\Delta\sigma$ persisting to higher stress-field values. As the critical point is reached at a nonzero stress field in the $\chi = 0.05$ sample, the transition is

more smeared than in the near-critical $\chi = 0.06$ sample, leading to the slightly smaller peak values of $\Delta T_{eCE}/\Delta\sigma$. The samples with $\chi > 0.06$ are already supercritical exhibiting the $\Delta T_{eCE}/\Delta\sigma$ peak values similar to those found in supercritical tails of $\chi = 0.05$ and $\chi = 0.06$ samples. Similar effects were observed in single crystal $Pb(Mg_{1/3}Nb_{2/3})O_3$-$PbTiO_3$ (PMN-PT) ferroelectric relaxors, where a large enough electric field could drive a first-order transition to terminate at a line of critical points and become supercritical for higher fields.

Using our phenomenological model for LCEs, the responsivity $\Delta r/\Delta h$ was calculated in the vicinity of the critical points around $h \sim 0.0$ and $d \sim 0.00175$, see the results presented in Figure 68 [240,241]. Note that d roughly corresponds to the crosslinker concentration χ. Initially, the responsivity slowly increases with an increasing d, until it reaches a peak value around $d \sim 0.0017$, followed by a rapid drop. If one now plots $\Delta r/\Delta h$ as a function of h for constant values of d around this peak and compares it to the experimentally obtained plot $\Delta T_{eCE}/\Delta\sigma$ as a function of $\Delta\sigma$, it can be seen that they are qualitatively similar (Figure 69a and 69b) [240,241]. The eC responsivity $\Delta r/\Delta h$ exhibits much sharper drops for the near critical point values of d (Figure 69a), similar to what is experimentally observed for the $\Delta T_{eCE}/\Delta\sigma$ for the near-critical $\chi = 0.06$ sample (Figure 69b). This suggests that the experimentally observed anomalous behavior of the $\chi = 0.06$ sample is actually due to its proximity to the line of critical points.

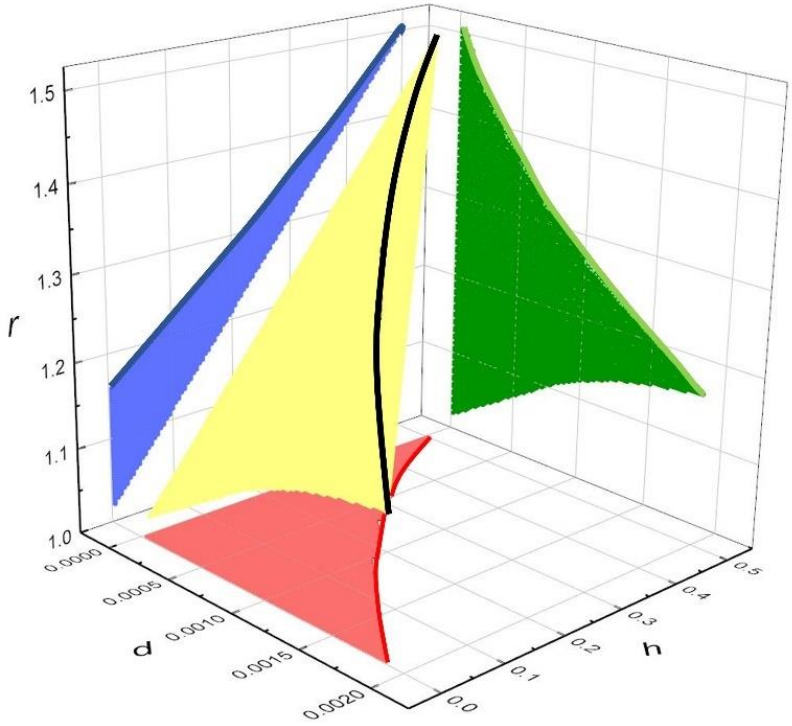

Figure 67: The $d - h - r$ phase diagram for the first-order phase transition in MC-LCEs. The black line represents the line of critical points r_{CP}, h_{CP}, and d_{CP}, where the first-order phase transition terminates and becomes second-order [240,241].

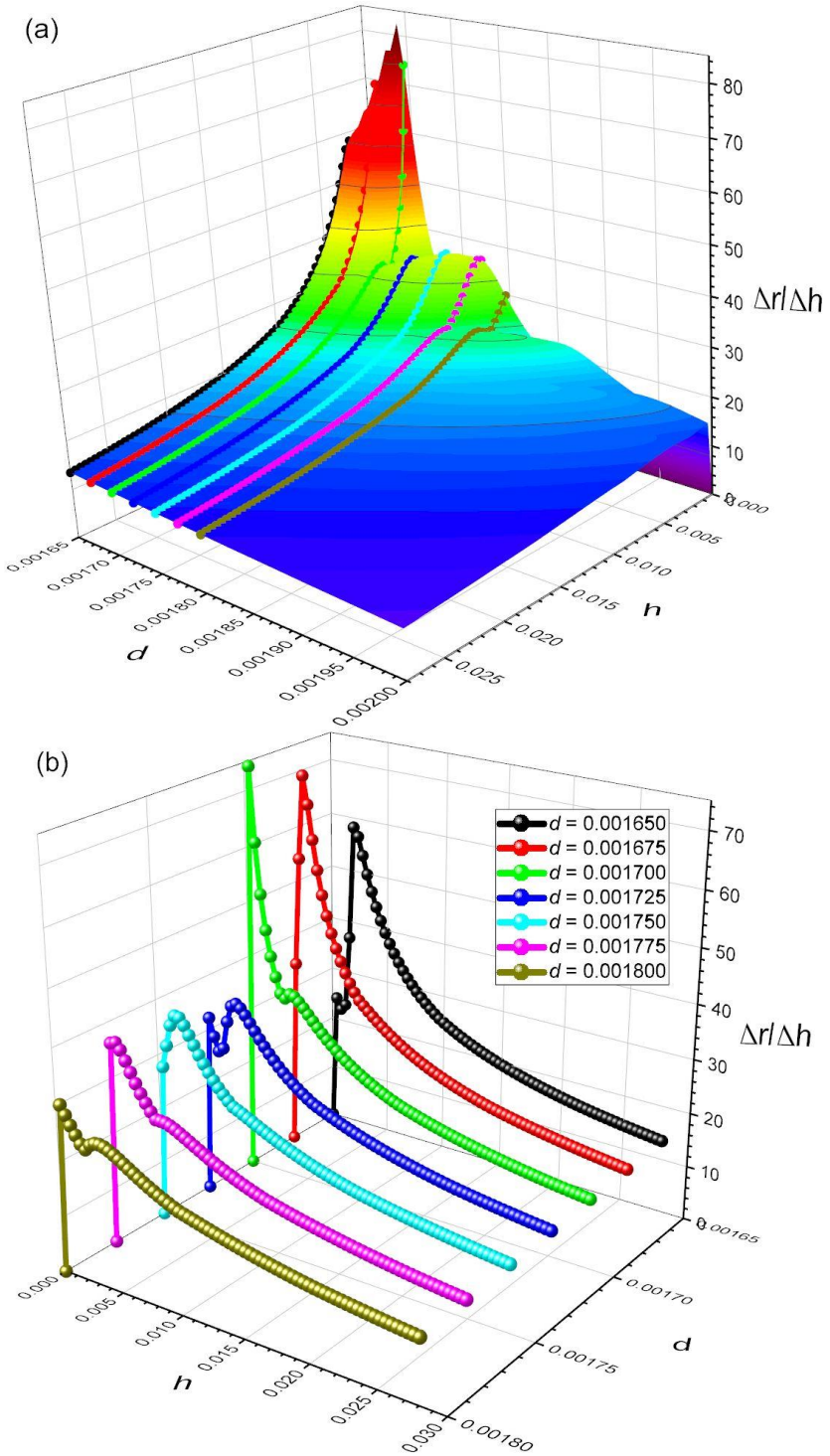

Figure 68: (a) The $d-h-\Delta r/\Delta h$ phase diagram in the vicinity of the critical points. (b) The $d-h-\Delta r/\Delta h$ phase diagram in the vicinity of the critical points for constant values of d around the $\Delta r/\Delta h$ peak [240,241].

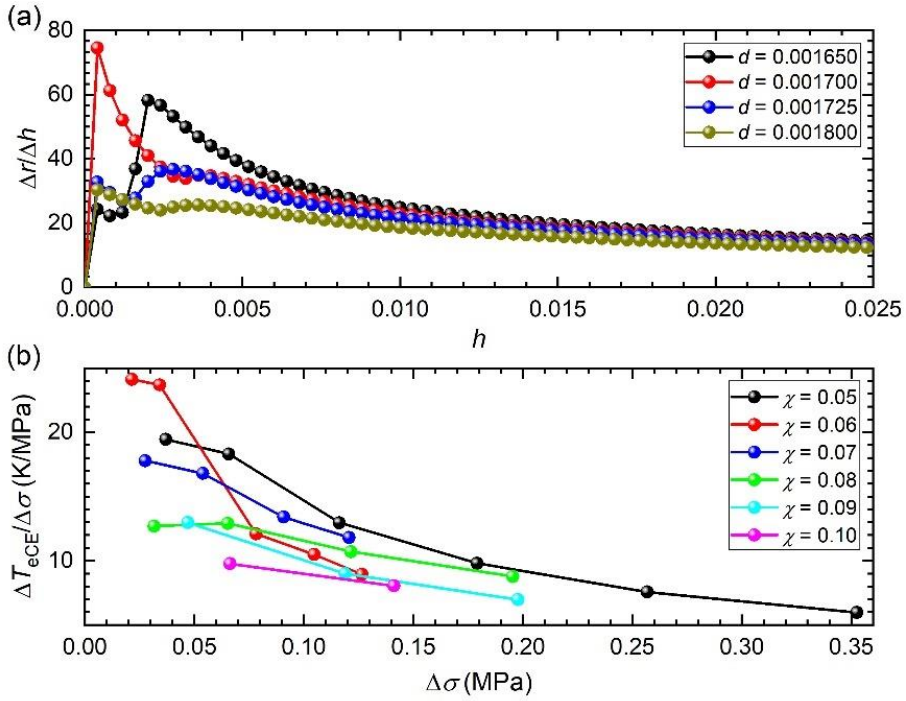

Figure 69: (a) The calculated eC responsivity $\Delta r/\Delta h$ as a function of h for different values of d. (b) The experimentally obtained eC responsivity $\Delta T_{eCE}/\Delta\sigma$ as a function of applied stress $\Delta\sigma$ for different values of crosslinker density χ [240,241].

3.9.5 Thermomechanical and elastocaloric effect measurement results of main-chain liquid crystalline elastomers crosslinked with varying loads

Thermomechanical and eCE measurement results of MC-LCE samples with a crosslinker concentration $\chi = 0.08$, which were stretched during the second crosslinking process at $T_{cross} = 343$ K using four different masses: sample 1 being stretched using $m_1 = 4.5$ g, sample 2 using $m_2 = 6.0$ g, sample 3 using $m_3 = 10.0$ g, and sample 4 using $m_4 = 20.0$ g, are presented. The different masses will cause a different orientational order to be imprinted into the elastomer network, with a larger mass producing a more ordered state than a smaller mass.

It has been demonstrated that crosslinking deeper in the N phase causes a shift in the N-I phase transition temperature, and the transition becomes supercritical [60,233]. It would appear as if applying a higher load during the second crosslinking step produces a similar effect as applying an external stress to a fully synthesized sample [244,245]. This is also what we see in our simulation results, when constant internal stress is present in the sample. Sample 1, crosslinked with a smaller load, is expected to produce a larger eC response.

Figures 70 and 71 show the thermomechanical response and its derivative for the samples [240,241]. Clearly, sample 1 displays a larger thermomechanical response than sample 2, followed by samples 3 and 4. This further confirms that sample 1 should display a larger eC response than the other samples. The shift in the phase transition temperature towards higher values is also observed.

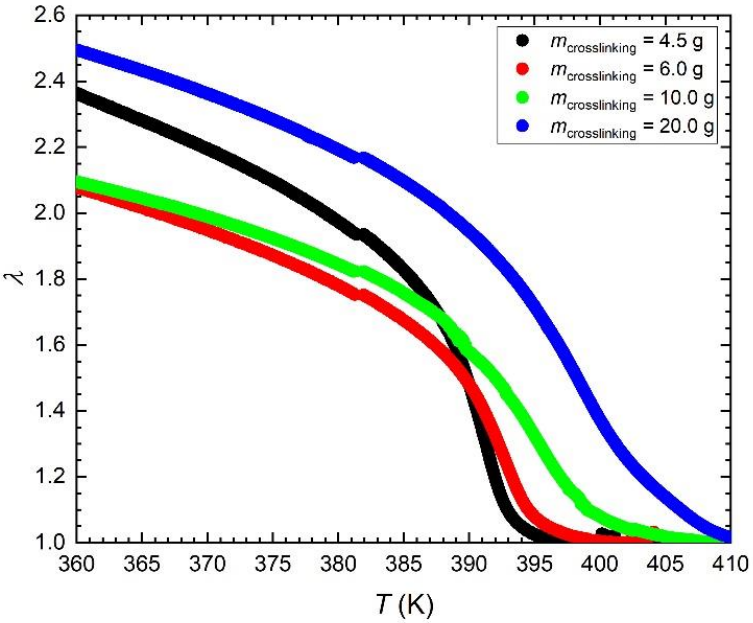

Figure 70: Thermomechanical response in the cooling run of samples crosslinked using different masses corresponding to different masses [240,241].

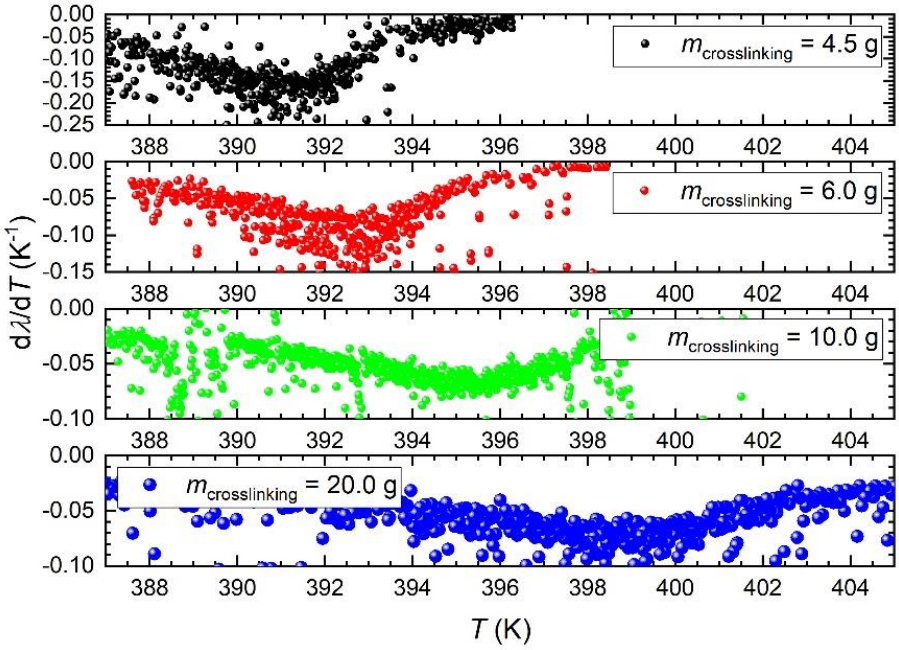

Figure 71: Derivative $d\lambda/dT$ in the cooling run. It is seen that the value of $|d\lambda/dT|$ is larger for sample 1, thus we expect a larger eC response from sample 1 than the other samples. The temperature shift of the phase transition temperature is also observed [240,241].

Figure 72 and 73 show the eC response ΔT_{eCE} as a function of temperature T and relative extension $\Delta l/l$ [240,241]. Initially, sample 1 experienced a larger ΔT_{eCE} in comparison to the other samples. At larger values of $\Delta l/l$, sample 3 experiences the largest ΔT_{eCE}. As previously stated, for applicational purposes, the much more important measure is the applied work in the form of $\Delta\sigma$ required to achieve such values of ΔT_{eCE}.

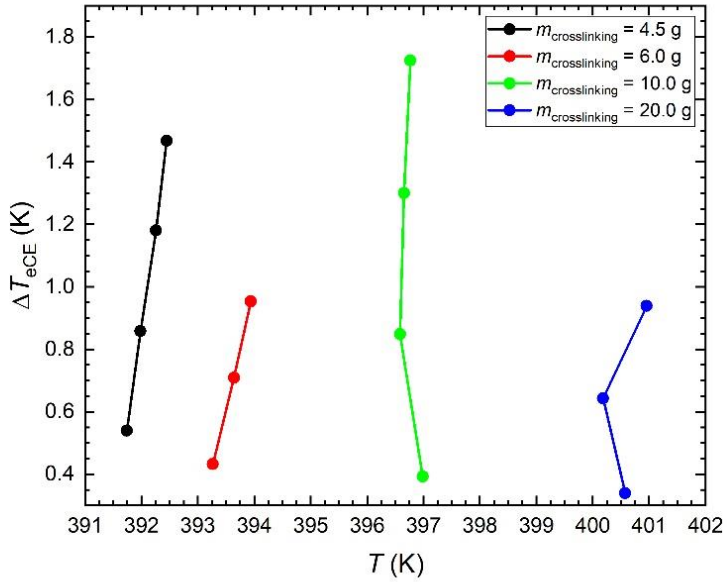

Figure 72: Measurement results of the eC response ΔT_{eCE} as a function of temperature T for samples stretched with different masses during the second crosslinking process. The measurements were performed in the vicinity of T_C [240,241].

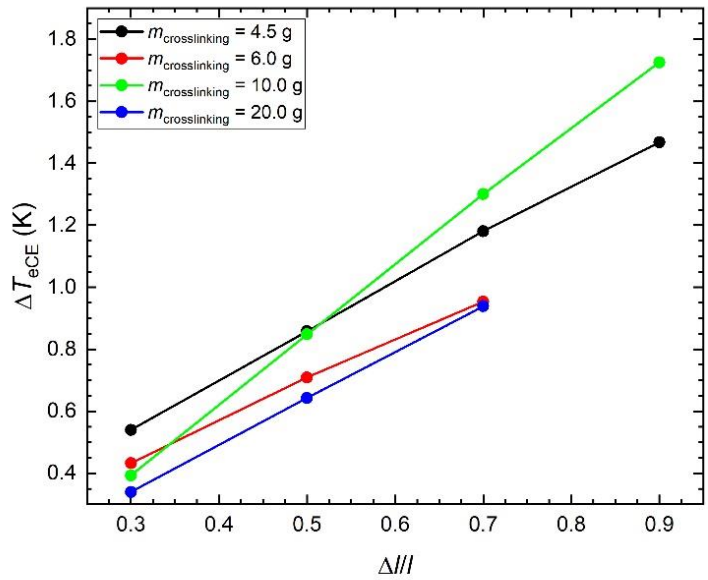

Figure 73: Measurement results of the eC response ΔT_{eCE} as a function of relative extension $\Delta l/l$ for samples stretched with different masses during the second crosslinking process [240,241].

The eC response ΔT_{eCE} and eC responsivity $\Delta T_{eCE}/\Delta\sigma$ as a function of applied stress $\Delta\sigma$ are presented in Figures 74 and 75 [240,241]. The disparity in ΔT_{eCE} between the samples is quite evident. The increase in ΔT_{eCE} as $\Delta\sigma$ is increased is much more drastic in samples 1 and 2 than in samples 3 and 4. The $\Delta T_{eCE}/\Delta\sigma$ clearly shows that crosslinking with a smaller mass creates a more efficient MC-LCE.

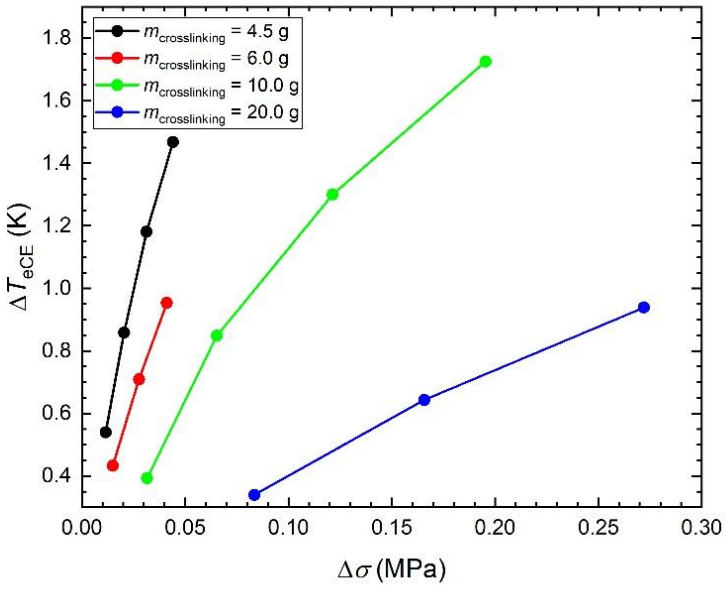

Figure 74: Measurement results of the eC response ΔT_{eCE} as a function of applied uniaxial stress $\Delta\sigma$ for samples stretched with different masses during the second crosslinking process [240,241].

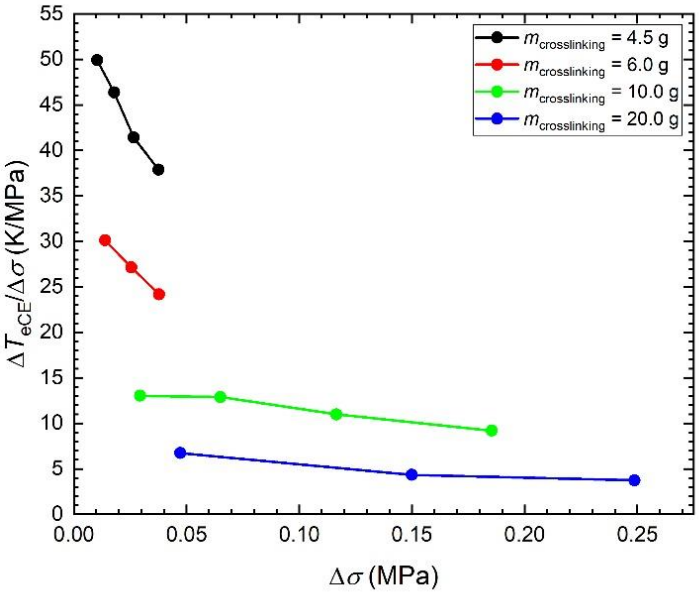

Figure 75: The eC responsivity $\Delta T_{eCE}/\Delta\sigma$ as a function of applied stress $\Delta\sigma$ for samples stretched with different masses during the second crosslinking process [240,241].

From these comparisons, we can conclude that sample 1, stretched using the smallest mass, produces the largest eC response, followed by samples 2, 3, and 4, which were stretched using heavier masses. It is also worth pointing out that all samples were crosslinked in the N phase. Due to the high phase transition temperatures and the nature of the synthesis process, we were unable to produce samples crosslinked in the I phase.

3.9.6 Thermomechanical and elastocaloric effect measurement results of main-chain liquid crystalline elastomers with varying crosslinking temperature

Next, we present the thermomechanical and eCE measurement results of three samples crosslinked at different crosslinking temperatures: sample 1 crosslinked at $T_1 = 313$ K, sample 2 at $T_2 = 343$ K, and sample 3 at $T_3 = 373$ K. Being crosslinked deeper in the N phase implies that sample 1 should have a larger orientational order imprinted into the elastomer network than samples 2 and 3. This can be considered equivalent to crosslinking the samples with a larger load, thereby producing a larger orientational order within the sample. Based on the results of the previous section, one might expect sample 3 to produce the largest ΔT_{eCE}, while sample 1 produces the smallest ΔT_{eCE}.

Figures 76 and 77 show the thermomechanical response of the cooling run and its derivative for all three samples [240,241]. Sample 3 shows the largest value of $|d\lambda/dT|$, thereby reinforcing the initial assumption that crosslinking deeper in the N phase is equivalent to crosslinking with a larger crosslinking load. The phase transition temperature T_C also decreases with increasing crosslinking temperature. This suggests that a larger orientational order imprinted into the sample during crosslinking makes the N phase more temperature stable, implying the existence of some internal ordering stress stabilizing the phase.

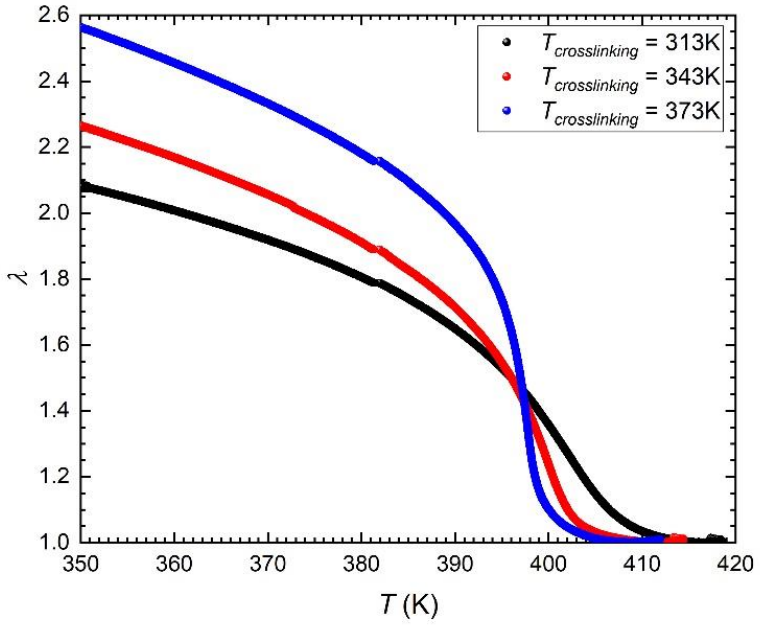

Figure 76: Thermomechanical response of the cooling run for samples crosslinked at three different temperatures [240,241].

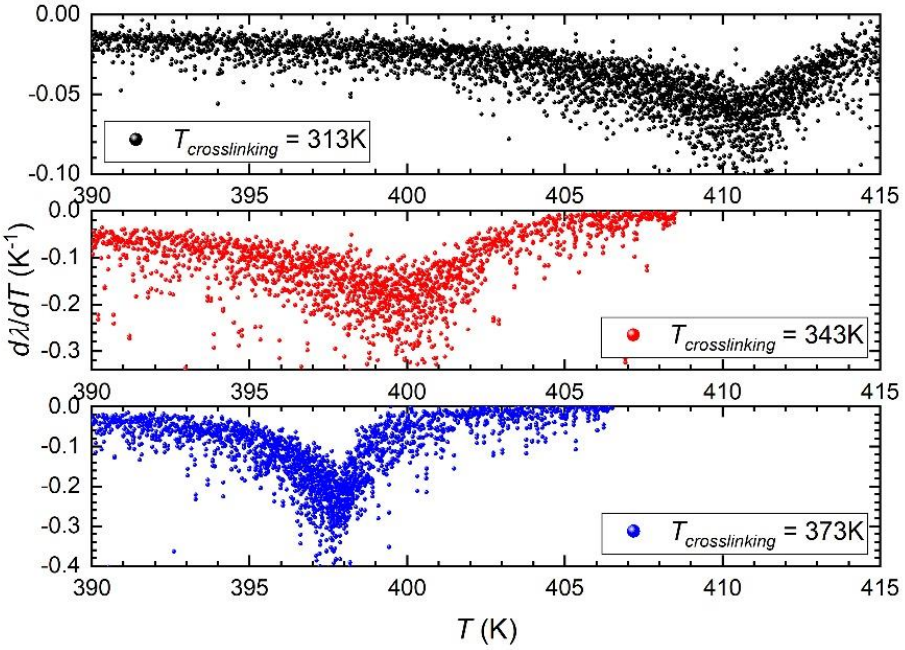

Figure 77: Derivative $d\lambda/dT$ of samples crosslinked at different temperatures. It is clearly seen that the value of $|d\lambda/dT|$ is the largest for sample 3 and the smallest for sample 1. Thus, a larger eC response is expected from 3. The temperature shift of the phase transition temperature towards lower temperatures is also observed [240,241].

Figures 78 and 79 show the eC response ΔT_{eCE} as a function of relative length change $\Delta l/l$ and applied stress $\Delta\sigma$, while Figure 80 shows the eC responsivity $\Delta T_{eCE}/\Delta\sigma$ as a function of applied stress $\Delta\sigma$ [240,241]. In terms of relative length changes, the largest eC response ΔT_{eCE} is achieved by sample 1. However, these results do not account for the work required to achieve these temperature changes. When the results are presented in terms of the applied uniaxial stress $\Delta\sigma$, the largest ΔT_{eCE} is achieved by sample 3, as expected, while samples 1 and 2 show a very similar trend. The curves for eC responsivity of samples 1 and 2 also coincide while lying below the curve of sample 3.

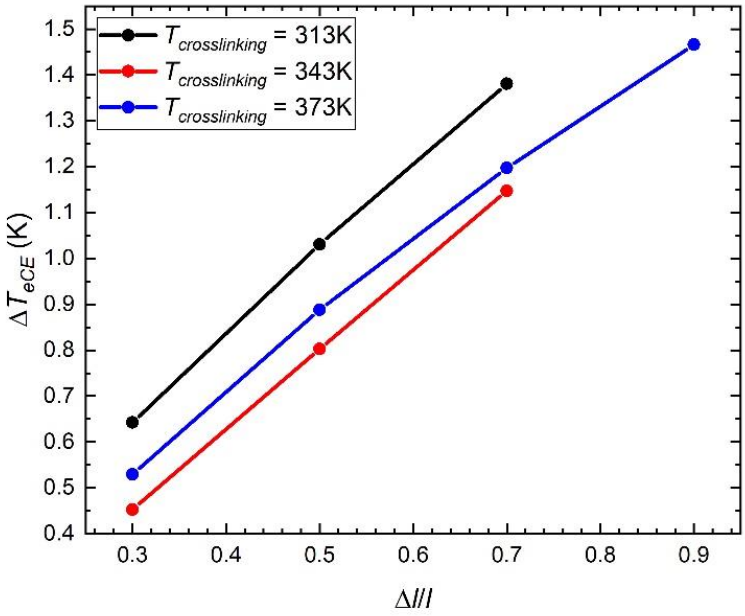

Figure 78: Measurement results of the eC response ΔT_{eCE} as a function of relative extension $\Delta l/l$ for samples crosslinked at different temperatures [240,241].

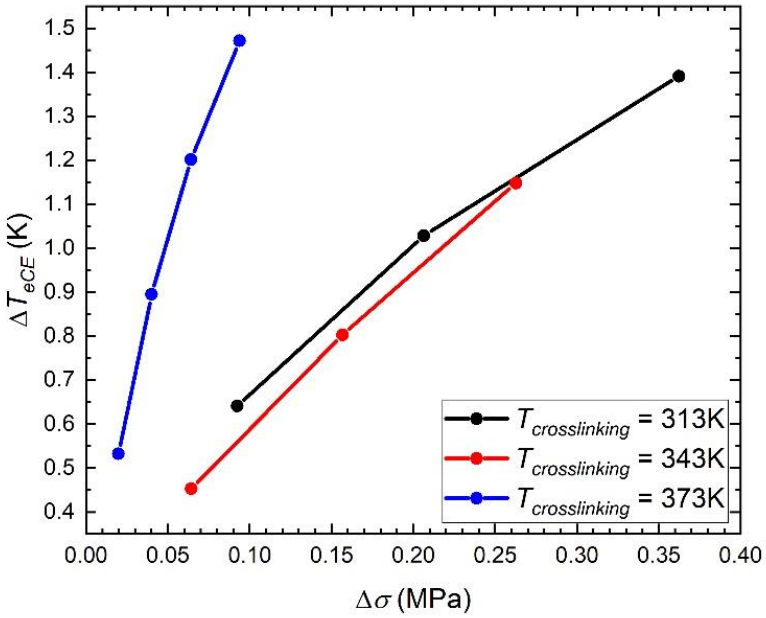

Figure 79: Measurement results of the eC response ΔT_{eCE} as a function of applied uniaxial stress $\Delta\sigma$ for samples crosslinked at different temperatures [240,241].

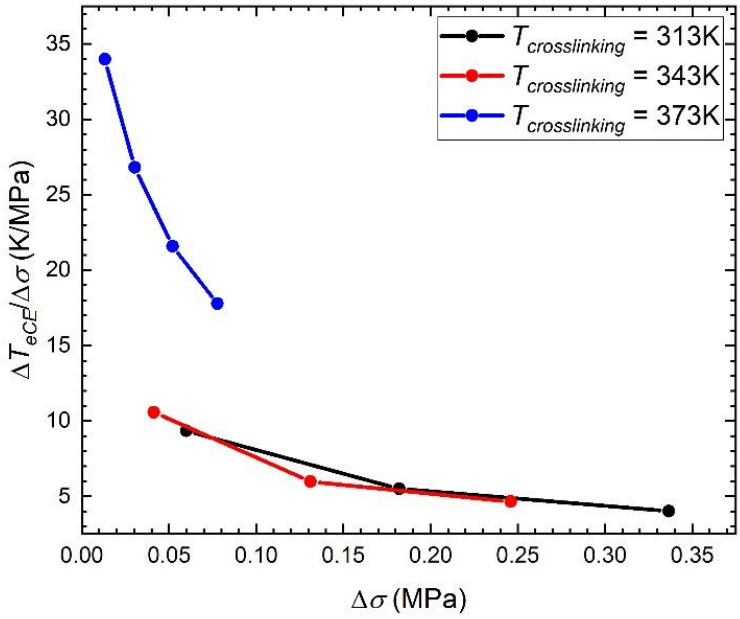

Figure 80: The eC responsivity $\Delta T_{eCE}/\Delta\sigma$ as a function applied stress $\Delta\sigma$ for samples crosslinked at different temperatures [240,241].

These results confirm our initial reasoning that crosslinking deeper in the N phase is equivalent to crosslinking the samples with a larger mass. The thermomechanical response shows a more continuous transition, which produces a smaller eC temperature change based on the simulations results and shifts the phase transition temperature towards higher values. The similar responses of samples 1 and 2 seem also to suggest, that a critical temperature exists where crosslinking samples below this temperature no longer produces any meaningful changes in the eC behavior of the samples. Due to the nature of the synthesis process, no samples crosslinked in the I phase were produced [240,241].

3.9.7 Thermomechanical and elastocaloric effect measurement results of main-chain liquid crystalline elastomers swelled with liquid crystal mesogens

Finally, we shall look at the eC response of MC-LCE swelled with the same mesogens used in synthesizing elastomers. Using the same mesogens ensures good mixing with the mesogens within the MC-LCE so that the nematic ordering is preserved. We prepared four samples: sample 1 was not swelled, sample 2 had the same amount of mesogens used in the swelling of the elastomers as were used in the synthesis of the elastomer ($m_{LC}/m_{LCE} \sim 1.0$), sample 3 had half of the amount of mesogens ($m_{LC}/m_{LCE} \sim 0.5$), and sample 4 had twice the amount of mesogens ($m_{LC}/m_{LCE} \sim 2.0$). Here, m_{LC} stands for the mass of the mesogens used in the swelling of the MC-LCE samples, while m_{LCE} stands for the mass of mesogens used in the synthesis process of the MC-LCE samples. In these cases, we have additional material indirectly being ordered through intramolecular interactions. From this, it follows that since we have more calorically active material, there should be an increase in the eC response of the swelled samples. On the other hand, there is extra material that is thermodynamically stable and resistant to any changes induced by external forces. This might require us to use larger stresses to achieve a larger eC

response. However, this concern might be redundant since we are dealing with LC, which requires negligible energy to change the ordering.

The thermomechanical response and its derivative $d\lambda/dT$, presented in Figures 81 and 82, show that swelling MC-LCE with mesogens could increase their eC response [240,241]. However, while adding some mesogens could improve the eC response, adding any additional amount produces diminishing returns. It also demonstrates that the peak is shifted towards lower temperatures with an increasing amount of mesogens. This is in good agreement with calorimetric measurement results obtained by Lebar et al. [233], which show a shift in the c_p peak towards lower temperatures in the swollen sample. Their measurement results also indicate that swelling MC-LCE causes the phase transition to become less supercritical (sharper). This could lead us to conclude that swelling MC-LCE improves the eC response ΔT_{eCE}, since our simulation results demonstrate that a less supercritical transition will produce larger eC responses.

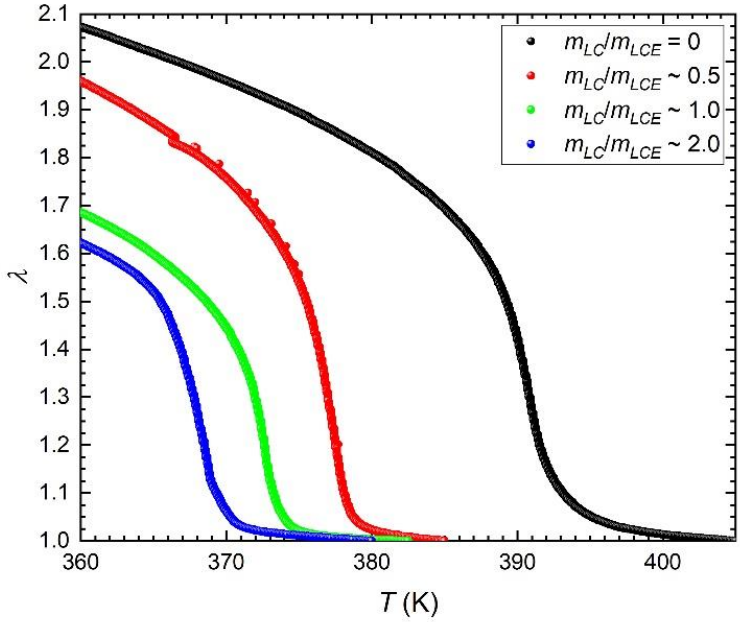

Figure 81: The thermomechanical response of MC-LCE samples swelled with mesogens with certain mass ratios m_{LC}/m_{LCE}. It is difficult to discern which sample has the largest thermomechanical response. The shift in T_C towards lower temperatures with increasing m_{LC}/m_{LCE} is observed [240,241].

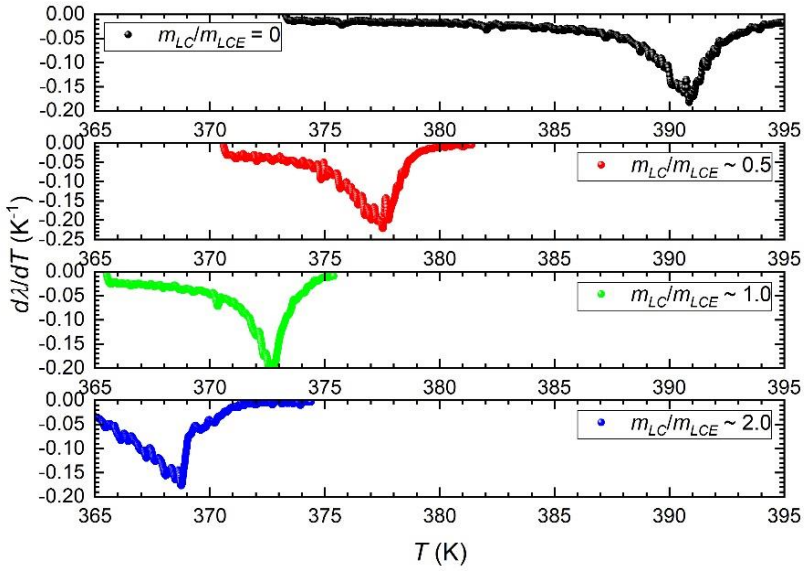

Figure 82: The derivative $d\lambda/dT$ of MC-LCE samples swelled with mesogens with certain mass ratios m_{LC}/m_{LCE}. It can be seen that swelling leads to an increase in the value of $|d\lambda/dT|$ for samples 2 and 3. It is expected that these two samples will display an increase in the eC response ΔT_{eCE} [240,241].

Figures 83 and 84 show the eC response ΔT_{eCE} as a function of temperature T and relative extension $\Delta l/l_0$ [240,241]. Increasing the number of mesogens decreases the temperature at which ΔT_{eCE} is the largest. This is in agreement with the thermomechanical response measurements. In terms of $\Delta l/l_0$, sample 1 displays the largest ΔT_{eCE}, while sample 4 displays the lowest ΔT_{eCE}.

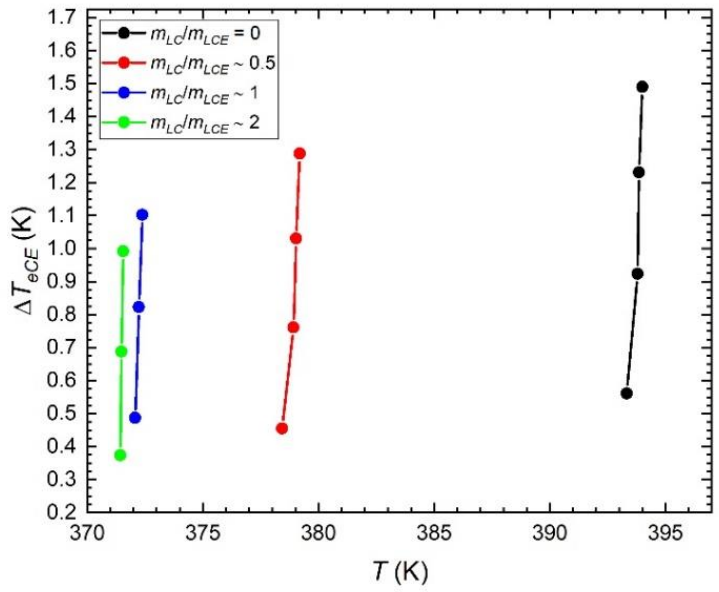

Figure 83: Measurement results of the eC response ΔT_{eCE} as a function of temperature T for MC-LCE samples swelled with mesogens with certain mass ratios m_{LC}/m_{LCE} [240,241].

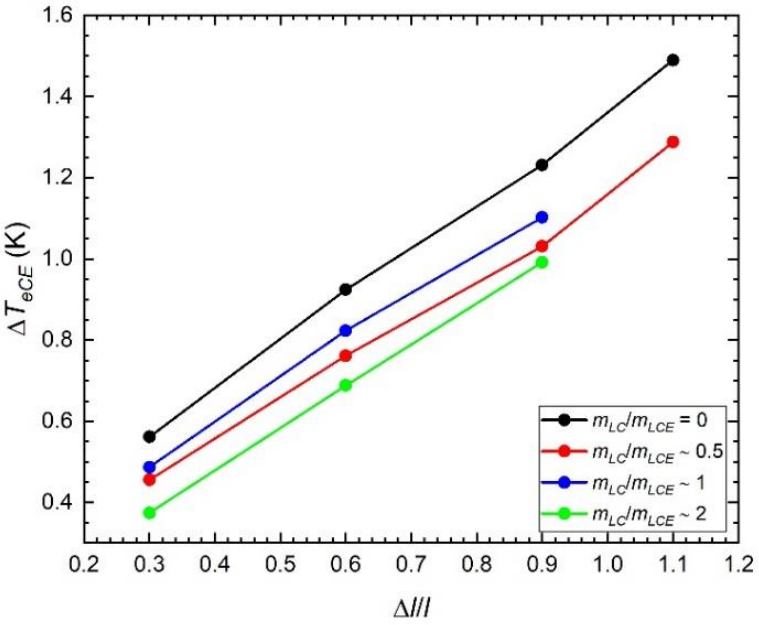

Figure 84: Measurement results of the eC response ΔT_{eCE} as a function of relative extension $\Delta l/l_0$ for MC-LCE samples swelled with mesogens with certain mass ratios m_{LC}/m_{LCE} [240,241].

Figures 85 and 86 show the eC response ΔT_{eCE} and eC responsivity $\Delta T_{eCE}/\Delta\sigma$ as a function of applied stress $\Delta\sigma$ [240,241]. Interestingly, sample 2, with $m_{LC}/m_{LCE} \sim 0.5$ stands out by exhibiting the largest ΔT_{eCE} as a function of $\Delta\sigma$, while the other samples show very similar responses. A possible explanation might be the competition between the induced order via stretching of the MC-LCE and the natural order of the surrounding LC. When we stretch the MC-LCE sample near the phase transition temperature, we order the mesogens incorporated within the polymer chains along the stretching axis. This ordering will influence the surrounding LC mesogens, which will want to remain more naturally disordered due to them being near the phase transition temperature. If the amount of free mesogens is small compared to the number of bounded mesogens, the external ordering will overpower the disordering tendency of the free mesogens. On the other hand, if the amount of free mesogens is similar or larger to the amount of bounded mesogens, then their resistance towards ordering might not be so easily overcome. This would lead to a smaller entropy change and, thus, to a smaller eC response. Also, this would explain why an increasing amount of free mesogens decreases the phase transition temperature since the LC ordering is being dictated more and more by the free mesogens than the bounded ones. Similarly, when it comes to $\Delta T_{eCE}/\Delta\sigma$, sample 2 shows the largest $\Delta T_{eCE}/\Delta\sigma$. At low-stress $\Delta\sigma$, the swelled samples show larger eC responsivity than sample 1. However, at intermediate levels, sample 1 at least outperforms sample 3, while for sample 4 we do not have enough data points due to the sample tearing during the measurement.

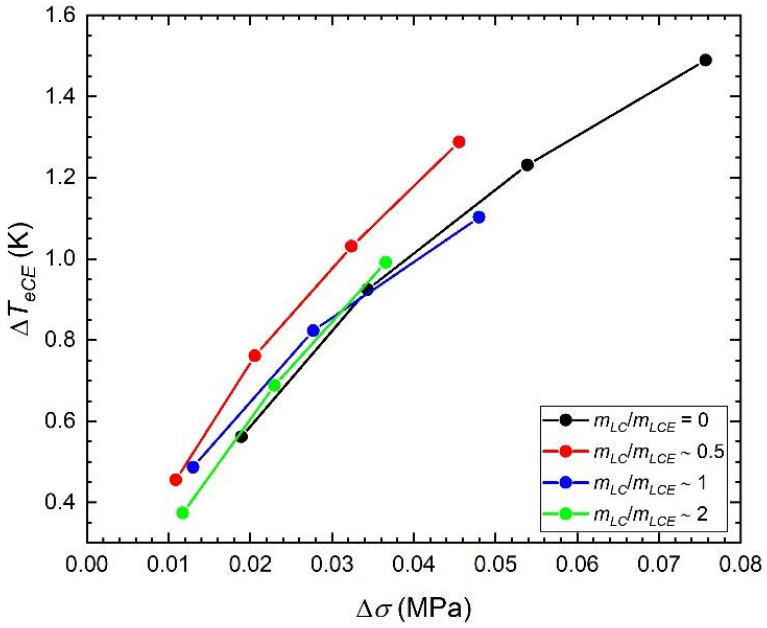

Figure 85: Measurement results of the eC response ΔT_{eCE} as a function of applied uniaxial stress $\Delta\sigma$ for MC-LCE samples swelled with mesogens with certain mass ratios m_{LC}/m_{LCE} [240,241].

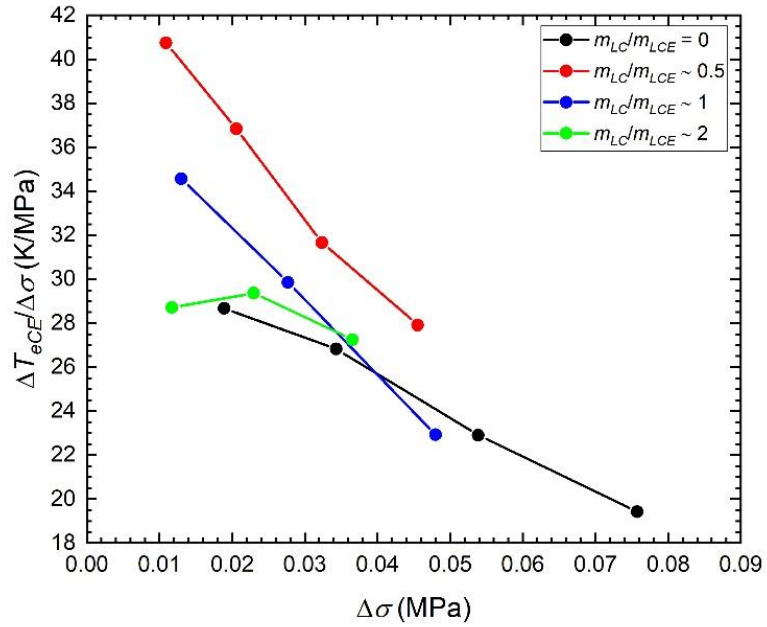

Figure 86: The eC responsivity $\Delta T_{eCE}/\Delta\sigma$ as a function applied stress $\Delta\sigma$ for MC-LCE samples swelled with mesogens with certain mass ratios m_{LC}/m_{LCE} [240,241].

These results indicate that partial swelling can improve the eC response, but they also suggest that the ratio m_{LC}/m_{LCE} has to lie between 1 and 0. Determining what the ideal

value is would require further investigation. Another question remains whether the free mesogens are eventually ejected from the elastomer, thereby reducing the long-term effectiveness of these samples. During the swelling process, some of the free mesogens were ejected from the elastomer. The larger was the number of swelling mesogens, the larger the ejected amount. Thus, it is assumed that at least some of the free mesogens will be ejected from the samples.

Chapter 4

Conclusion

The first part of this dissertation focused on the impact NPs can have on a surrounding LC matrix. This can be either destructive or constructive in nature. First, we looked at the experimental results of LC-NP mixtures, indicating a decrease in the nematic orientational order parameter as the concentration of NPs increased. Our focus was to create a minimalistic mathematical model that would be able to describe the observed behavior qualitatively. Next, the AC calorimetry measurements of LC mixtures with surface-functionalized Au NPs were performed. This study aimed to observe whether such NPs can thermodynamically stabilize TGB_A phases via the ADCT mechanism. By partially filling the energetically expensive TD core volume with the volume of the trapped NPs, this would lead towards a more energetically stable system.

The experiment in question demonstrated that at low concentration values of NPs, the orientational order parameter decreases only slightly. Upon reaching a certain critical concentration, the orientational order parameter decreases rapidly until it reaches a certain non-zero value, after which any additional NPs no longer have any effect. A simple mean-field-type expression at temperature $T = 0$ K for the nematic response in a randomly perturbed N phase was derived. A modified Lebwohl-Lasher-type lattice modelling was utilized, which, despite its simplicity, describes the general properties of nematic ordering well. In the experimental setup homogeneously dispersed NPs enforce a relatively weak disorder. In the model, it was assumed that NPs act as a kind of local random field, enforcing a different orientation at each point in the lattice. An increasing NP concentration was modeled as an increase in the random field strength. For the orientational distribution of the random field, the decision was made to use two distributions: a constant distribution and a Gaussian distribution. Numerically solving the self-consistent equation for the nematic orientational order parameter for both types of distributions demonstrated that the mathematical model described the qualitative behavior of the experimental results well. It also showed that the model is very robust regarding the choice of the distribution function since the solutions in both cases are very similar. Such a model could be potentially used in predicting the behavior of LC-NP mixtures.

It has been demonstrated previously that surface-functionalized NPs could thermodynamically stabilize certain LC phases containing TDs, such as blue and TGB_A phases when not previously present in a pure LC. This was achieved via the DCT or ADCT mechanisms. If an NP is surface-functionalized with an appropriate coating, it will be able to interact with the surrounding LC matrix. This can lead to the NPs filling the volume of the energetically expensive TD cores, thereby stabilizing such a defect structure. Our experiments aimed to determine how surface-functionalized NPs affect the thermodynamic stability of LC phases containing TDs that are already thermodynamically stable by

themselves. Specifically, how do Au NPs coated with OA impact the thermodynamic stability of the TGB_A and N_L^* phases present in three sets of LCs: $9FBTFO_1M_7$, $10FBTFO_1M_7$, and $11FBTFO_1M_7$. By performing AC calorimetry measurements on samples with various mass concentrations of NPs, it was determined that the combined temperature range of the TGB_A and N_L^* phases does increase. The comparison of the results for the three sets also showed that the presence of NPs impacted certain LC phases more than others. Specifically, the temperature range of the SmA phase noticeably shrinks while the temperature range of the SmC^* phase increases. This is most evident in $10FBTFO_1M_7$, where an increasing concentration of NPs appears to shrink the temperature range of the SmA phase, which lies in between the TGB_A and SmC^* phases, moving towards a TGB_A - SmA - SmC^* triple point. Interestingly, in $11FBTFO_1M_7$, the NPs appear to have a similar stabilizing effect on both TGB_A and SmC^* phases. This can be concluded from the fact that the increase in the combined temperature range of TGB_A and N_L^* is relatively small, $\Delta T_{TGB_A+N_L^*}(\chi = 0.01) \sim 0.2$ K. These examples show that the ADCT mechanism has a significant impact on stabilizing structures with TDs.

The second part of this dissertation was focused on caloric effects in condensed matter. More specifically, the ECE in lead-free doped BT and the eCE in LCEs are investigated. The goal of this research was to determine how certain chemical and physical parameters during the synthesis process impact the size of the temperature change of these materials.

The chemical parameters altered in BT were the concentration of Ba and Ti, where part of them are substituted by other appropriate elements, such as Ca, Zr, Sn, and Sr. We had BCT, BCZT, BSTS-0 (BST), BSTS-5, and BSTS-10 at our disposal. Specifically, we compared BCT and BCZT, studying the impact Zr has when added to a pure BCT, and compared BST with BSTS-5 and BSTS-10, studying the impact of Sn when added to a pure BST. Dielectric measurements showed that the addition of Zr did enhance the electric properties of BCT. Performing EC measurements in the vicinity of the phase transition, it is quite evident that the addition of Zr enhanced the ECE in BCT, the temperature changes being $\Delta T_{ECE} = 0.474$ K and $\Delta T_{ECE} = 0.668$ K at an applied electric field of $E = 14$ kV/cm for BCT and BCZT, respectively. Interestingly, the presence of Zr did not alter the phase transition temperature T_C. Dielectric measurements showed an increase in the electric properties in both BSTS-5 and BSTS-10, with BSTS-10 showing a larger increase in the dielectric constant. It is also seen that T_C decreases as the concentration of Sn increases from around 367 K for BST to 334 K for BSTS-5 and 298 K for BSTS-10. On the other hand, the EC measurements showed a decrease in the temperature change as the concentration of Sn is increased, as well as a broadening of the peak in the vicinity of the phase transition temperature, which is consistent with the diffuse phase transition behavior of BSTS ceramics.

In the case of LCEs, the chemical and physical parameters altered were the crosslinker concentration, stretching the LCEs with varying loads during the second crosslinking process, crosslinking at different temperatures during the second crosslinking process, and doping the LCEs with the same LCs used in the synthesis of said LCEs. An initial predictive study of LCEs was performed by solving the Landau free energy expression for an LCE experiencing uniaxial stress with an additional disordering term expressing the impact of crosslinkers. The varying parameters were the strength of both externally applied and internally present uniaxial stress and the disorder strength. It is shown that any increase in the internal stress experienced by the LCEs causes the first-order phase transition to become second-order. Increasing the disorder strength causes a non-zero nematic order to remain present at higher temperatures. The thermomechanical response shows that increasing internal stress shifts the phase transition towards higher temperatures while increasing both the internal stress and the disorder strength decreases

its absolute value. These results suggest that LCEs with a lower crosslinker concentration and with lower internal stress will produce larger temperature changes, which was confirmed by performing numerical calculations of such systems. Increasing the applied external stress produces a larger temperature change, shifting the phase transition temperature towards higher values.

AC calorimetry measurements on LCE samples with varying crosslinker concentrations was performed in order to determine the type of phase transition present. Results show that the $\chi = 0.05$ sample is weakly first-order with a negligible amount of latent heat detected. The $\chi = 0.06$ sample showed the largest c_p peak, but no latent heat is present. In the other samples ($\chi \geq 0.07$) the c_p peak decreases and broadens, indicating a second-order phase transition. Combining these results with the numerical simulations, we would expect the $\chi = 0.06$ sample to have the largest eC response. Measurements of the eC response at small values of applied stress confirmed our expectations. However, at moderate stress values, the $\chi = 0.06$ sample's eC response began to fall off compared to the other samples, which followed a trend in agreement with the numerical simulations. Possible damage to the sample during measurement was excluded by performing the same measurement on another $\chi = 0.06$ sample from the same batch as the initial sample. One explanation could be that an error occurred during the synthesis process. However, according to the specific heat measurements, the sample lies very much near the line of critical points and another explanation is possible. The application of a large enough σ to the sample at the critical point causes it to immediately pass into the supercritical regime, which is reflected as a sudden drop in $\Delta T_{eCE}/\Delta\sigma$. Using the phenomenological model for MC-LCEs, a region is formed in the $d - h - r$ phase diagram, where the phase transition is first-order. One also obtains a set of critical points (r_{CP}, h_{CP}, d_{CP}) that form a line of critical points that separates the phase transition between first-order and supercritical regime. The responsivity $\Delta r/\Delta h$ calculated in the vicinity of the critical points around $h \sim 0.0$ and $d \sim 0.00175$ showed an initial increase in $\Delta r/\Delta h$ with increased d, followed by a sharp drop. Comparison of these results with the experimentally obtained values for $\Delta T_{eCE}/\Delta\sigma$ as a function of σ, in which a similar drop is observed for the $\Delta T_{eCE}/\Delta\sigma$ for the near-critical $\chi = 0.06$ sample, shows qualitatively well agreement. This suggests that the experimentally observed anomalous behavior of the $\chi = 0.06$ sample is actually a consequence of its proximity to the line of critical points. Similar effects were observed in single crystal $Pb(Mg_{1/3}Nb_{2/3})O_3$-$PbTiO_3$ (PMN-PT) ferroelectric relaxors, where a large enough electric field could drive a first-order transition to terminate on a line of critical points and become supercritical.

Crosslinking LCEs at a lower temperature has a similar effect as crosslinking with a larger mass. It imprints a larger nematic orientational order into the LCE. This implies that the change in the nematic orientational order, and consequently in the subsystem's entropy, will be smaller, leading to a smaller eC response. The experimental results confirm that when LCEs are crosslinked at a higher temperature and with a smaller load, they exhibit larger temperature changes during stretching. It would have been interesting to compare the eC response of LCEs crosslinked above and below the phase transition temperature. However, the solutions used in the synthesis process have a boiling point lower than the phase transition temperature of the LCE.

Doping the LCEs with the same LCs used in the synthesis process impacts the eC response, but only up to a certain point. Measurements of the eC response show that when the mass ratio between the doped LC mesogens and LC mesogens incorporated within the LCE, m_{LC}/m_{LCE}, is around 0.5, the LCEs show an improved response. Increasing m_{LC}/m_{LCE} toward 1.0, the LCEs display a similar response as a pure LCE. Beyond $m_{LC}/m_{LCE} \sim 1.0$, the eC response decreases. The conclusion is that doping can improve

the eC response in LCEs. To determine the optimal amount of doping would require us to increase incrementally m_{LC}/m_{LCE}, for example, by 0.1, and perform the eC measurements. Such research remains to be conducted.

In general, the conclusions reached from the eC measurements of variously engineered LCEs are that lower concentrations of crosslinkers, higher crosslinking loads, and higher temperatures during the second crosslinking process, as well as some doping with LC mesogens, will increase the eC response.

References

[1] P. Poulin, *Novel Colloidal Interactions in Anisotropic Fluids*, Science (80-.). **275**, 1770 (1997).

[2] P. Poulin and D. A. Weitz, *Inverted and Multiple Nematic Emulsions*, Phys. Rev. E **57**, 626 (1998).

[3] U. Tkalec, M. Ravnik, S. Čopar, S. Žumer, and I. Muševič, *Reconfigurable Knots and Links in Chiral Nematic Colloids*, Science (80-.). **333**, 62 (2011).

[4] I. Muševič, M. Škarabot, U. Tkalec, M. Ravnik, and S. Žumer, *Two-Dimensional Nematic Colloidal Crystals Self-Assembled by Topological Defects*, Science (80-.). **313**, 954 (2006).

[5] I. Muševič, *Interactions, Topology and Photonic Properties of Liquid Crystal Colloids and Dispersions*, Eur. Phys. J. Spec. Top. **227**, 2455 (2019).

[6] J. Brugués, J. Ignés-Mullol, J. Casademunt, and F. Sagués, *Probing Elastic Anisotropy from Defect Dynamics in Langmuir Monolayers*, Phys. Rev. Lett. **100**, 037801 (2008).

[7] U. Tkalec and I. Muševič, *Topology of Nematic Liquid Crystal Colloids Confined to Two Dimensions*, Soft Matter **9**, 8140 (2013).

[8] C. N. Weiler, T. W. Neely, D. R. Scherer, A. S. Bradley, M. J. Davis, and B. P. Anderson, *Spontaneous Vortices in the Formation of Bose–Einstein Condensates*, Nature **455**, 948 (2008).

[9] A. Polkovnikov, K. Sengupta, A. Silva, and M. Vengalattore, *Colloquium : Nonequilibrium Dynamics of Closed Interacting Quantum Systems*, Rev. Mod. Phys. **83**, 863 (2011).

[10] K. Kudo and Y. Kawaguchi, *Coarsening Dynamics Driven by Vortex-Antivortex Annihilation in Ferromagnetic Bose-Einstein Condensates*, Phys. Rev. A **91**, 053609 (2015).

[11] S. W. Seo, W. J. Kwon, S. Kang, and Y. Shin, *Collisional Dynamics of Half-Quantum Vortices in a Spinor Bose-Einstein Condensate*, Phys. Rev. Lett. **116**, 185301 (2016).

[12] V. M. H. Ruutu, V. B. Eltsov, A. J. Gill, T. W. B. Kibble, M. Krusius, Y. G. Makhlin, B. Plaçais, G. E. Volovik, and W. Xu, *Vortex Formation in Neutron-Irradiated Superfluid 3He as an Analogue of Cosmological Defect Formation*, Nature **382**, 334 (1996).

[13] C. Bäuerle, Y. M. Bunkov, S. N. Fisher, H. Godfrin, and G. R. Pickett, *Laboratory Simulation of Cosmic String Formation in the Early Universe Using Superfluid 3He*, Nature **382**, 332 (1996).

[14] A. Wachowiak, J. Wiebe, M. Bode, O. Pietzsch, M. Morgenstern, and R. Wiesendanger, *Direct Observation of Internal Spin Structure of Magnetic Vortex Cores*, Science (80-.). **298**, 577 (2002).

[15] R. Hertel and C. M. Schneider, *Exchange Explosions: Magnetization Dynamics*

during Vortex-Antivortex Annihilation, Phys. Rev. Lett. **97**, 177202 (2006).

[16] I. Rissanen and L. Laurson, *Coarsening Dynamics of Topological Defects in Thin Permalloy Films*, Phys. Rev. B **94**, 144428 (2016).

[17] R. Ray and A. M. Srivastava, *Measuring Cosmic Defect Correlations in Liquid Crystals*, Phys. Rev. D **69**, 103525 (2004).

[18] W. H. Zurek, *Cosmological Experiments in Condensed Matter Systems*, Phys. Rep. **276**, 177 (1996).

[19] I. Chuang, R. Durrer, N. Turok, and B. Yurke, *Cosmology in the Laboratory: Defect Dynamics in Liquid Crystals*, Science (80-.). **251**, 1336 (1991).

[20] I. Chuang, N. Turok, and B. Yurke, *Late-Time Coarsening Dynamics in a Nematic Liquid Crystal*, Phys. Rev. Lett. **66**, 2472 (1991).

[21] M. J. Bowick, L. Chandar, E. A. Schiff, and A. M. Srivastava, *The Cosmological Kibble Mechanism in the Laboratory: String Formation in Liquid Crystals*, Science (80-.). **263**, 943 (1994).

[22] H.-R. Trebin, *Defects in Liquid Crystals and Cosmology*, Liq. Cryst. **24**, 127 (1998).

[23] T. Kibble and A. Srivastava, *Condensed Matter Analogues of Cosmology*, J. Phys. Condens. Matter **25**, 400301 (2013).

[24] T. Araki, M. Buscaglia, T. Bellini, and H. Tanaka, *Memory and Topological Frustration in Nematic Liquid Crystals Confined in Porous Materials*, Nat. Mater. **10**, 303 (2011).

[25] J. D. Lee and A. C. Eringen, *Boundary Effects of Orientation of Nematic Liquid Crystals*, J. Chem. Phys. **55**, 4509 (1971).

[26] T. C. Lubensky, D. Pettey, N. Currier, and H. Stark, *Topological Defects and Interactions in Nematic Emulsions*, Phys. Rev. E **57**, 610 (1998).

[27] M. Yada, J. Yamamoto, and H. Yokoyama, *Direct Observation of Anisotropic Interparticle Forces in Nematic Colloids with Optical Tweezers*, Phys. Rev. Lett. **92**, 185501 (2004).

[28] M. Ravnik, G. P. Alexander, J. M. Yeomans, and S. Žumer, *Three-Dimensional Colloidal Crystals in Liquid Crystalline Blue Phases*, Proc. Natl. Acad. Sci. **108**, 5188 (2011).

[29] R. P. Trivedi, I. I. Klevets, B. Senyuk, T. Lee, and I. I. Smalyukh, *Reconfigurable Interactions and Three-Dimensional Patterning of Colloidal Particles and Defects in Lamellar Soft Media*, Proc. Natl. Acad. Sci. **109**, 4744 (2012).

[30] J. Dontabhaktuni, M. Ravnik, and S. Žumer, *Quasicrystalline Tilings with Nematic Colloidal Platelets*, Proc. Natl. Acad. Sci. **111**, 2464 (2014).

[31] I. Lelidis, M. Nobili, and G. Durand, *Electric-Field-Induced Change of the Order Parameter in a Nematic Liquid Crystal*, Phys. Rev. E **48**, 3818 (1993).

[32] V. Fréedericksz and A. Repiewa, *Theoretisches Und Experimentelles Zur Frage Nach Der Natur Der Anisotropen Flüssigkeiten*, Zeitschrift Für Phys. **42**, 532 (1927).

[33] J. Hanus, *Effect of the Molecular Interaction Between Anisotropic Molecules on the Optical Kerr Effect. Field-Induced Phase Transition*, Phys. Rev. **178**, 420 (1969).

[34] Y. Poggi and J. C. Filippini, *Magnetic-Field Dependence of the Order Parameter in a Nematic Single Crystal*, Phys. Rev. Lett. **39**, 150 (1977).

[35] A. J. Nicastro and P. H. Keyes, *Electric-Field-Induced Critical Phenomena at the Nematic-Isotropic Transition and the Nematic-Isotropic Critical Point*, Phys. Rev. A **30**, 3156 (1984).

[36] P. Pieranski and E. Guyon, *Instability of Certain Shear Flows in Nematic Liquids*, Phys. Rev. A **9**, 404 (1974).

[37] J. N. Baleo, M. Vincent, P. Navard, and Y. Demay, *Finite Element Simulation of Flow and Director Orientation of Viscous Anisotropic Fluids in Complex 2D Geometries*, J. Rheol. (N. Y. N. Y). **36**, 663 (1992).

[38] S. Chono and T. Suji, *Numerical Simulation of Nematic Liquid Crystalline Flows Around a Circular Cylinder*, Mol. Cryst. Liq. Cryst. Sci. Technol. Sect. A. Mol. Cryst. Liq. Cryst. **309**, 217 (1998).

[39] S. Chono, T. Tsuji, and M. M. Denn, *Spatial Development of Director Orientation of Tumbling Nematic Liquid Crystals in Pressure-Driven Channel Flow*, J. Nonnewton. Fluid Mech. **79**, 515 (1998).

[40] P. A. Cruz, M. F. Tomé, I. W. Stewart, and S. McKee, *Numerical Investigation of Director Orientation and Flow of Nematic Liquid Crystals in a Planar 1:4 Expansion*, J. Mech. Mater. Struct. **6**, 1017 (2011).

[41] P.-G. de Gennes and J. Prost, *The Physics of Liquid Crystals (International Series of Monographs on Physics)*, Oxford Univ. Press. USA (1995).

[42] L. M. Blinov, *Structure and Properties of Liquid Crystals* (Springer Netherlands, Dordrecht, 2011).

[43] O. D. Lavrentovich and M. Kleman, *Soft Matter Physics: An Introduction* (Springer New York, New York, NY, 2004).

[44] S. Kaur, S. P. Singh, A. M. Biradar, A. Choudhary, and K. Sreenivas, *Enhanced Electro-Optical Properties in Gold Nanoparticles Doped Ferroelectric Liquid Crystals*, Appl. Phys. Lett. **91**, 023120 (2007).

[45] T. Miyama, J. Thisayukta, H. Shiraki, Y. Sakai, Y. Shiraishi, N. Toshima, and S. Kobayashi, *Fast Switching of Frequency Modulation Twisted Nematic Liquid Crystal Display Fabricated by Doping Nanoparticles and Its Mechanism*, Jpn. J. Appl. Phys. **43**, 2580 (2004).

[46] H. Shiraki, S. Kundu, Y. Sakai, T. Masumi, Y. Shiraishi, N. Toshima, and S. Kobayashi, *Dielectric Properties of Frequency Modulation Twisted Nematic LCDs Doped with Palladium (Pd) Nanoparticles*, Jpn. J. Appl. Phys. **43**, 5425 (2004).

[47] Y. Shiraishi, N. Toshima, K. Maeda, H. Yoshikawa, J. Xu, and S. Kobayashi, *Frequency Modulation Response of a Liquid-Crystal Electro-Optic Device Doped with Nanoparticles*, Appl. Phys. Lett. **81**, 2845 (2002).

[48] S. Starzonek, S. J. Rzoska, A. Drozd-Rzoska, K. Czupryński, and S. Kralj, *Impact of Ferroelectric and Superparaelectric Nanoparticles on Phase Transitions and Dynamics in Nematic Liquid Crystals*, Phys. Rev. E **96**, 022705 (2017).

[49] S. J. Rzoska, S. Starzonek, A. Drozd-Rzoska, K. Czupryński, K. Chmiel, G. Gaura, A. Michulec, B. Szczypek, and W. Walas, *Impact of BaTiO3 Nanoparticles on Pretransitional Effects in Liquid Crystalline Dodecylcyanobiphenyl*, Phys. Rev. E **93**, 020701 (2016).

[50] M. Trček, Nanoparticle-Induced Twist Grain Boundary Phases and Electrocaloric

Effect in Liquid Crystals : PhD Thesis, [M. Trček], 2017.

[51] M. Lavrič, V. Tzitzios, S. Kralj, G. Cordoyiannis, I. Lelidis, G. Nounesis, V. Georgakilas, H. Amenitsch, A. Zidanšek, and Z. Kutnjak, *The Effect of Graphene on Liquid-Crystalline Blue Phases*, Appl. Phys. Lett. **103**, 143116 (2013).

[52] B. Rožič et al., *Theoretical and Experimental Study of the Nanoparticle-Driven Blue Phase Stabilisation*, Eur. Phys. J. E **34**, 17 (2011).

[53] G. Cordoyiannis, A. Lebar, B. Rožič, B. Zalar, Z. Kutnjak, S. Žumer, F. Brömmel, S. Krause, and H. Finkelmann, *Controlling the Critical Behavior of Paranematic to Nematic Transition in Main-Chain Liquid Single-Crystal Elastomers*, Macromolecules **42**, 2069 (2009).

[54] D. Coursault, J. Grand, B. Zappone, H. Ayeb, G. Lévi, N. Félidj, and E. Lacaze, *Linear Self-Assembly of Nanoparticles Within Liquid Crystal Defect Arrays*, Adv. Mater. **24**, 1461 (2012).

[55] M. Škarabot, M. Ravnik, S. Žumer, U. Tkalec, I. Poberaj, D. Babič, and I. Muševič, *Hierarchical Self-Assembly of Nematic Colloidal Superstructures*, Phys. Rev. E **77**, 061706 (2008).

[56] V. G. Nazarenko, A. B. Nych, and B. I. Lev, *Crystal Structure in Nematic Emulsion*, Phys. Rev. Lett. **87**, 075504 (2001).

[57] I. I. Smalyukh, S. Chernyshuk, B. I. Lev, A. B. Nych, U. Ognysta, V. G. Nazarenko, and O. D. Lavrentovich, *Ordered Droplet Structures at the Liquid Crystal Surface and Elastic-Capillary Colloidal Interactions*, Phys. Rev. Lett. **93**, 117801 (2004).

[58] R. Repnik, V. P. Nita, and S. Kralj, *Mixtures of Nanoparticles and Liquid Crystal Phases Exhibiting Topological Defects*, Mol. Cryst. Liq. Cryst. **560**, 115 (2012).

[59] G. Cordoyiannis et al., *Different Modulated Structures of Topological Defects Stabilized by Adaptive Targeting Nanoparticles*, Soft Matter **9**, 3956 (2013).

[60] M. Warner and E. M. Terentjev, *Liquid Crystal Elastomers*, Revised (Oxford Sciences Publications, New York, NY, 2003).

[61] D. K. Shenoy, D. Laurence Thomsen III, A. Srinivasan, P. Keller, and B. R. Ratna, *Carbon Coated Liquid Crystal Elastomer Film for Artificial Muscle Applications*, Sensors Actuators A Phys. **96**, 184 (2002).

[62] M. Hébert, R. Kant, and P.-G. de Gennes, *Dynamics and Thermodynamics of Artificial Muscles Based on Nematic Gels*, J. Phys. I **7**, 909 (1997).

[63] A. Sánchez-Ferrer, T. Fischl, M. Stubenrauch, H. Wurmus, M. Hoffmann, and H. Finkelmann, *Photo-Crosslinked Side-Chain Liquid-Crystalline Elastomers for Microsystems*, Macromol. Chem. Phys. **210**, 1671 (2009).

[64] P. Palffy-Muhoray, *Printed Actuators in a Flap*, Nat. Mater. **8**, 614 (2009).

[65] M. Camacho-Lopez, H. Finkelmann, P. Palffy-Muhoray, and M. Shelley, *Fast Liquid-Crystal Elastomer Swims into the Dark*, Nat. Mater. **3**, 307 (2004).

[66] M. Chambers, B. Zalar, M. Remškar, S. Žumer, and H. Finkelmann, *Actuation of Liquid Crystal Elastomers Reprocessed with Carbon Nanoparticles*, Appl. Phys. Lett. **89**, 243116 (2006).

[67] C. L. van Oosten, C. W. M. Bastiaansen, and D. J. Broer, *Printed Artificial Cilia from Liquid-Crystal Network Actuators Modularly Driven by Light*, Nat. Mater. **8**, 677 (2009).

[68] M. Devetak, B. Zupančič, A. Lebar, P. Umek, B. Zalar, V. Domenici, G. Ambrožič, M. Žigon, M. Čopič, and I. Drevenšek-Olenik, *Micropatterning of Light-Sensitive Liquid-Crystal Elastomers*, Phys. Rev. E **80**, 050701 (2009).

[69] W. H. de Jeu, editor , *Liquid Crystal Elastomers: Materials and Applications*, Vol. 250 (Springer Berlin Heidelberg, Berlin, Heidelberg, 2012).

[70] A. K. Bain and P. Chand, *Ferroelectrics: Principles and Applications*, 1st editio (Wiley-VCH, 2017).

[71] P. G. de Gennes, *An Analogy between Superconductors and Smectics A*, Solid State Commun. **10**, 753 (1972).

[72] S. R. Renn and T. C. Lubensky, *Abrikosov Dislocation Lattice in a Model of the Cholesteric – to – Smectic- A Transition*, Phys. Rev. A **38**, 2132 (1988).

[73] C. C. Huang, D. S. Lin, J. W. Goodby, M. A. Waugh, S. M. Stein, and E. Chin, *Calorimetric and Optical Microscopic Studies on One Ferroelectric Liquid-Crystal Compound with the Smectic-A Phase*, Phys. Rev. A **40**, 4153 (1989).

[74] J. W. Goodby, M. A. Waugh, S. M. Stein, E. Chin, R. Pindak, and J. S. Patel, *Characterization of a New Helical Smectic Liquid Crystal*, Nature **337**, 449 (1989).

[75] T. C. Lubensky and S. R. Renn, *Twist-Grain-Boundary Phases near the Nematic–Smectic- A –Smectic- C Point in Liquid Crystals*, Phys. Rev. A **41**, 4392 (1990).

[76] F. C. Frank, *I. Liquid Crystals. On the Theory of Liquid Crystals*, Discuss. Faraday Soc. **25**, 19 (1958).

[77] A. Rapini and M. Papoular, *Distorsion d'une Lamelle Nematique Sous Champ Magnetique Conditions d'ancrage Aux Parois*, Le J. Phys. Colloq. **30**, C4 (1969).

[78] T. Jin and D. Finotello, *Aerosil Dispersed in a Liquid Crystal: Magnetic Order and Random Silica Disorder*, Phys. Rev. Lett. **86**, 818 (2001).

[79] C. W. Garland, *Calorimetric Studies*, in *Liquid Crystals: Experimental Study of Physical Properties and Phase Transitions*, edited by S. Kumar (Cambridge University Press, 2001), pp. 240–294.

[80] J. Thoen, G. Cordoyiannis, and C. Glorieux, *Investigations of Phase Transitions in Liquid Crystals by Means of Adiabatic Scanning Calorimetry*, Liq. Cryst. **36**, 669 (2009).

[81] H. Yao, K. Ema, and C. W. Garland, *Nonadiabatic Scanning Calorimeter*, Rev. Sci. Instrum. **69**, 172 (1998).

[82] M. A. Anisimov, *Critical Phenomena in Liquid and Liquid Crystals* (CRC Press, 1991).

[83] J. Thoen, *Thermal Investigations of Phase Transitions in Thermotropic Liquid Crystals*, Int. J. Mod. Phys. B **09**, 2157 (1995).

[84] Y. A. Kraftmakher, *AC Calorimetry*, Zhurnal Prikl. Mekhaniki i Tekhnicheskoi Fiz. **5**, (1962).

[85] K. Ema, T. Uematsu, A. Sugata, and H. Yao, *Complex Calorimeter with AC- and Relaxation-Mode Operation*, Jpn. J. Appl. Phys. **32**, 1846 (1993).

[86] K. Ema, H. Yao, I. Kawamura, T. Chan, and C. W. Garland, *High-Resolution Calorimetric Study of the Antiferroelectric Liquid Crystals Methylheptyloxycarbonylphenyl Octyloxybiphenyl Carboxylate and Its Octylcarbonylbiphenyl Analog*, Phys. Rev. E **47**, 1203 (1993).

[87] D. Djurek, J. Baturić-Rubčić, and K. Franulović, *Specific-Heat Critical Exponents near the Nematic—Smectic-A Phase Transition*, Phys. Rev. Lett. **33**, 1126 (1974).

[88] E. Karatairi, B. Rožič, Z. Kutnjak, V. Tzitzios, G. Nounesis, G. Cordoyiannis, J. Thoen, C. Glorieux, and S. Kralj, *Nanoparticle-Induced Widening of the Temperature Range of Liquid-Crystalline Blue Phases*, Phys. Rev. E **81**, 041703 (2010).

[89] M. Trček, G. Cordoyiannis, V. Tzitzios, S. Kralj, G. Nounesis, I. Lelidis, and Z. Kutnjak, *Nanoparticle-Induced Twist-Grain Boundary Phase*, Phys. Rev. E **90**, 032501 (2014).

[90] H. Haga and C. Garland, *Effect of Silica Aerosil Particles on Liquid-Crystal Phase Transitions*, Phys. Rev. E **56**, 3044 (1997).

[91] Z. Kutnjak, S. Kralj, and S. Žumer, *Effect of Dispersed Silica Particles on the Smectic- A –Smectic- C * Phase Transition*, Phys. Rev. E **66**, 041702 (2002).

[92] G. Cordoyiannis et al., *Blue Phase III Widening in CE6-Dispersed Surface-Functionalised CdSe Nanoparticles*, Liq. Cryst. **37**, 1419 (2010).

[93] C. Kyrou, S. Kralj, M. Panagopoulou, Y. Raptis, G. Nounesis, and I. Lelidis, *Impact of Spherical Nanoparticles on Nematic Order Parameters*, Phys. Rev. E **97**, 042701 (2018).

[94] P. A. Lebwohl and G. Lasher, *Nematic-Liquid-Crystal Order—A Monte Carlo Calculation*, Phys. Rev. A **6**, 426 (1972).

[95] S. Buček, S. Kralj, and T. J. Sluckin, *Hysteresis in Two-Dimensional Liquid Crystal Models*, Adv. Condens. Matter Phys. **2015**, 1 (2015).

[96] G. R. Luckhurst, T. J. Sluckin, and H. B. Zewdie, *Computer Simulation Studies of Anisotropic Systems*, Mol. Phys. **59**, 657 (1986).

[97] D. J. Cleaver, S. Kralj, T. J. Sluckin, and M. P. Allen, *The Random Anisotropy Nematic Spin Model*, in *Liquid Crystals In Complex Geometries: Formed by Polymer And Porous Networks*, edited by G. P. Crawford and S. Žumer (Taylor and Francis, 1996), pp. 467–481.

[98] H. Kikuchi, M. Yokota, Y. Hisakado, H. Yang, and T. Kajiyama, *Polymer-Stabilized Liquid Crystal Blue Phases*, Nat. Mater. **1**, 64 (2002).

[99] L. Wang, W. He, X. Xiao, F. Meng, Y. Zhang, P. Yang, L. Wang, J. Xiao, H. Yang, and Y. Lu, *Hysteresis-Free Blue Phase Liquid-Crystal-Stabilized by ZnS Nanoparticles*, Small **8**, 2189 (2012).

[100] A. Gudimalla, M. Lavrič, M. Trček, S. Harkai, B. Rožič, G. Cordoyiannis, S. Thomas, K. Pal, Z. Kutnjak, and S. Kralj, *Nanoparticle-Stabilized Lattices of Topological Defects in Liquid Crystals*, Int. J. Thermophys. **41**, 51 (2020).

[101] N. Schopohl and T. J. Sluckin, *Defect Core Structure in Nematic Liquid Crystals*, Phys. Rev. Lett. **59**, 2582 (1987).

[102] S. Kralj and T. J. Sluckin, *Landau-de Gennes Theory of the Core Structure of a Screw Dislocation in Smectic A Liquid Crystals*, Liq. Cryst. **18**, 887 (1995).

[103] M. Ambrožič, S. Kralj, T. J. Sluckin, S. Žumer, and D. Svenšek, *Annihilation of Edge Dislocations in Smectic-A Liquid Crystals*, Phys. Rev. E **70**, 051704 (2004).

[104] G. Cordoyiannis, M. Lavrič, V. Tzitzios, M. Trček, I. Lelidis, G. Nounesis, S. Kralj, J. Thoen, and Z. Kutnjak, *Experimental Advances in Nanoparticle-Driven*

Stabilization of Liquid-Crystalline Blue Phases and Twist-Grain Boundary Phases, Nanomaterials **11**, 2968 (2021).

[105] A. Bouchta, H. T. Nguyen, M. F. Achard, F. Hardouin, C. Destrade, R. J. Twieg, A. Maaroufi, and N. Isaert, *New TGB A Series Exhibiting a SC *SASA*N* Phase Sequence*, Liq. Cryst. **12**, 575 (1992).

[106] M. Trček, G. Cordoyiannis, Z. Kutnjak, G. Nounesis, and I. Lelidis, *Twist-Grain-Boundary-A* Phase Stabilisation in Confined Geometry by the Interfaces*, Liq. Cryst. **43**, 1437 (2016).

[107] T. Chan, C. W. Garland, and H. T. Nguyen, *Calorimetric Study of Chiral Liquid Crystals with a Twist-Grain-Boundary Phase*, Phys. Rev. E **52**, 5000 (1995).

[108] I. Dierking, *Textures of Liquid Crystals* (Wiley, 2003).

[109] I. Dierking, F. Gieβelmann, P. Zugenmaier, W. Kuczynskit, S. T. Lagerwall, and B. Stebler, *Investigations of the Structure of a Cholesteric Phase with a Temperature Induced Helix Inversion and of the Succeeding Sc∗ Phase in Thin Liquid Crystal Cells*, Liq. Cryst. **13**, 45 (1993).

[110] A. Thanassoulas, E. Karatairi, G. Cordoyiannis, Z. Kutnjak, V. Tzitzios, I. Lelidis, and G. Nounesis, *CdSe Nanoparticles Dispersed in Ferroelectric Smectic Liquid Crystals: Effects upon the Smectic Order and the Smectic-A to Chiral Smectic-C Phase Transition*, Phys. Rev. E **88**, 032504 (2013).

[111] G. Cordoyiannis, S. Kralj, G. Nounesis, Z. Kutnjak, and S. Žumer, *Pretransitional Effects near the Smectic- A –Smectic- C* Phase Transition of Hydrophilic and Hydrophobic Aerosil Networks Dispersed in Ferroelectric*, Phys. Rev. E **75**, 021702 (2007).

[112] H. Grebel, R. M. Hornreich, and S. Shtrikman, *Landau Theory of Cholesteric Blue Phases: The Role of Higher Harmonics*, Phys. Rev. A **30**, 3264 (1984).

[113] J. V. Selinger, *Interpretation of Saddle-Splay and the Oseen-Frank Free Energy in Liquid Crystals*, Liq. Cryst. Rev. **6**, 129 (2018).

[114] S. Meiboom, J. P. Sethna, P. W. Anderson, and W. F. Brinkman, *Theory of the Blue Phase of Cholesteric Liquid Crystals*, Phys. Rev. Lett. **46**, 1216 (1981).

[115] S. Kralj and T. J. Sluckin, *Core Structure of a Screw Disclination in Smectic- A Liquid Crystals*, Phys. Rev. E **48**, R3244 (1993).

[116] B. Jaffe, R. S. Roth, and S. Marzullo, *Piezoelectric Properties of Lead Zirconate-Lead Titanate Solid-Solution Ceramics*, J. Appl. Phys. **25**, 809 (1954).

[117] Y. Y. Yohachi Yamashita, *Large Electromechanical Coupling Factors in Perovskite Binary Material System*, Jpn. J. Appl. Phys. **33**, 5328 (1994).

[118] T. Yamamoto and S. O. Satoru Ohashi, *Dielectric and Piezoelectric Properties of Pb(Yb 1/2 Nb 1/2)O 3 -PbTiO 3 Solid Solution System*, Jpn. J. Appl. Phys. **34**, 5349 (1995).

[119] W. Cao and L. E. Cross, *Theoretical Model for the Morphotropic Phase Boundary in Lead Zirconate–Lead Titanate Solid Solution*, Phys. Rev. B **47**, 4825 (1993).

[120] A. Amin, R. E. Newnham, and L. E. Cross, *Effect of Elastic Boundary Conditions on Morphotropic Pb(Zr,Ti)O3 Piezoelectrics*, Phys. Rev. B **34**, 1595 (1986).

[121] M. Ahart, M. Somayazulu, R. E. Cohen, P. Ganesh, P. Dera, H. Mao, R. J. Hemley, Y. Ren, P. Liermann, and Z. Wu, *Origin of Morphotropic Phase Boundaries in*

Ferroelectrics, Nature **451**, 545 (2008).

[122] A.-B. M. A. Ibrahim, R. Murgan, M. K. Abd Rahman, and J. Osm, *Morphotropic Phase Boundary in Ferroelectric Materials*, in *Ferroelectrics - Physical Effects* (InTech, 2011).

[123] Z. Kutnjak, J. Petzelt, and R. Blinc, *The Giant Electromechanical Response in Ferroelectric Relaxors as a Critical Phenomenon*, Nature **441**, 956 (2006).

[124] D. Damjanovic, *Ferroelectric, Dielectric and Piezoelectric Properties of Ferroelectric Thin Films and Ceramics*, Reports Prog. Phys. **61**, 1267 (1998).

[125] H. Fu and R. E. Cohen, *Polarization Rotation Mechanism for Ultrahigh Electromechanical Response in Single-Crystal Piezoelectrics*, Nature **403**, 281 (2000).

[126] J. Gough, *A Description of a Property of Caoutchouc, or Indian Rubber*, Memories Lit. Philos. Soc. Manchester **1**, 288 (1805).

[127] J. P. Joule, *On Some Thermo-Dynamic Properties of Solids*, Philos. Trans. R. Soc. London **149**, 91 (1859).

[128] W. Thomson, *On the Thermoelastic, Thermomagnetic, and Pyroelectric Properties of Matter*, London, Edinburgh, Dublin Philos. Mag. J. Sci. **5**, 4 (1878).

[129] X. Moya, E. Defay, V. Heine, and N. D. Mathur, *Too Cool to Work*, Nat. Phys. **11**, 202 (2015).

[130] S. G. Lu, B. Rožič, Q. M. Zhang, Z. Kutnjak, R. Pirc, M. Lin, X. Li, and L. Gorny, *Comparison of Directly and Indirectly Measured Electrocaloric Effect in Relaxor Ferroelectric Polymers*, Appl. Phys. Lett. **97**, 202901 (2010).

[131] S. G. Lu et al., *Organic and Inorganic Relaxor Ferroelectrics with Giant Electrocaloric Effect*, Appl. Phys. Lett. **97**, 162904 (2010).

[132] B. Rožič, B. Malič, H. Uršič, J. Holc, M. Kosec, B. Neese, Q. M. Zhang, and Z. Kutnjak, *Direct Measurements of the Giant Electrocaloric Effect in Soft and Solid Ferroelectric Materials*, Ferroelectrics **405**, 26 (2010).

[133] B. Rožič, Z. Kutnjak, B. Neese, S.-G. Lu, and Q. M. Zhang, *Electrocaloric Effect in the Relaxor Ferroelectric Polymer Composition P(VDF–TrFE–CFE) 0.90 – P(VDF–CTFE) 0.10*, Phase Transitions **83**, 819 (2010).

[134] S. G. Lu, B. Rožič, Q. M. Zhang, Z. Kutnjak, and B. Neese, *Enhanced Electrocaloric Effect in Ferroelectric Poly(Vinylidene-Fluoride/Trifluoroethylene) 55/45 Mol % Copolymer at Ferroelectric-Paraelectric Transition*, Appl. Phys. Lett. **98**, 122906 (2011).

[135] B. Rožič, B. Neese, S.-G. Lu, Q. M. Zhang, and Z. Kutnjak, *Direct Measurements of the Electrocaloric Effect in P(VDF-TrFE) (68/32) Copolymer Ferroelectric Films*, Ferroelectrics **416**, 139 (2011).

[136] B. Rožič, B. Malič, H. Uršič, J. Holc, M. Kosec, and Z. Kutnjak, *Direct Measurements of the Electrocaloric Effect in Bulk PbMg 1/3 Nb 2/3 O 3 (PMN) Ceramics*, Ferroelectrics **421**, 103 (2011).

[137] B. Rožič, S. G. Lu, Z. Kutnjak, B. Neese, and Q. M. Zhang, *Electrocaloric Effect in the Relaxor Ferroelectric Terpolymer P(VDF-TrFE-CFE)*, Ferroelectrics **422**, 81 (2011).

[138] B. Rožič, M. Kosec, H. Uršič, J. Holc, B. Malič, Q. M. Zhang, R. Blinc, R. Pirc, and

Z. Kutnjak, *Influence of the Critical Point on the Electrocaloric Response of Relaxor Ferroelectrics*, J. Appl. Phys. **110**, 064118 (2011).

[139] J. Küpfer and H. Finkelmann, *Nematic Liquid Single Crystal Elastomers*, Die Makromol. Chemie, Rapid Commun. **12**, 717 (1991).

[140] M. Lavrič et al., *Tunability of the Elastocaloric Response in Main-Chain Liquid Crystalline Elastomers*, Liq. Cryst. **48**, 405 (2021).

[141] L. B. Kong, H. Huang, and S. Li, *Fundamentals of Ferroelectric Materials*, in *Ferroelectric Materials for Energy Applications*, edited by H. Huang and J. F. Scott (Wiley-VCH Verlag GmbH & Co. KGaA, Weinheim, Germany, 2018), pp. 1–31.

[142] R. Blinc, *On the Isotopic Effects in the Ferroelectric Behaviour of Crystals with Short Hydrogen Bonds*, J. Phys. Chem. Solids **13**, 204 (1960).

[143] M. Ichikawa, K. Motida, and N. Yamada, *Negative Evidence for a Proton-Tunneling Mechanism in the Phase Transition of KH2PO4-Type Crystals*, Phys. Rev. B **36**, 874 (1987).

[144] R. J. Nelmes, *On the Structural Evidence for a Direct Proton Tunnelling Effect in the KH 2 PO 4 -Type Transition*, J. Phys. C Solid State Phys. **21**, L881 (1988).

[145] G. F. Reiter, J. Mayers, and P. Platzman, *Direct Observation of Tunneling in KDP Using Neutron Compton Scattering*, Phys. Rev. Lett. **89**, 135505 (2002).

[146] G. Shirane, J. D. Axe, J. Harada, and J. P. Remeika, *Soft Ferroelectric Modes in Lead Titanate*, Phys. Rev. B **2**, 155 (1970).

[147] G. Burns and B. A. Scott, *Raman Studies of Underdamped Soft Modes in PbTiO3*, Phys. Rev. Lett. **25**, 167 (1970).

[148] Y. Yamada, G. Shirane, and A. Linz, *Study of Critical Fluctuations in BaTiO3 by Neutron Scattering*, Phys. Rev. **177**, 848 (1969).

[149] A. F. Devonshire, *XCVI. Theory of Barium Titanate*, London, Edinburgh, Dublin Philos. Mag. J. Sci. **40**, 1040 (1949).

[150] A. F. Devonshire, *CIX. Theory of Barium Titanate— Part II*, London, Edinburgh, Dublin Philos. Mag. J. Sci. **42**, 1065 (1951).

[151] A. S. Mischenko, Q. Zhang, J. F. Scott, R. W. Whatmore, and N. D. Mathur, *Giant Electrocaloric Effect in Thin-Film PbZr0.95Ti0.05O3*, Science (80-.). **311**, 1270 (2006).

[152] X. Moya, E. Stern-Taulats, S. Crossley, D. González-Alonso, S. Kar-Narayan, A. Planes, L. Mañosa, and N. D. Mathur, *Giant Electrocaloric Strength in Single-Crystal BaTiO 3*, Adv. Mater. **25**, 1360 (2013).

[153] G. Dai, S. Wang, G. Huang, G. Chen, B. Lu, D. Li, T. Tao, Y. Yao, B. Liang, and S. Lu, *Direct and Indirect Measurement of Large Electrocaloric Effect in Barium Strontium Titanate Ceramics*, Int. J. Appl. Ceram. Technol. **17**, 1354 (2020).

[154] S. Qi, G. Zhang, L. Duan, T. Zeng, and J. Cao, *Electrocaloric Effect in Pb-Free Sr-Doped BaTi 0.9 Sn 0.1 O 3 Ceramics*, Mater. Res. Bull. **91**, 31 (2017).

[155] Z. Lv, J. Wei, T. Yang, Z. Sun, and Z. Xu, *Manipulation of Curie Temperature and Ferroelectric Polarization for Large Electrocaloric Strength in BaTiO3-Based Ceramics*, Ceram. Int. **46**, 14978 (2020).

[156] S. Patel, A. Chauhan, and R. Vaish, *Electrocaloric Behavior and Temperature-Dependent Scaling of Dynamic Hysteresis of Ba 0.85 Ca 0.15 Ti 0.9 Zr 0.1 O 3*

Ceramics, Int. J. Appl. Ceram. Technol. **12**, 899 (2015).

[157] B. Peng, H. Fan, and Q. Zhang, *A Giant Electrocaloric Effect in Nanoscale Antiferroelectric and Ferroelectric Phases Coexisting in a Relaxor Pb 0.8 Ba 0.2 ZrO 3 Thin Film at Room Temperature*, Adv. Funct. Mater. **23**, 2987 (2013).

[158] T. M. Correia, J. S. Young, R. W. Whatmore, J. F. Scott, N. D. Mathur, and Q. Zhang, *Investigation of the Electrocaloric Effect in a PbMg2/3Nb1/3O3-PbTiO3 Relaxor Thin Film*, Appl. Phys. Lett. **95**, 182904 (2009).

[159] D. Saranya, A. R. Chaudhuri, J. Parui, and S. B. Krupanidhi, *Electrocaloric Effect of PMN-PT Thin Films near Morphotropic Phase Boundary*, Bull. Mater. Sci. **32**, 259 (2009).

[160] K. S. Srikanth and R. Vaish, *Enhanced Electrocaloric, Pyroelectric and Energy Storage Performance of BaCe Ti1−O3 Ceramics*, J. Eur. Ceram. Soc. **37**, 3927 (2017).

[161] W. N. Lawless and A. J. Morrow, *Specific Heat and Electrocaloric Properties of a SrTiO3 Ceramic at Low Temperatures*, Ferroelectrics **15**, 159 (1977).

[162] M. E. Rogers, C. M. Fancher, and J. E. Blendell, *Domain Evolution in Lead-Free Thin Film Piezoelectric Ceramics*, J. Appl. Phys. **112**, 052014 (2012).

[163] S. Chihaoui, L. Seveyrat, V. Perrin, I. Kallel, L. Lebrun, and H. Khemakhem, *Structural Evolution and Electrical Characteristics of Sn-Doped Ba0.8Sr0.2TiO3 Ceramics*, Ceram. Int. **43**, 427 (2017).

[164] M. Chen, Z. Xu, R. Chu, Y. Liu, L. Shao, W. Li, S. Gong, and G. Li, *Polymorphic Phase Transition and Enhanced Piezoelectric Properties in (Ba0.9Ca0.1)(Ti1−xSnx)O3 Lead-Free Ceramics*, Mater. Lett. **97**, 86 (2013).

[165] Y. Yang, Y. Zhou, J. Ren, Q. Zheng, K. H. Lam, and D. Lin, *Coexistence of Three Ferroelectric Phases and Enhanced Piezoelectric Properties in BaTiO3–CaHfO3 Lead-Free Ceramics*, J. Eur. Ceram. Soc. **38**, 557 (2018).

[166] Z. Luo, D. Zhang, Y. Liu, D. Zhou, Y. Yao, C. Liu, B. Dkhil, X. Ren, and X. Lou, *Enhanced Electrocaloric Effect in Lead-Free BaTi 1−x Sn x O 3 Ceramics near Room Temperature*, Appl. Phys. Lett. **105**, 102904 (2014).

[167] X.-S. Qian, H.-J. Ye, Y.-T. Zhang, H. Gu, X. Li, C. A. Randall, and Q. M. Zhang, *Giant Electrocaloric Response Over A Broad Temperature Range in Modified BaTiO 3 Ceramics*, Adv. Funct. Mater. **24**, 1300 (2014).

[168] M. Sanlialp, Z. Luo, V. V. Shvartsman, X. Wei, Y. Liu, B. Dkhil, and D. C. Lupascu, *Direct Measurement of Electrocaloric Effect in Lead-Free Ba(Sn x Ti 1-x)O 3 Ceramics*, Appl. Phys. Lett. **111**, 173903 (2017).

[169] S.-G. Lu, X. Lin, J. Li, D. Li, Y. Yao, T. Tao, and B. Liang, *Enhanced Electrocaloric Strengths at Room Temperature in (SrxBa1−x)(Sn0.05Ti0.95)O3 Lead-Free Ceramics*, J. Alloys Compd. **871**, 159519 (2021).

[170] H. Zaitouni et al., *Structural, Dielectric, Ferroelectric and Tuning Properties of Pb-Free Ferroelectric Ba0.9Sr0.1Ti1-XSnxO3*, Ceram. Int. **46**, 27275 (2020).

[171] J. Liu, L. Liu, J. Zhang, L. Jin, D. Wang, J. Wei, Z. Ye, and C. Jia, *Charge Effects in Donor-doped Perovskite Ferroelectrics*, J. Am. Ceram. Soc. **103**, 5392 (2020).

[172] C. L. Freeman, J. A. Dawson, H.-R. Chen, L. Ben, J. H. Harding, F. D. Morrison, D. C. Sinclair, and A. R. West, *Energetics of Donor-Doping, Metal Vacancies, and*

Oxygen-Loss in A-Site Rare-Earth-Doped BaTiO 3, Adv. Funct. Mater. **23**, 3925 (2013).

[173] T. Sareein, P. Baipaywad, W. Chaiammad, A. Ngamjarurojana, S. Ananta, X. Tan, and R. Yimnirun, *Dielectric Aging Behavior in A-Site Hybrid-Doped BaTiO3 Ceramics*, Curr. Appl. Phys. **11**, S90 (2011).

[174] Y. Noguchi, H. Matsuo, Y. Kitanaka, and M. Miyayama, *Ferroelectrics with a Controlled Oxygen-Vacancy Distribution by Design*, Sci. Rep. **9**, 4225 (2019).

[175] W. Liu, W. Chen, L. Yang, L. Zhang, Y. Wang, C. Zhou, S. Li, and X. Ren, *Ferroelectric Aging Effect in Hybrid-Doped BaTiO3 Ceramics and the Associated Large Recoverable Electrostrain*, Appl. Phys. Lett. **89**, 172908 (2006).

[176] L. X. Zhang and X. Ren, *In Situ Observation of Reversible Domain Switching in Aged Mn-Doped BaTiO 3 Single Crystals*, Phys. Rev. B **71**, 174108 (2005).

[177] D.-Y. Lu, X.-Y. Sun, and M. Toda, *A Novel High-k 'Y5V' Barium Titanate Ceramics Co-Doped with Lanthanum and Cerium*, J. Phys. Chem. Solids **68**, 650 (2007).

[178] C. Fu, N. Chen, and G. Du, *Comparative Studies of Nickel Doping Effects at A and B Sites of BaTiO3 Ceramics on Their Crystal Structures and Dielectric and Ferroelectric Properties*, Ceram. Int. **43**, 15927 (2017).

[179] C. Li, X. Lu, W. Ding, L. Feng, Y. Gao, and Z. Guo, *Formability of ABX 3 (X = F, Cl, Br, I) Halide Perovskites*, Acta Crystallogr. Sect. B Struct. Sci. **64**, 702 (2008).

[180] M. I. Morozov and D. Damjanovic, *Charge Migration in Pb(Zr,Ti)O3 Ceramics and Its Relation to Ageing, Hardening, and Softening*, J. Appl. Phys. **107**, 034106 (2010).

[181] R. Gerson, *Variation in Ferroelectric Characteristics of Lead Zirconate Titanate Ceramics Due to Minor Chemical Modifications*, J. Appl. Phys. **31**, 188 (1960).

[182] L. Eyraud, B. Guiffard, L. Lebrun, and D. Guyomar, *Interpretation of the Softening Effect in PZT Ceramics Near the Morphotropic Phase Boundary*, Ferroelectrics **330**, 51 (2006).

[183] C. Ang, Z. Yu, Z. Jing, R. Guo, A. S. Bhalla, and L. E. Cross, *Piezoelectric and Electrostrictive Strain Behavior of Ce-Doped BaTiO3 Ceramics*, Appl. Phys. Lett. **80**, 3424 (2002).

[184] L. Zhang, E. Erdem, X. Ren, and R.-A. Eichel, *Reorientation of (MnTi″−VO••)× Defect Dipoles in Acceptor-Modified BaTiO3 Single Crystals: An Electron Paramagnetic Resonance Study*, Appl. Phys. Lett. **93**, 202901 (2008).

[185] K. Carl and K. H. Hardtl, *Electrical After-Effects in Pb(Ti, Zr)O3 Ceramics*, Ferroelectrics **17**, 473 (1977).

[186] G. Arlt and H. Neumann, *Internal Bias in Ferroelectric Ceramics: Origin and Time Dependence*, Ferroelectrics **87**, 109 (1988).

[187] X. Ren, *Large Electric-Field-Induced Strain in Ferroelectric Crystals by Point-Defect-Mediated Reversible Domain Switching*, Nat. Mater. **3**, 91 (2004).

[188] X. Ren and K. Otsuka, *Universal Symmetry Property of Point Defects in Crystals*, Phys. Rev. Lett. **85**, 1016 (2000).

[189] P. V. Lambeck and G. H. Jonker, *The Nature of Domain Stabilization in*

Ferroelectric Perovskites, J. Phys. Chem. Solids **47**, 453 (1986).

[190] R.-A. Eichel, *Defect Structure of Oxide Ferroelectrics—Valence State, Site of Incorporation, Mechanisms of Charge Compensation and Internal Bias Fields*, J. Electroceramics **19**, 11 (2007).

[191] Y. A. Genenko, J. Glaum, M. J. Hoffmann, and K. Albe, *Mechanisms of Aging and Fatigue in Ferroelectrics*, Mater. Sci. Eng. B **192**, 52 (2015).

[192] H. L. Stadler, *Etched Hillocks in BaTiO 3*, J. Appl. Phys. **34**, 570 (1963).

[193] L. Zhang and X. Ren, *Aging Behavior in Single-Domain Mn-Doped BaTiO3 Crystals: Implication for a Unified Microscopic Explanation of Ferroelectric Aging*, Phys. Rev. B **73**, 094121 (2006).

[194] Q. M. Zhang, H. Wang, N. Kim, and L. E. Cross, *Direct Evaluation of Domain-wall and Intrinsic Contributions to the Dielectric and Piezoelectric Response and Their Temperature Dependence on Lead Zirconate-titanate Ceramics*, J. Appl. Phys. **75**, 454 (1994).

[195] Z. Yao, H. Liu, Y. Liu, Z. Wu, Z. Shen, Y. Liu, and M. Cao, *Structure and Dielectric Behavior of Nd-Doped BaTiO3 Perovskites*, Mater. Chem. Phys. **109**, 475 (2008).

[196] A. R. West, T. B. Adams, F. D. Morrison, and D. C. Sinclair, *Novel High Capacitance Materials:- BaTiO3:La and CaCu3Ti4O12*, J. Eur. Ceram. Soc. **24**, 1439 (2004).

[197] V. Buscaglia, M. T. Buscaglia, and G. Canu, *BaTiO3-Based Ceramics: Fundamentals, Properties and Applications*, in *Encyclopedia of Materials: Technical Ceramics and Glasses* (Elsevier, 2021), pp. 311–344.

[198] J.-K. Lee, K.-S. Hong, and J.-W. Jang, *Roles of Ba/Ti Ratios in the Dielectric Properties of BaTiO3 Ceramics*, J. Am. Ceram. Soc. **84**, 2001 (2004).

[199] N. V. Dang, T. D. Thanh, L. V. Hong, V. D. Lam, and T.-L. Phan, *Structural, Optical and Magnetic Properties of Polycrystalline BaTi 1−x Fe x O 3 Ceramics*, J. Appl. Phys. **110**, 043914 (2011).

[200] T. Li, K. Yang, R. Xue, Y. Xue, and Z. Chen, *The Effect of CuO Doping on the Microstructures and Dielectric Properties of BaTiO3 Ceramics*, J. Mater. Sci. Mater. Electron. **22**, 838 (2011).

[201] H.-J. Hagemann, *Loss Mechanisms and Domain Stabilisation in Doped BaTiO 3*, J. Phys. C Solid State Phys. **11**, 3333 (1978).

[202] A. C. Caballero, J. F. Fernández, C. Moure, and P. Durán, *ZnO-Doped BaTiO3: Microstructure and Electrical Properties*, J. Eur. Ceram. Soc. **17**, 513 (1997).

[203] A. Salhi, S. Sayouri, A. Alimoussa, and L. Kadira, *Impedance Spectroscopy Analysis of Ca Doped BaTiO3 Ferroelectric Ceramic Manufactured with a New Synthesis Technique*, Mater. Today Proc. **13**, 1248 (2019).

[204] S. M. Said, M. F. M. Sabri, and F. Salleh, *Ferroelectrics and Their Applications*, in *Reference Module in Materials Science and Materials Engineering* (Elsevier, 2017).

[205] M. E. Lines and A. M. Glass, *Principles and Applications of Ferroelectrics and Related Materials* (Oxford University Press, 2001).

[206] J. N. Lin and T. B. Wu, *Effects of Isovalent Substitutions on Lattice Softening and Transition Character of BaTiO 3 Solid Solutions*, J. Appl. Phys. **68**, 985 (1990).

[207] S. Yasmm, S. Choudhury, M. A. Hakim, A. H. Bhuiyan, and M. J. Rahman, *Effect*

of Cerium Doping on Microstructure and Dielectric Properties of BaTiO3 Ceramics, J. Mater. Sci. Technol. **27**, 759 (2011).

[208] M. Ganguly, S. K. Rout, T. P. Sinha, S. K. Sharma, H. Y. Park, C. W. Ahn, and I. W. Kim, *Characterization and Rietveld Refinement of A-Site Deficient Lanthanum Doped Barium Titanate*, J. Alloys Compd. **579**, 473 (2013).

[209] K. Vani and V. Kumar, *Evolution of Dielectric and Ferroelectric Relaxor States in Al 3+ -Doped BaTiO 3*, AIP Adv. **5**, 027135 (2015).

[210] S. Merselmiz et al., *Enhanced Electrical Properties and Large Electrocaloric Effect in Lead-Free Ba0.8Ca0.2ZrxTi1−xO3 (x = 0 and 0.02) Ceramics*, J. Mater. Sci. Mater. Electron. **31**, 17018 (2020).

[211] H. Kaddoussi, A. Lahmar, Y. Gagou, B. Manoun, J. N. Chotard, J.-L. Dellis, Z. Kutnjak, H. Khemakhem, B. Elouadi, and M. El Marssi, *Sequence of Structural Transitions and Electrocaloric Properties in (Ba1-XCax)(Zr0.1Ti0.9)O3 Ceramics*, J. Alloys Compd. **713**, 164 (2017).

[212] Z. Hanani et al., *Enhanced Dielectric and Electrocaloric Properties in Lead-Free Rod-like BCZT Ceramics*, J. Adv. Ceram. **9**, 210 (2020).

[213] M. Sanlialp, V. V. Shvartsman, M. Acosta, and D. C. Lupascu, *Electrocaloric Effect in Ba(Zr,Ti)O 3 -(Ba,Ca)TiO 3 Ceramics Measured Directly*, J. Am. Ceram. Soc. **99**, 4022 (2016).

[214] H. Zaitouni et al., *Enhanced Electrocaloric and Energy-Storage Properties of Environment-Friendly Ferroelectric Ba0.9Sr0.1Ti1−xSnxO3 Ceramics*, Mater. Today Commun. **31**, 103351 (2022).

[215] A. Dixit, S. B. Majumder, R. S. Katiyar, and A. S. Bhalla, *Relaxor Behavior in Sol–Gel-Derived BaZr(0.40)Ti(0.60)O3 Thin Films*, Appl. Phys. Lett. **82**, 2679 (2003).

[216] C. Molin, T. Richter, and S. E. Gebhardt, *Tailoring Electrocaloric Properties of Ba1-XSrxSnyTi1-YO3 Ceramics by Compositional Modification*, J. Eur. Ceram. Soc. **42**, 140 (2022).

[217] T. Ikeda, J. Mamiya, and Y. Yu, *Photomechanics of Liquid-Crystalline Elastomers and Other Polymers*, Angew. Chemie Int. Ed. **46**, 506 (2007).

[218] Y. H. Na, Y. Aburaya, H. Orihara, K. Hiraoka, and Y. Han, *Electrically Induced Deformation in Chiral Smectic Elastomers with Different Domain Structures*, Phys. Rev. E **90**, 062507 (2014).

[219] A. Kaiser, M. Winkler, S. Krause, H. Finkelmann, and A. M. Schmidt, *Magnetoactive Liquid Crystal Elastomer Nanocomposites*, J. Mater. Chem. **19**, 538 (2009).

[220] H. Zeng, P. Wasylczyk, C. Parmeggiani, D. Martella, M. Burresi, and D. S. Wiersma, *Light-Fueled Microscopic Walkers*, Adv. Mater. **27**, 3883 (2015).

[221] S. Schuhladen, F. Preller, R. Rix, S. Petsch, R. Zentel, and H. Zappe, *Iris-Like Tunable Aperture Employing Liquid-Crystal Elastomers*, Adv. Mater. **26**, 7247 (2014).

[222] N. A. Platé and V. P. Shibaev, *Comb-Shaped Polymers and Liquid Crystals* (Springer US, Boston, MA, 1987).

[223] V. P. Shibaev and N. A. Platé, *Synthesis and Structure of Liquid-Crystalline Side-Chain Polymers*, Pure Appl. Chem. **57**, 1589 (1985).

[224] I. Kundler and H. Finkelmann, *Director Reorientation via Stripe-Domains in Nematic Elastomers: Influence of Cross-Link Density, Anisotropy of the Network and Smectic Clusters*, Macromol. Chem. Phys. **199**, 677 (1998).

[225] M. Brehmer, R. Zentel, G. Wagenblast, and K. Siemensmeyer, *Ferroelectric Liquid-Crystalline Elastomers*, Macromol. Chem. Phys. **195**, 1891 (1994).

[226] T. I. Yuranova, V. N. Vasilets, A. V. Kovalchuk, G. N. Savenkov, E. R. Zubarev, O. A. Otmakhova, and R. V. Talroze, *Regularities of γ-Ray Induced Polymerization for Two Mesogen-Containing Acrylic Monomers*, Macromol. Chem. Phys. **198**, 2121 (1997).

[227] A. Anwer and A. H. Windle, *Orientation Kinetics of Thermotropic Main-Chain Liquid-Crystalline Polymers in a Magnetic Field*, Polymer (Guildf). **32**, 103 (1991).

[228] N. R. Barnes, F. J. Davis, and G. R. Mitchell, *Molecular Switching in Liquid Crystal Elastomers*, Mol. Cryst. Liq. Cryst. Inc. Nonlinear Opt. **168**, 13 (1989).

[229] R. Zentel, *Shape Variation of Cross-Linked Liquid-Crystalline Polymers by Electric Fields*, Liq. Cryst. **1**, 589 (1986).

[230] E. M. Terentjev, M. Warner, and G. C. Verwey, *Non-Uniform Deformations in Liquid Crystalline Elastomers*, J. Phys. II **6**, 1049 (1996).

[231] J. V. Selinger, H. G. Jeon, and B. R. Ratna, *Isotropic-Nematic Transition in Liquid-Crystalline Elastomers*, Phys. Rev. Lett. **89**, 225701 (2002).

[232] W. Kaufhold, H. Finkelmann, and B. R. Helmut, *Nematic Elastomers, 1. Effect of the Spacer Length on the Mechanical Coupling between Network Anisotropy and Nematic Order*, Die Makromol. Chemie **192**, 2555 (1991).

[233] A. Lebar, Z. Kutnjak, S. Žumer, H. Finkelmann, A. Sánchez-Ferrer, and B. Zalar, *Evidence of Supercritical Behavior in Liquid Single Crystal Elastomers*, Phys. Rev. Lett. **94**, 197801 (2005).

[234] G. Cordoyiannis, A. Sánchez-Ferrer, H. Finkelmann, B. Rožič, S. Žumer, and Z. Kutnjak, *Thermal Study of the Isotropic to Smectic C Phase Transition in Main-Chain Liquid-Crystalline Elastomers*, Liq. Cryst. **37**, 349 (2010).

[235] B. Rožič, S. Krause, H. Finkelmann, G. Cordoyiannis, and Z. Kutnjak, *Controlling the Thermomechanical Response of Liquid-Crystalline Elastomers by Influencing Their Critical Behavior*, Appl. Phys. Lett. **96**, 111901 (2010).

[236] G. Cordoyiannis, A. Lebar, B. Zalar, S. Žumer, H. Finkelmann, and Z. Kutnjak, *Criticality Controlled by Cross-Linking Density in Liquid Single-Crystal Elastomers*, Phys. Rev. Lett. **99**, 197801 (2007).

[237] L. Petridis and E. M. Terentjev, *Nematic-Isotropic Transition with Quenched Disorder*, Phys. Rev. E **74**, 051707 (2006).

[238] H. Finkelmann, A. Greve, and M. Warner, *The Elastic Anisotropy of Nematic Elastomers*, Eur. Phys. J. E **5**, 281 (2001).

[239] S. M. Clarke, A. Hotta, A. R. Tajbakhsh, and E. M. Terentjev, *Effect of Crosslinker Geometry on Equilibrium Thermal and Mechanical Properties of Nematic Elastomers*, Phys. Rev. E **64**, 061702 (2001).

[240] D. Črešnar et al., *Elastocaloric Response in Liquid Crystalline Elastomers: Phenomenological Modelling and Experiments*, (n.d.).

[241] D. Črešnar et al., *Elastocaloric Effect in Liquid Crystalline Elastomers*, (n.d.).

[242] D. Črešnar et al., *Caloric Effects in Liquid Crystal-Based Soft Materials*, J. Phys. Energy **5**, 045004 (2023).

[243] G. Skačej, *Sample Preparation Affects the Nematic–Isotropic Transition in Liquid Crystal Elastomers: Insights from Molecular Simulation*, Soft Matter **14**, 1408 (2018).

[244] S. Krause, F. Zander, G. Bergmann, H. Brandt, H. Wertmer, and H. Finkelmann, *Nematic Main-Chain Elastomers: Coupling and Orientational Behavior*, Comptes Rendus Chim. **12**, 85 (2009).

[245] J. Schätzle, W. Kaufhold, and H. Finkelmann, *Nematic Elastomers: The Influence of External Mechanical Stress on the Liquid-Crystalline Phase Behavior*, Die Makromol. Chemie **190**, 3269 (1989).

Bibliography

Publications Related to the Thesis

Journal Articles

D. Črešnar, C. Kyrou, I. Lelidis, A. Drozd-Rzoska, S. Starzonek, S. Rzoska, Z. Kutnjak, and S. Kralj, *Impact of Weak Nanoparticle Induced Disorder on Nematic Ordering*, Crystals **9**, 171 (2019).

S. Merselmiz, Z. Hanani, S. B. Moumen, A. Matavž, D. Mezzane, N. Novak, Z. Abkhar, L. Hajji, M. Amjoud, Y. Gagou, K. Hoummada, D. Črešnar, Z. Kutnjak, and B. Rožič, *Enhanced Electrical Properties and Large Electrocaloric Effect in Lead-Free* $Ba_{0.8}Ca_{0.2}Zr_xTi_{1-x}O_3$ *(x = 0 and 0.02) Ceramics*, J. Mater. Sci. Mater. Electron. **31**, 17018 (2020).

M. Lavrič, N. Derets, D. Črešnar, V. Cresta, V. Domenici, A. Rešetič, G. Skačej, M. Sluban, P. Umek, B. Zalar, Z. Kutnjak, and B. Rožič, *Tunability of the Elastocaloric Response in Main-Chain Liquid Crystalline Elastomers*, Liq. Cryst. **48**, 405 (2021).

H. Zaitouni, L. Hajji, D. Mezzane, E. Choukri, A. G. Razumnaya, Y. Gagou, K. Hoummada, A. Alimoussa, B. Rožič, D. Črešnar, M. El Marssi, and Z. Kutnjak, *Enhanced Electrocaloric and Energy-Storage Properties of Environment-Friendly Ferroelectric* $Ba_{0.9}Sr_{0.1}Ti_{1-x}Sn_xO_3$ *Ceramics*, Mater. Today Commun. **31**, 103351 (2022).

Journal Articles in Preparation for Publication

D. Črešnar, N. Derets, M. Trček, G. Skačej, A. Rešetič, M. Lavrič, V. Domenici, B. Zalar, S. Kralj, Z. Kutnjak, and B. Rožič, *Elastocaloric effect in liquid crystalline elastomers, in preparation.*

D. Črešnar, N. Derets, M. Trček, G. Skačej, A. Rešetič, M. Lavrič, V. Domenici, B. Zalar, S. Kralj, Z. Kutnjak, and B. Rožič, *Elastocaloric response in liquid crystalline elastomers: phenomenological modelling and experiments, in preparation.*

Conference Abstracts

M. Lavrič, A. Rešetič, N. Derets, D. Črešnar, A. Sánchez-Ferrer, G. Skačej, B. Zalar, Z. Kutnjak, B. Rožič, *Elastocaloric effect in main-chain liquid crystal elastomers*, in *International Liquid Crystal Elastomer Conference, ILCEC 2019, 15-18 September 2019, Eindhoven, The Netherlands : program and abstracts*, Eindhoven, Netherlands (2019).

D. Črešnar, M. Lavrič, A. Rešetič, N. Derets, B. Zalar, Z. Kutnjak, and B. Rožič, *Large elastocaloric effect in liquid crystal elastomers*, in *International Symposium Nanomaterials, Microstructure and Properties, TRAMP19, 7-9 November, 2019, Marrakech, Morocco: abstracts book*, Marrakech, Morocco (2019).

D. Črešnar, M. Lavrič, A. Rešetič, N. Derets, B. Zalar, Z. Kutnjak, and B. Rožič, *Liquid crystal elastomers as soft elastocaloric materials*, in *Book of Abstracts / 12th Jožef Stefan International Postgraduate School Students' Conference and 14th Young Researchers' Day, 15th May, 2020*, Ljubljana, Slovenia (2020).

Other Publications

A. Fajmut, K. Pal, S. Harkai, D. Črešnar, Z. Kutnjak, and S. Kralj, *The core structure of a laboratory-made dust devil-like vortex and its condensed matter analogs*, J. Mol. Struct. **1237**, 130335 (2021).

N. Novak, D. Črešnar, G. Cordoyiannis, and R. Pirc, *Inverse Electrocaloric Effect in Ferroelectrics and Antiferroelectrics: A Phenomenological Approach*, Phys. B Condens. Matter **651**, 414598 (2023).

Biography

Dejvid Črešnar was born on 19 February 1990 in Maribor. He concluded his elementary school education in Osnovna šola Miklavž na Dravskem polju in 2005 and his high school education in Srednja gradbena šola in gimnazija Maribor in 2009. In 2013, he received his bachelor's degree in physics from the Faculty of Natural Sciences and Mathematics of the University of Maribor. The title of his dissertation was "The effect of nanoparticles on screw dislocations in smectic A phases" under the mentorship of Prof. Dr. Samo Kralj. In 2018, he received his master's degree in physics from the Faculty of Natural Sciences and Mathematics of the University of Maribor with the dissertation entitled "The impact of nanoparticles on the degree of the nematic ordering" under the mentorship of Prof. Dr. Samo Kralj and co-mentorship of Prof. Dr. Zdravko Kutnjak. For this work, he received an award for scientific research from the Faculty of Natural Sciences and Mathematics of the University of Maribor.